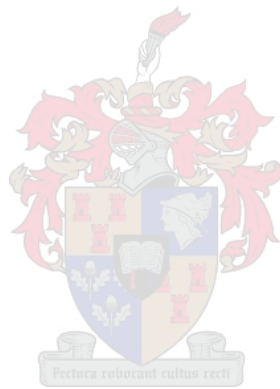


# Developing protocols for XCT scanning of dense mineral ore samples with applications to geology and minerals processing



LUNGA C. BAM

This is submitted in fulfilment of the requirements of a  
DOCTOR OF PHILOSOPHY IN THE FACULTY OF EARTH SCIENCES

**March 2020**

Department of Earth Science, Stellenbosch University

Supervisor: Prof Jodie Miller

Co-supervisor: Prof Megan Becker

#### Declaration

I hereby declare that the entirety of the work contained herein is my own, original work, that I am the authorship owner thereof (unless to the extent explicitly otherwise stated) and that I have not previously in its entirety or in part submitted it for obtaining any qualification. This thesis is submitted in fulfilment of a Doctor of philosophy in the department of Earth Science, Stellenbosch University.

Full name: Lunga C. Bam

March 2020

## Abstract

X-ray computed tomography (XCT) is a non-destructive technique capable of producing 3D mineralogical and textural information from drill cores. The discrimination between mineralogical information of the drill cores was optimised by using the developed linear attenuation coefficient data bank that can automatically provide linear attenuation coefficient information. The discrimination between the minerals was further optimised by using the determined optimal scanning parameters. XCT technique is most effective when scanning low density samples or minerals with low linear attenuation coefficients. However, when scanning high density samples, the technique suffers from the lack of X-ray penetration which results in beam hardening. Beam hardening affects the true representation of mineralogical and textural information and this leads to the misrepresentation of the mineralogical and textural information. Beam hardening is not easily quantifiable because its impact on the sample information is not uniform and can result in a loss of sample information. To address this, it was proposed to use an aluminium standard when scanning high density samples which acted as a standard in order to quantify the degree of beam hardening in each slice of the sample volume. The aluminium standard sample not only quantified the degree of beam hardening but also determined the optimal sample size for scanning where no sample information is lost. The optimal sample size for scanning was determined to be 4mm when scanning samples with  $SG > 3$ . Even though the impact of beam hardening was minimised when using the optimal sample size the degree of beam hardening still affected the discrimination between minerals. This led to the development of a simplified dual energy method in order to optimise the discrimination between minerals that are affected by beam hardening and result in high levels of noise within the images. The developed simplified dual energy method uses a combination of scanned volume data together with the simulated image. This combination has an advantage over the traditional dual energy method that uses two scanned volume data which is more time consuming. The simplified dual energy method effectively discriminated mineralogical information with no artefacts as compared to the traditional dual energy method which result in edge artefacts. The utilisation of the aluminium standard and the simplified dual energy method resulted in the reliable quantification of porosity information and 3D chalcopyrite grain size distribution (GSD). The quantified porosity information was largely in agreement with QEMSCAN results which show the importance of using the aluminium standard when scanning high density ore samples. The quantified 3D chalcopyrite GSD had a similar trend to the 2D QEMSCAN data but with coarser GSD as expected. This shows the effectiveness of the developed simplified dual energy method to optimise the discrimination of chalcopyrite in dense ore mineral samples. The reliable quantification of porosity and chalcopyrite information is important in minerals processing. Porosity is a component of texture and it is of relevance to physical processing where chalcopyrite is important in terms of inherent rock strength, its breakage, liberation properties and establishing geometallurgical units. The reliable quantification of the textural information using XCT shows that the technique can be adopted and adapted to any ore type with even more complex textures or mineralogies.



## List of Publications

### Peer Reviewed Journals:

- Bam, L.C.**, Miller, J.A., Becker, M., De Beer, F.C., Basson, I. 2016. X-ray Computed Tomography – Determination of Rapid Scanning Parameters for Geometallurgical Analysis of Iron Ore, in: Proceedings of the Third AusIMM International Geometallurgy Conference. Perth, pp. 209–219.
- Bam, L.C.**, Miller, J.A., Becker, M., Basson, I.J., 2019. X-ray Computed Tomography: Practical Evaluation of Beam Hardening in Iron Ore Samples. Miner. Eng. 131, 206–215. <https://doi.org/10.1016/j.mineng.2018.11.010>

### Papers in Preparation:

- Bam, L.C.**, Miller, J.A., Becker, M., In Prep a 2018. Application of a Simplified Dual Energy X-Ray Computed Tomography Method for Analysis of High Density Ore Samples.
- Bam, L.C.**, Miller, J.A., Becker, M., In Prep b 2018. A simple Tool to Calculate X-ray Linear Attenuation Coefficients to Assess Mineralogical Differentiation for X-ray Computed Tomography Scanning.
- Bam, L.C.**, Becker, M., Miller, J.A., In Prep c 2018. Customisation of XCT scanning protocols for the quantification of textural attributes in high density ores

### Conference proceedings:

- Bam, L.C.**, Miller, J.A., Becker, M., De Beer, F.C., Basson, I. 2015. Optimisation of  $\mu$ XCT Measurement Parameters for 3D Mineralogical and Textural Imaging of Iron Ores in Real Time, MinProc, August
- Bam, L.C.**, Miller, J.A., Becker, M., De Beer, F.C., Basson, I. 2015. Optimisation of  $\mu$ XCT Measurement Parameters for 3D Mineralogical and Textural Imaging of Iron Ores in Real Time, SAMMRI workshop, November
- Bam, L.C.**, Miller, J.A., Becker, M., de Beer, F., and Basson, I.J., 2016. X-ray computed tomography – Determination of rapid scanning parameters for geometallurgical analysis of iron ores. The third international AUSIMM Geometallurgy Conference, Perth, 15-16th June, pp. 209-219.
- Bam\*, L.C.**, Miller, J.A., Becker, M., Basson, I.J., de Beer, F., 2016. Determination of Hematite and Magnetite Attenuation Coefficients for the Optimisation of X-ray Computed Tomography Scanning Resolution. 35th International Geological Congress, Cape Town, August.
- Bam, L.C.**, Miller, J.A., Becker, M. 2016. Application of X-Ray Dual Energy Tomography to Iron Ore, SAMMRI workshop, November.
- Bam\*, L.C.**, Miller, J., Basson, I.J., Becker, M., 2017. X-ray computed tomography: Challenges in iron ore analysis for process mineralogy. MEI Process Mineralogy 17, Cape Town, March.
- Bam, L.C.**, Becker, M., Miller, J.A., 2018. Application of refined protocols for XCT scanning of high-density ore samples, Process Mineralogy '18, November

# Table of Contents

<b>Abbreviations</b>	<b>xii</b>
<b>Glossary</b>	<b>xiii</b>
<b>Acknowledgements</b>	<b>xiv</b>
<b>Chapter 1: Introduction</b>	<b>1</b>
1.1. Problem Statement	4
1.2. Aims of the Study	4
1.3. Project Scope	5
1.4. Thesis Outline	6
1.5. Statement of Novelty	7
1.6. Fundamentals of X-ray Computed Tomography	7
1.6.1. Overview	7
1.6.2. Different XCT Systems	8
1.6.3. XCT Configuration	9
1.6.3.1. X ray Source	10
1.6.3.2. Detectors	11
1.7. Minerals Processing	12
1.8. References	13
<b>Chapter 2: A simple Tool to Calculate X-ray Linear Attenuation Coefficients to Assess Mineralogical Differentiation for X-ray Computed Tomography Scanning</b>	<b>16</b>
1. Introduction	17
2. Methodology	18
2.1. Tungsten Energy Spectrum	18
2.2. Development of the Attenuation Coefficient Databank	20
2.3. Development of User Spreadsheet	20
2.4. Validation of Linear Attenuation Coefficients	20
3. Results	22
3.1. Calculated Linear Attenuation Coefficients	24
3.2. Minimum Attenuation Coefficient Difference to Determine Discrimination	24
4. Discussion	26
4.1. Mineral Composition and Linear Attenuation Coefficient	26
4.2. Mineral Density and Attenuation	28
4.3. Influence of mineral composition vs density on attenuation coefficient	28
5. Conclusions	28
6. Acknowledgements	29
7. References	29
<b>Chapter 3: X-Ray Computed Tomography – Determination of Rapid Scanning</b>	<b>31</b>

<b>Parameters for Geometallurgical Analysis of Iron Ore</b>	
1. Introduction	32
2. Micro-focus X-Ray Computed Tomography	33
2.1. Scanning Parameters	33
2.1.1. X-ray Source and Energy	34
2.1.2. Reconstruction	34
2.1.3. Signal to noise ratio	35
3. Materials and Methods	36
3.1. Sample Selection and Characterization	36
3.2. Experimental Approach	36
3.2.1. Phase One	36
3.2.2. Phase Two	36
3.3. Image Reconstruction	37
3.4. Volume Analysis	37
4. Results	37
4.1. X-ray Attenuation	37
4.2. X-ray Penetration and Contrast	38
4.3. Beam Hardening Correction	39
4.4. Signal to Noise Ratio	39
5. Discussion	39
6. Conclusion	42
7. Acknowledgements	42
8. References	42
9. Supplementary Notes on Scanning Parameters	44
9.1. Focal Spot Size	44
9.2. X-Ray Energy	44
9.3. Number of Projections	44
9.4 Filter Materials	45
9.5 Beam Hardening and Exposure Time Evaluation	45
 <b>Chapter 4: X-ray Computed Tomography: Practical Evaluation of Beam Hardening in iron ore samples</b>	 <b>46</b>
1. Introduction	47
2. Artefacts in X-ray tomography	48
2.1. Common Artefacts	48
2.2. Beam Hardening	49
2.3. Noise	49
3. Methodology	49
3.1. Sample Preparation	49
3.1.1. Hematite Stepped-wedge	50
3.1.2. Core Samples	50
3.1.3. Aluminium Standard Sample	51
3.2. Scanning Protocol	51
3.3. Scan Quality	51
3.4. Line Profiles	52
4. Results and discussion	52
4.1. Loss of Information Due to Beam Hardening	52
4.2. Porosity Information	52
4.3. Beam Hardening Evaluation Method	53
4.4. The Application of the Aluminium Standard Sample to Different Sample Geometries	55
5. Conclusions	56
6. Acknowledgements	57
7. References	57

8. Supplementary Notes on Beam Hardening	59
8.1 Application of Filter Materials	59
8.2 Signal-To-Noise Ratio	59
8.3 Line Profile	59
8.4 Specularite Vein	59
8.5 Quantification of Pore Volume and %Porosity Information	60
8.6 Utilisation of Aluminium Standard Sample	60
8.7 Quantification of the %Error	60
<b>Chapter 5: Application of a Simplified Dual Energy X-Ray Computed Tomography Method for Analysis of High Density Ore Samples</b>	<b>62</b>
1. Introduction	63
2. Methodology	64
2.1. Simplified Dual Energy Method	6
2.1.1 Linear Attenuation Coefficient of Minerals	5
2.1.2. The Generation of the Simulated Image	5
2.2. Samples	6
2.3. X-Ray Source Calibration	6
2.4. Scanning Conditions	7
3. Results	67
3.1. Dual Energy	7
3.1.1 Beam Alignment	7
3.1.2. Unsharpness	9
3.1.3. Beam Hardening Artefacts	9
3.2. Application of Dual Energy to Different Samples	0
4. Discussion	71
4.1. Impact of X-Ray Source	71
4.2. Impact of Beam Hardening	73
4.3. Application of Dual Energy	73
5. Conclusion	73
6. Acknowledgements	74
7. References	74
<b>Chapter 6: Customisation of XCT scanning protocols for the quantification of textural attributes in high density ores</b>	<b>75</b>
1. Introduction	76
2. Materials and Methods	78
2.1. Samples	78



2.2. QEMSCAN	78
2.3. X-Ray Computed Tomography	78
2.3.1. Iron Ore Case Study	79
2.3.2. Polymetallic Sulphide Ore Case Study	79
3. Iron Ore Case Study	79
3.1. Results	79
3.2. Discussion	82
4. Polymetallic Sulphide ore Case study	82
4.1. Results	82
4.2. Discussion	84
5. Conclusions	85
6. Acknowledgements	85
7. References	85
 <b>Chapter 7: Conclusion and Recommendation</b>	 <b>87</b>

# Figures

## Chapter 1: Introduction

<b>Fig 1.1.</b>	Declining ore grades for a variety of base and precious metals in Australia (Prior et al., 2012).	2
<b>Fig 1.2.</b>	Different generations of X-ray computed tomography medical scanners with different designs.	8
<b>Fig 1.3.</b>	A schematic diagram of a common lab-based $\mu$ XCT setup with a conical X-ray beam which allows a geometrical magnification.	9
<b>Fig 1.4.</b>	Different analytical techniques to quantify mineralogical and textural information (Becker et al., 2016)	12

## Chapter 2: A simple Tool to Calculate X-ray Linear Attenuation Coefficients to Assess Mineralogical Differentiation for X-ray Computed Tomography Scanning

<b>Fig 2.1.</b>	Different tungsten energy spectrums collected at different energies.	18
<b>Fig 2.2.</b>	Correlation between the effective X-ray energy and the X-ray energy spectrum of the tungsten target.	19
<b>Fig 2.3.</b>	The representation of iron mass attenuation coefficient by different equations (linear, second and fifth order polynomial). The black lines represent linear equations (equation 1) and the red and green curves represent the second and fifth order polynomial equations (equation 2 and 3).	22
<b>Fig 2.4.</b>	Variation of linear attenuation coefficients for different mineral densities calculated with the developed spreadsheet and NIST at: A) 44.79keV and B) 62.53keV X-ray energy	24
<b>Fig 2.5.</b>	Grey value variation of different minerals with their corresponding false color to illustrate discrimination between minerals at 45.5keV effective energy: A) almandine, B) andradite, C) grossular, D) quartz, E) kaolinite, F) dolomite, G) calcite, H) apatite, I) fluorite, J) goethite, K) chromite, L) magnetite and M) hematite.	25
<b>Fig 2.6.</b>	Mineral classification using QEMSCAN in order to understand the discrimination between the minerals: A) almandine, B) andradite, C) grossular, D) quartz, E) Kaolinite, F) dolomite, G) calcite, H) apatite, I) fluorite, J) goethite, K) chromite, L) magnetite and M) hematite.	27

## Chapter 3: X-Ray Computed Tomography – Determination of Rapid Scanning Parameters for Geometallurgical Analysis of Iron Ore

<b>Fig 3.1.</b>	Components and the principle of X-ray computed tomography.	33
<b>Fig 3.2.</b>	Tungsten X-ray energy beam spectrums measured at different energies of 60, 80, 100, 120, 140, 160 and 180keV.	34
<b>Fig 3.3.</b>	Correlation between X-ray energy spectrums to their effective X-ray energy.	35

<b>Fig 3.4.</b>	Ring and beam hardening artefacts on an XCT image slice.	35
<b>Fig 3.5.</b>	(a) QEMSCAN false colour image and (b) backscattered electron (BSE) image illustrating the heterogenous iron ore texture. The darker and lighter grey values on the BSE image represent quartz and hematite respectively.	36
<b>Fig 3.6.</b>	Attenuation coefficient for hematite and quartz as a function of effective energy.	37
<b>Fig 3.7.</b>	Shows the effect on increasing X-ray energy to image contrast at (a) 60keV, (b) 80keV, (c) 100keV, (d) 120keV, (e) 140keV, (f) 160keV and (g) 180keV. Detectable contrast difference is only visual between 60 and 80keV, beyond 100keV it is rather difficult to differentiate contrast between the image slices.	38
<b>Fig 3.8.</b>	Contrast distribution as a function of energy for hematite and quartz.	39
<b>Fig 3.9.</b>	(a) Image slice with no beam hardening correction applied, (b) and (c) line and histogram profile distribution for grey values for both hematite and quartz before beam hardening correction, (d) image slice with beam hardening correction applied, (e) and (f) line and histogram profile distribution of hematite and quartz grey values after beam hardening correction.	40
<b>Fig 3.10.</b>	(a) Image slice before beam hardening correction; (b, c and d) hematite signal to noise ratio (SNR), quartz SNR, and sample contrast (hematite and quartz contrast) before beam hardening correction; (e) image slice after beam hardening; (f, g and h) hematite SNR, quartz SNR and sample contrast after beam hardening corrections has been applied.	41

#### **Chapter 4: X-ray Computed Tomography: Practical Evaluation of Beam Hardening in iron ore samples**

<b>Fig 4.1.</b>	Hematite stepped-wedge sample with different thickness	50
<b>Fig 4.2.</b>	Different sample geometries of apatite-magnetite cores to evaluate beam hardening effect due to different geometries: cylindrical (38 x 34mm), half cylinder (19 x 34mm) and quarter cylinder (17 x 20mm).	50
<b>Fig 4.3.</b>	Aluminium standard sample with a 2mm pore diameter utilised to indirectly assess the impact of beam hardening artefacts for hematite and core samples.	51
<b>Fig 4.4.</b>	(a) Hematite stepped-wedge longitudinal image showing different thickness regions, (b) SNR of different thicknesses of the hematite stepped-wedge before and (c) after beam hardening correction was applied.	52
<b>Fig 4.5.</b>	(a) to (e) show line profiles for different thickness increments of the hematite stepped-wedge before the beam hardening correction was applied, and (f) to (j) shows line profiles after beam hardening correction was applied.	53
<b>Fig 4.6.</b>	(a) Longitudinal image slice of the stepped-wedge showing the loss of information with increasing sample thickness, (b) The variation of quantified maximum pore volume of 4, 14 and 24mm thickness at different X-ray energies before beam hardening correction was applied, and (c) Quantified maximum pore volume after beam hardening correction was applied.	54
<b>Fig 4.7.</b>	(a) Porosity information of different stepped-wedge thicknesses and different X-ray energies before the beam hardening correction was applied, and (b) Porosity information after the beam hardening correction was applied.	54
<b>Fig 4.8.</b>	Shows the positioning of the aluminium standard samples in order to indirectly evaluate the impact of beam hardening for each thickness	54

<b>Fig 4.9.</b>	(a) and (b) Shows the calculated pore surface area of the aluminium standard sample before and after the beam hardening correction was applied, and (c) and (d) show the variation of the scan quality due to increasing sample thickness.	55
<b>Fig 4.10.</b>	(a) to (f) Shows the scan qualities of full, half and quarter cylinder of the apatite-magnetite sample before and after beam hardening correction was applied.	56
<b>Fig 4.A.</b>	Stepped-wedge sample cut from a natural piece of hematite ore with a specularite vein bisecting the entire sample	60

## **Chapter 5: Application of a Simplified Dual Energy X-Ray Computed Tomography Method for Analysis of High-Density Ore Samples**

<b>Fig 5.1.</b>	The linear attenuation coefficient distribution with increasing X-ray energy of chalcopyrite, pyrite and magnetite.	64
<b>Fig 5.2.</b>	(a) Simulated images representing pyrite and chalcopyrite grey values at 130kV and (b) Pyrite and chalcopyrite grey value distribution assuming a monochromatic X-ray beam.	65
<b>Fig 5.3.</b>	Tungsten cross used for X-ray beam alignment at (a) 70kV, (b) 130kV and (c) the resulting image to evaluate the X-ray beam position at both energies	66
<b>Fig 5.4.</b>	Witwatersrand basin quartz conglomerate sample scanned at (A) 70kV, (B) 130kV and (C) the discrimination of chalcopyrite from pyrite grains through dual energy subtraction method.	68
<b>Fig 5.5.</b>	Distribution of peak positions for quartz, pyrite and chalcopyrite at 45.5keV and 61.3keV with optimized X-ray beam alignment.	68
<b>Fig 5.6.</b>	(a) Witwatersrand basin quartz conglomerate scanned at 45.5keV, (b) Simulated grey values of pyrite and chalcopyrite at 61.3keV and (c) Dual energy subtraction result.	68
<b>Fig 5.7.</b>	Witwatersrand basin quartz conglomerate scanned at (a) 70kV, (b) 130kV, (c) dual energy subtraction between 70kV and 130kV and (d) dual energy subtraction between 70kV and 130kV simulated image.	69
<b>Fig 5.8.</b>	Distribution of peak positions for quartz, pyrite and chalcopyrite at 70kV and 130kV influenced by misaligned X-ray beam..	70
<b>Fig 5.9.</b>	Witwatersrand basin quartz conglomerate scanned at (A) 70kV, (B) 130kV before induced beam hardening artefact and (C) 70kV and (D) 130kV after beam hardening has been induced experimentally.	70
<b>Fig 5.10.</b>	Distribution of peak positions for quartz, pyrite and chalcopyrite at 70kV and 130kV influenced by beam hardening artefact.	71
<b>Fig 5.11.</b>	(a) Dual energy subtraction of 70kV and 130kV scans and (b) dual energy subtraction of 70kV scan and 130kV simulated image.	71
<b>Fig 5.12.</b>	The Discrete pyrite and chalcopyrite mineral separates scanned at 70kV (a) and (d), processed with dual energy subtraction using 70kV and 130kV scans (b) and (e), and also processed with dual energy subtraction using a 70kV scan and 130kV simulated image (c) and (f).	72
<b>Fig 5.13.</b>	Two different slice positions of the apatite magnetite iron ore scanned at (A) and (D) 70kV, (B) and (E) dual energy subtraction result using 70kV and 130kV scans and, (C) and (F) dual energy subtraction method using the 70kV and 130kV simulated image.	72

## Chapter 6: Customisation of XCT scanning protocols for the quantification of textural attributes in high density ores

<b>Fig 6.1.</b>	(a) The distribution of the quantified %Error in each slice of the massive hematite ore sample and (b) Iron formation showing the presence of quartz and pores in the interstitial spaces of massive hematite ore (slice number 157)	80
<b>Fig 6.2.</b>	Histogram of frequency of 3D pore diameter distribution within the interstitial spaces of the massive hematite ore sample..	80
<b>Fig 6.3.</b>	(a) The distribution of %Error for compact hematite and (b) 2D image slice of compact hematite (slice number 212)	80
<b>Fig 6.4.</b>	(a) The distribution of %Error for compact itabirite, (B) 2D image slice (slice number 311) and (C) 2D image slice (slice number 433) of compact itabirite.	81
<b>Fig 6.5.</b>	Histogram of frequency of 3D pore diameter distribution of compact itabirite and hematite with minimum pore size of 15 $\mu\text{m}$ .	81
<b>Fig 6.6.</b>	(a) The distribution of %Error for goethite and (b) 2D image slice of goethite.	83
<b>Fig 6.7.</b>	%Error for each image slice of the polymetallic sulphide ore sample (UOB) at 70kV X-ray energy.	83
<b>Fig 6.8.</b>	Shows different image slices of the polymetallic sulphide ore sample with magnetite dominated before and after dual energy subtraction (a) and (c), and (b) and (d). The discriminated chalcopyrite grains grey values were compared to the chalcopyrite standard sample..	83
<b>Fig 6.9.</b>	The comparison of 3D XCT (UOB) and QEMSCAN (UOB) grain size distribution of the polymetallic sulfide ore sample.	84
<b>Fig. 6.10</b>	QEMSCAN images showing different distributions of the chalcopyrite grains in different sections of the same polymetallic sulphide ore sample	84

## Tables

### **Chapter 2: A simple Tool to Calculate X-ray Linear Attenuation Coefficients to Assess Mineralogical Differentiation for X-ray Computed Tomography Scanning**

<b>Table 2.1.</b>	Excel spreadsheet template with inputs under number of atoms in the compound, density and voltage for each mineral. The calculated output is under X-ray attenuation coefficient.	21
<b>Table 2.2.</b>	Scanning parameters to optimize discrimination between minerals.	22
<b>Table 2.3.</b>	Comparison of the NIST and spreadsheet attenuation coefficient for different types of minerals.	23
<b>Table 2.4.</b>	Grey value variation of different minerals with their corresponding density [ <a href="https://www.mindat.org/">https://www.mindat.org/</a> ] and linear attenuation coefficients.	25
<b>Table 2.5.</b>	Mineral discrimination using linear attenuation coefficient difference in conjunction with grey value and density difference.	26
<b>Table 2.6.</b>	Summary of common minerals in iron ores, alongside their formulae and density <a href="https://www.mindat.org/">https://www.mindat.org/</a> .	27

### **Chapter 5: Application of a Simplified Dual Energy X-Ray Computed Tomography Method for Analysis of High Density Ore Samples**

<b>Table 5.1.</b>	Scanning conditions for all the sample	67
<b>Table 5.2.</b>	Comparison between the experimental and experimental + simulated image result of the dual energy method	73

### **Chapter 6: Customisation of XCT scanning protocols for the quantification of textural attributes in high density ores**

<b>Table 6.1.</b>	Summary of the drill core samples analysed in Case studies 1 and 2.	78
<b>Table 6.2.</b>	Scanning parameters for porosity quantification, optimization parameters and chalcopyrite discrimination.	79
<b>Table 6.3.</b>	Comparison of 2D and 3D porosity information of different iron ore samples.	81

## Abbreviations

µm:	micrometre
mm:	millimetre
3D:	three-dimensional
2D:	two-dimensional
g/cm <sup>3</sup> :	density
x, y, z axis:	Cartesian coordinate system
kV:	kilovolt - a unit of electric potential equal to 1000 volts
µA:	current - a unit of electric current equal to one millionth of an ampere
W:	is the unit of power referred to as “watt”
ROI:	region of interest
FOV:	field of view
GSD:	grain size distribution
XCT:	X-ray computed tomography
CBCT:	cone beam computed tomography
µXCT:	micro-focus X-ray computed tomography
MLA:	Mineral Liberation Analyser
TIMA-X:	Tescan Integrated Mineral Analyser
SEM-EDS:	scanning electron microscopes with energy dispersive X-Ray spectrometry
QEMSCAN:	Quantitative Evaluation of Minerals by Scanning Electron Microscopy
EMPA:	Electron microprobe analysis

# Glossary

Linear attenuation coefficient	is a constant that describes the fraction of the attenuated incident photons in a monochromatic beam per unit thickness of a material. It is numerically expressed in units of $\text{cm}^{-1}$
Grey value:	it is a unit that indicates the brightness of a pixel
Effective energy:	X-ray energy calculated by combining all the X-ray or photon energies of the spectrum relative to the count ratio for each photon energy of the spectrum
Dual energy:	X-ray computed tomography technique that uses two separate energy spectrums to improve contrast between different phases or reveal hidden information
X-ray focal spot size:	a region on a target (tungsten, silver, etc) where X-rays are produced through an interaction of electrons with a target
Beam hardening:	a process that occurs when a polychromatic X-ray beam passes through the sample resulting in selective attenuation of lower X-ray photons. It causes the edges of the sample to appear brighter than the centre even though the sample is the same throughout.
Signal-to-noise ratio (SNR):	it is a measure of detectability of an object within an image that describes the ratio between the signal and noise within the region of interest
Maximum pore volume:	quantified maximum pore volume at different scanning parameters to determine data reliability and the impact of beam hardening
Particles or grains:	refers to individual mineral volumes within a sample.
Pore surface area:	is a cross-sectional area or pore area of the aluminium cylindrical pore sample
%Error:	it is a comparison between the quantified pore areas of aluminium cylindrical sample within the images with the expected or known pore surface area given as $\%Error = 100 - [ (Pore\ Area)_{quantified} / (Pore\ Area)_{known} ] * 100$



## Acknowledgements

First of all I would like to thank my supervisors for their continuous support and guidance during this project. Dr Jodie Miller, your knowledge, critical reviews and questions sparked an interest in me and provided a direction during this project. Dr Megan Becker, your interest in the project, our continuous discussions and your deep knowledge provided a direction for this project. I would also like to thank both my supervisors for allowing me the freedom to pursue my own interest as well.

To my wife, best friend Norah Nomfanelo Bam and son Amkhuselel Bam, thank you for your love, support, encouragement, and for being my source of strength during my darkest hours.

I would also like to thank my colleagues at Necsa Dr Frikkie de Beer, Mr Robert Nshimirimiana and Mr Jakobus Hoffman, for their continuous support and guidance during this time. To my immediate supervisor at work Dr Frikkie de Beer and Necsa management team, thank you for allowing me the time to do this project.

To Mr Mabuti Radebe, thank you for listening to all my crazy ideas, your continuous support and scientific guidance is appreciated as well.

To Mihloti Baloyi and Lebo Mokwena thank you for your support during this time.

This project is supported by South African Minerals to Metals Research Initiative (SAMMRI) and Necsa which I'm truly grateful for.

I would like to thank all my friends for their continuous support during this time, I am truly grateful.

To all my friends in the PhD lab at the department of Earth Science, your support is highly appreciated.

To Jani van Gend-Muller, thank you for all you have done and your extended efforts are really appreciated.

Finally, my dearest family. My mother Fikile Beslina Bam, thank you for your love, guidance, patience and, for being my best friend and comedian that shared jokes when I was down. My late father Zandisile Edward Bam, thank you for your support in everything I wanted to do and for being my number one fan. My sister Nozuko Bam, thank you for your love, patience, your continuous support from my undergraduate studies until now and for believing in your younger brother. To my brother Bongane Shabalala, thank you for your support and believing in me. My grandmother, aunts and all my cousins, thank you for your love and support during this time. To my uncle Visimuza Shabalala, thank you for all your support and taking care of my family during the time of need. To my in-laws, Mr Maduse, Mrs Maduse, Kutlwano Maduse, Katlego Maduse and Ofense Maduse thank you for your love, support and for looking after my wife and son during this time.

## Introduction

In the last few decades, mining companies have shifted to mining and processing of lower grade, less accessible, more heterogeneous and complex ores in response to the general decline in ore grades over the last century as the high grade, accessible and easy to process ores have been mined out (Fig. 1; Prior et al., 2012). All ores generally require some form of processing to concentrate the valuable minerals to produce a saleable product, and particularly so for the lower grade, complex and heterogeneous ores (Wills and Napier-Munn, 2005). For these and other reasons, mines are now looking for a far more detailed understanding of the variation in ore mineralogy, valuable metal deportment and mineral grades as well as how these minerals are spatially distributed in the host ores. The best way to do this is by utilising analytical techniques that can statistically quantify these attributes for each defined ore type in order to provide a full mineralogical and textural characterisation of them (Johnson et al., 2007; Becker et al., 2016).

For many years, mineralogical information was obtained through chemical assays which were used to calculate or infer a modal mineralogy for a bulk sample or through quantitative X-Ray diffraction analysis when quantitative modal mineralogy was required (Becker et al., 2016). These methods though were limited in their ability to provide statistically meaningful datasets of upfront ore mineralogy and particle and grain size characteristics of processing streams. Quantitative mineralogical information proved to be extremely useful and this prompted further developments to produce information through automated measurements. Over time, the optical systems were replaced by scanning electron microscopes with energy dispersive X-Ray spectrometry (SEM-EDS) based systems – for example QEMSCAN (Quantitative Evaluation of Minerals by Scanning Electron Microscopy), MLA (Mineral Liberation Analyser) and TIMA-X (Tescan Integrated Mineral Analyser) and Mineralogic (Fandrich et al., 2007; Zhou and Gu, 2016; Wightman et al., 2016). These modern SEM based systems are able to provide detailed and quantitative information on the bulk mineralogy, grain size and shape distribution, liberation and association and provide statistically representative datasets on these parameters. However, the above techniques are limited to 2D information and require extensive sample preparation and also suffer from stereological error (Evans et al., 2015; Spencer and Sutherland, 2000). More recently, the focus has turned to characterizing mineralogical and textural information in 3D using X-ray computed tomography (XCT) because it does not suffer from stereological error and captures the full mineralogical and textural variability of the ore, while requiring very little in the way of sample preparation. It is also ideally suited to the analysis of drill cores which are generated months prior to the processing and mining of any particular area of a mineral deposit (Becker et al., 2016).

The successful application of XCT in the geosciences has attracted a lot of attention due to its ability to characterize minerals in-situ within the rock matrices and because it is non-destructive. The technique

## CHAPTER 1: Introduction

generates a volume of the ore sample that allows visualisation of the mineralogical information in 3D to quantify the real distribution of grains or

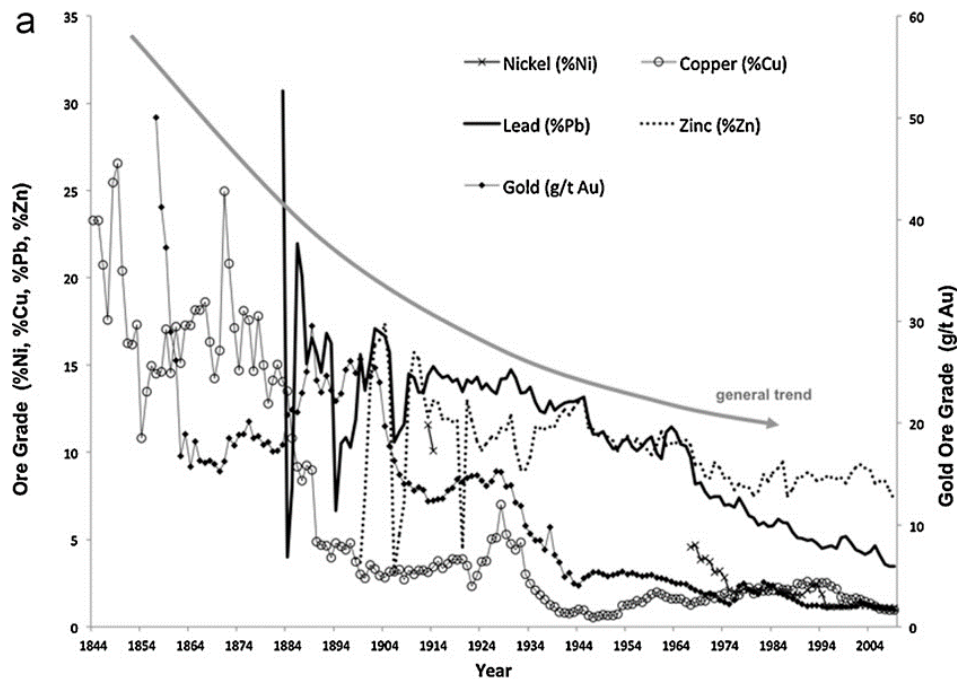


**Fig 1.1.** Declining ore grades for a variety of base and precious metals in Australia (Prior et al., 2012).

particles including their size, shape and orientation. The technique identifies minerals based on the attenuation coefficient because each mineral has a unique attenuation coefficient that depends on their mineralogical composition, density and X-ray energy (Wang et al., 2011). This advantage allows a variety of mineralogical information to be quantified for different ore types based on attenuation coefficients. Through this, the technique has the potential to provide parameters relevant to process mineralogy (grain size distribution, spatial location, liberation and association, porosity etc). There are a number of examples where XCT has been used successfully including the quantification and characterisation of porosity in reservoir rocks (Van Geet et al., 2000), quantification of porosity and permeability in porous rocks in petroleum engineering (Akin and Kovscek, 2003), determination of the liberation efficiency of copper through heap leaching (Miller et al., 2003) and characterisation of iron ore pellets by quantifying porosity as part of downstream processing (Forsberg and Hjortsberg, 2012). However, while XCT has been used to study different ore samples to better understand ore mineralogy, ore genesis and parameters required for minerals or metallurgical processing (Fonteneau et al., 2013; Kyle and Ketcham, 2003), the technique is more problematic when dealing with high density ore samples (Bam et al., 2016).

XCT in high density ore samples has a number of challenges. High density samples are defined here as those ores with a specific gravity greater than 3.5 that are typically comprised of high proportions of dense minerals such as the metal sulphides (e.g. pyrite, chalcopyrite, galena) and / or metal oxides (e.g. magnetite, chromite, hematite). The two most important of these challenges in XCT are the lack of exact compositional information and beam hardening (Bam et al., 2019; Cnudde and Boone, 2013). XCT provides grey-value information where the grey values correspond to mineral compositional information which is a function of the mineral's linear attenuation coefficient. The assigning of grey values to different minerals relies on the user knowing the identity of the minerals present in the sample and which grey values

## CHAPTER 1: Introduction

correspond to which minerals (Cnudde et al., 2006) since the XCT does not provide compositional information in the way that SEM-EDS type platforms do. The difficulties come when one has samples with different mineral assemblages. As an example, for a sample that contains the minerals quartz, plagioclase, biotite and garnet, each of these minerals has a specific grey value and a grey value ratio with respect to density. If however, another sample contains the mineral assemblage quartz, plagioclase and biotite with no garnet, the grey value ratio with respect to density for each mineral will stay the same but the grey values themselves will change. In this situation, so long as the user knew that garnet was missing, they would still be able to work out which mineral corresponded to which grey value. However, beam hardening results in changes to both the grey values and the grey value ratios, meaning that identification of minerals in XCT can be challenging where beam hardening is a factor.

Beam hardening occurs when the lower X-ray energies of the polychromatic beam are more absorbed as they pass through the sample than the higher X-ray energies resulting in a more energetic X-ray beam hitting the detector (Alles and Mudde, 2007; Bucher et al., 2016; Van de Casteele et al., 2002). Beam hardening is most acute when dealing with high density ore samples. It creates artefacts that result in different grey values for the same minerals and this affects the quality of mineralogical information that can be extracted (Ketcham and Carlson, 2001). The problem becomes more pronounced as the sample size increases but this can, to some extent, be circumvented by increasing scanning times. However, longer scanning times would limit the possibility of the technique being employed routinely on a mining site to provide rapid mineralogical and textural information. Scanning times could be decreased by decreasing the sample size in order to facilitate better X-ray penetration which reduces beam hardening. By doing so, it would also improve the resolution of the image information. The resolution capability of the system determines the level of details that can be analysed within the ore sample and in most cases it is a function of the sample size itself (Jerram and Higgins, 2007). However, when dealing with high density ore samples it is difficult to know the optimal sample size because the impact of beam hardening and its extent on mineralogical grey value change is also unknown. Due to this there is a need for new scanning protocols and analysis methods to optimize scanning parameters and the quality of the quantified mineralogical and textural information when dealing with high density ore samples. With continuous development of computer power, big data analysis, detector efficiencies as well as the development in optics to provide highly focused X-ray beams to improve spatial resolution, the XCT technique has the potential in the next few decades to find wide spread routine use in mineralogical analysis, and possibly ultimately even replace the 2D techniques.

This study addresses these issues by examining the need for development of such methods and protocols and focusses on three main issues. The first is the need for methods to determine optimal scanning parameters to obtain mineralogical and textural information rapidly of any ore type. The second is the need to evaluate optimal sample sizes for different ore types based on density to minimize the loss of mineralogical and textural information due to beam hardening. Thirdly, the need for a simplified approach to improving the discrimination of minerals with similar densities to optimize the quantification of grain size distribution particularly for sulphide ores. For this last issue, the focus of this study is on optimisation of dual energy scanning methods to facilitate mineral discrimination in higher density samples. The methodological developments presented here represent an important advance in the way in which XCT can be used to quantify mineralogical and textural characteristics of ore deposits. These developments represent important

## CHAPTER 1: Introduction

steps towards the longer term goal of implementing XCT as a routine, rapid, reliable and, eventually, accurate analytical technique in the minerals processing industry.

### 1.1. Problem Statement

With the increasing mineralogical complexity and variability of low grade ores and the technical challenges associated with the mining and processing of such ores, there is an increasing demand for upfront ore body knowledge of the mineralogy and texture of these ores. To achieve this the mining and minerals industry needs the ability to obtain rapid and robust information on ore mineralogy and 3D texture and the variation thereof, for effective mine planning and optimisation of ore processing. XCT has potential to provide this 3D mineralogical and textural information. However, the application of XCT to different ore types has to be optimized in order to address the inherent limitations of the XCT technique when applied to high density ores. This includes the differentiation of minerals with similar attenuation behaviour, the impact of beam hardening, and the role of sample size and the use of dual energy scanning. Each of these issues requires the development of specific scanning protocols tailored to high density ores.

### 1.2. Aims of the Study

This project aims to develop methods and protocols to improve the quantification of 3D sample information using XCT and to overcome beam hardening artefacts associated with high density ore samples. To do this a number of objectives and key questions have been developed.

#### Chapter 2: Key Objective:

To build an attenuation coefficient data bank in order to predict mineralogical discrimination in high-density ores using XCT.

- 1.1. What is the minimum attenuation coefficient difference required in order to differentiate two minerals using XCT?
- 1.2. What is the impact of density on the minimum attenuation coefficient difference between two minerals?

#### Chapter 3: Key Objective:

To determine the optimal scanning parameters to quantify mineralogical and textural information in high density ore samples.

- 2.1. Which scanning parameter variables have the most impact on mineralogical and textural information obtained from XCT scanning?
- 2.2. What is the interdependence of scanning parameter variables in order to generate optimal mineralogical and textural information?
- 2.3. What is the relationship between optimal scanning parameters and rapid scanning parameters?

#### Chapter 4: Key Objective

## CHAPTER 1: Introduction

To develop a method that identifies the degree of loss of sample information due to beam hardening in high density ores.

- 3.1. How can loss of sample information in high density samples be recognised?
- 3.2. What is the impact of sample size on loss of information?
- 3.3. By what mechanism can loss of sample information be quantified?

**Chapter 5: Key Objective**

To develop a new approach to the dual energy method that optimizes the discrimination of mineralogical information in high density ore samples.

- 4.1. What are the factors that influence the application of dual energy to differentiate minerals of similar attenuation coefficient?
- 4.2. What is the best method for routine application of dual energy to differentiate minerals with similar attenuation coefficients?
- 4.3. Is there a limit to the ability of dual energy scanning to differentiate minerals with similar attenuations coefficients?

**Chapter 6: Key Objective**

To demonstrate the practical application of scanning methods and protocols developed in this study for high density ores and their relevance to the minerals processing industry.

- 5.1. How reliable is the mineralogical and textural information generated by the scanning protocols developed in this study?
- 5.2. What additional steps or developments would be needed to further improve the mineralogical and textural information obtained by XCT on high density samples?
- 5.3. What is the long term feasibility of implementing XCT as a standard analysis technique for the minerals processing value chain?

**1.3. Project Scope – Sample Selection**

Although this study discusses mineralogical and textural information in ore samples, all the samples used in this study are derived from drill core and are analysed as drill core with the exception of the Witwatersrand Basin samples in Chapter 5 which were extracted from drill core. Drill core is the most amenable sample type for XCT because it gives a regular shape. In contrast, “grab” samples have very irregular shapes and sizes and this would introduce an additional element of uncertainty into the scanning. Additionally whilst the project deals with high-density samples, the study uses only two different types of high-density ores: (1) iron ores and (2) base metals sulphides. These two types of ores though are probably representative of most high-density ores. The samples used in this study come dominantly from South Africa. However, iron ore samples from Brazil and Sweden were also examined.

#### 1.4. Thesis Outline

This thesis is written as a series of papers, each one building on the previous. The papers have the common theme of optimizing the differentiation of minerals in order to optimally quantify mineralogical and textural information in high density samples.

Chapter 2 discusses the importance of knowing the mineralogical makeup of samples prior to XCT scanning by determining the linear attenuation coefficient of each mineral in order to optimize the discrimination of minerals by selecting an appropriate X-ray energy for scanning. The importance of knowing the exact cation composition prior to scanning, as well as the limitations of single energy scanning and the advantages of the dual energy scanning approach is discussed. The goal is to determine which mineral pairs can and cannot be differentiated using XCT.

Once it has been established that it is possible to differentiate two minerals, the next step is to determine what the optimal scanning parameters for doing this are, and this is the subject of Chapter 3. The chapter demonstrates that the optimal scanning conditions for rapid scanning of high density ores can be identified by comparing different combinations of the scanning parameters (X-ray energy, current, number of images, exposure time) to produce an image with a high signal to noise ratio. This means that the ability of XCT to provide 3D mineralogical and textural information rapidly, positions the technique as a potential analytical tool for implementation on mining sites. This capability will also broaden the application of XCT from drill core logging, to ore characterisation, and through to minerals processing.

Even with optimal scanning parameters determined though, it is important to recognise that some information can be lost from the scanned data due to beam hardening. Chapter 4 explores this issue and focusses on the fact that beam hardening can result in loss of sample information that cannot be identified and quantified because it is not known that it is lost. A method for assessing loss of information is proposed using an aluminium standard sample to determine a %Error associated with a loss of sample information based on sample size. Reliable results have important implications for minerals processing because a loss of sample information may bias ore characterisation, and consequently lead to incorrect interpretations of the efficiencies and deficiencies in minerals processing circuits.

However, even when the attenuation coefficients of the minerals suggest they can be discriminated, and the optimal scanning parameters have been identified and the loss of information due to beam hardening has been quantified, it may still be challenging to differentiate particular mineral pairs because of similarities in their attenuation coefficients. In this situation, it may be necessary to utilise dual energy scanning to improve the differentiation and this is the focus of Chapter 5. The approach uses both scanned information and simulated information to better discriminate minerals because a simulated image assumes a monochromatic X-ray beam which overcomes the impact of beam hardening. The method is illustrated by differentiating chalcopyrite from pyrite and magnetite.

Chapter 6 presents two case studies where the above methods and protocols are used to quantify porosity in iron ore samples and chalcopyrite grain size distribution (GSD) in a base metal sulphide ore sample. The quantified porosity information in the iron ore samples were validated against the QEMSCAN (2D) data and the results are in agreement expect for one iron ore sample which has a non-uniform distribution of the porosity information which affects the representation of the 2D analysed data. In the base metal sulphide sample, the chalcopyrite grains were first discriminated from pyrite grains using the



## CHAPTER 1: Introduction

simplified dual energy method discussed in chapter 5, where after the chalcopyrite GSD was quantified. The case studies highlight both the advantages and limitations of the various methods being implemented.

The thesis concludes with an assessment of the main findings of the study as well as an evaluation of the practicalities of implementing these on a mine site.

### 1.5. Statement of Novelty

- a) This thesis has developed an approach to select the optimal XCT scanning parameters in high density ores in order to obtain mineralogical and textural information rapidly by using the signal-to-noise ratio (SNR) as a guideline.
- b) A method to indirectly quantify the impact of beam hardening and resultant loss of sample information in high density ore samples was developed. The method allows the user to determine the optimal sample size that is not associated with loss of information by using an aluminium standard sample to quantify %Error that assess the impact of beam hardening. Without the use of a standard sample this loss of information cannot be effectively evaluated and hence cannot be effectively corrected.
- c) A modified approach for the dual energy method, tailored for high density ores, has been developed to differentiate minerals with similar attenuation coefficients. The method addresses the issue of beam hardening artefacts while still optimizing the discrimination of minerals using a time effective approach by combining scanned images with simulated images as compared to the traditional dual energy method which relies on two scanning conditions.

### 1.6. Fundamentals of X-ray Computed Tomography

XCT is the core technique used in this study. Hence it is appropriate to give a review of the background to XCT to provide context for the later chapters. As the thesis has been written as a series of manuscripts, this information is not appropriate to include in subsequent chapters.

#### 1.6.1. Overview

X-rays were discovered in 1895 by Wilhelm Conrad Röntgen and this led to a successful development of imaging technologies (medical and technical). This discovery led to the first development of the X-ray imaging device that had X-ray tubes, X-ray films and later incorporated X-ray detectors. The advancement in computer technology in the 1960s and 1970s led to the development of X-ray computed tomography (XCT) techniques (Hampel, 2015). XCT is a non-destructive technique that acquires 2D projections in a 360° angular rotation to reveal internal structures of any object of interest (Schuetz et al., 2013). The 2D projections or radiographs are made of pixels that record the average grey values of objects within the samples as the X-ray beam passes through. The analysis of objects in 2D radiographs has limitations due to overlap or a lack of contrast between objects (Stock, 2011). However, the utilisation of mathematical principles of tomography to reconstruct 2D projections produces a 3D digital volume where each voxel represents the X-ray attenuation or absorption at any given x, y and z position. This means that the 3D volume can be viewed from different 2D image slices (Landis and Keane, 2010) sometimes referred to as front, top and right view. Due to the relationship that exists between X-ray absorption and density, the technique provides accurate representation of different phases within the sample due to different responses in X-ray absorption (Stock, 2011). Phases with similar response in X-ray absorption will be difficult to



## CHAPTER 1: Introduction

discriminate from each other. Initially XCT was used for medical applications (Landis and Keane, 2010; Wang et al., 2018) but the improvement of key components extended the technique to industrial application due to better imaging of material densities greater than that of human tissue (Sato et al., 2018; Landis and Keane, 2010). For industrial application there are two types of XCT systems, those focusing on high penetrating capability and those with high spatial resolution capability which are both referred to as micro-focus XCT systems (Wang et al., 2018). The development of high spatial resolution systems led to the interrogation of material microstructures and this is complementary to 2D microscopy systems (Landis and Keane, 2010).

### 1.6.2. Different XCT Systems

XCT imaging was initially considered as a reconstruction of a thin slice from line integrals in order to reveal material structures within an object. The line integrals in XCT are acquired through the measurements of X-ray beam intensities with a set X-ray beam voltage or energy. Such X-ray beams generate from a focal spot size on a target material of the tube and detected on the other side of an object by an active area of a detector. In order to have a full representation of an object the detector together with the line integrals must be positioned in different places. Figure 1.2 demonstrates improving technology and complexity of the medical XCT which classifies different generations of XCT scanners (Hampel, 2015).

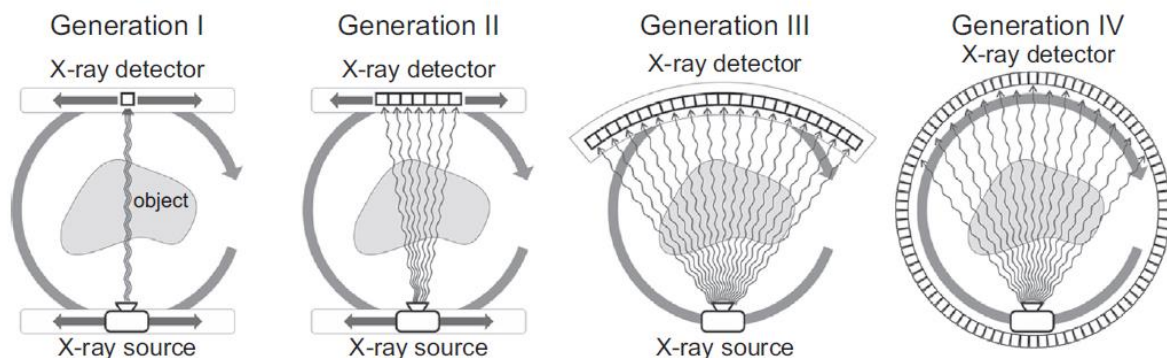


**Fig 1.2.** Different generations of X-ray computed tomography medical scanners with different designs.

The first generation of the medical XCT scanners were referred to as pencil beams that belonged to a generation of devices that used a parallel X-ray beam. This type of scanner has two movements: a) a lateral movement responsible for a single projection and b) a circular movement responsible to gather all the projections needed to reconstruct an image. This type of scanner acquired projections either continuously or discretely. The advancement of detector technology in 1972 led to the second generation of scanners with multiple detector arrays. This generation of scanners had a detector ranging from 3 to 52 (detectors) in the array and were referred to as a partial fan beam. The fan beam allowed the projections to cover a wider area of an object which resulted to a fewer number of projections required to reconstruct an image (Cierniak, 2011). The introduction of the third generation of scanners was directed towards limiting the lateral movement of the detector system and the X-ray source. This was achieved in the mid 70's by the XCT designers who managed to limit the movement only to rotational movement. This generation of scanners was called the fan beam scanner which refers to a beam with a fan shape and an angular spread ranging from 40 to 55 degrees which covers the whole test object. Introducing this scanner addressed the need to increase the number of detectors (up to 1000 detector elements) together with a rotating target (X-

## CHAPTER 1: Introduction

ray tube). The introduction of the fourth generation of XCT scanners in the late 70's differed from the previous (third) generation with more detector elements (from 600 up to 5000). This scanner had a rotating target and a stationary detector (Cierniak, 2011).

The development of the first medical XCT scanner led to the concept of cone beam computed tomography (CBCT) (Pauwels et al., 2015). CBCT was first dedicated for angiography but the application extended to radiotherapy planning, mammography and cardiology (Scarfe and Farman, 2008; Pauwels et al., 2012). It has been applied in medicine since the 1980s but the first commercial CBCT was introduced in 1998 (Pauwels et al., 2012). The term cone beam refers to a cone geometrical shaped X-ray beam (Abramovitch and Rice, 2014). The system was developed as an alternative to the medical CT scanners using the fan beam as mentioned above. This was done to rapidly acquire object images filling up the whole field of view of (FOV) a detector with high level of details (Scarfe and Farman, 2008; Pauwels et al., 2012) which is one of the advantages of the CBCT systems. The other advantage of the systems is that it has a low-radiation X-ray source with a focused X-ray beam that delivers relative high spatial resolution and has less scattering as compared to the fan beam systems (Palomo et al., 2006). The high resolution capability is due to a smaller focal spot size of about 0.5mm while the total radiation of the source is about 20% of that of a medical XCT. The CBCT systems have two significant differences compared to the medical XCT scanners: a) it utilises a low-energy tube and b) the system rotates once around the area of interest to obtain the data. These differences allows the CBCT systems to be less expensive and smaller in size compared to the medical scanners (Palomo et al., 2006; Quereshy, Savell and Palomo, 2008).

### 1.6.3. *XCT Configuration*

There are several significant differences between a medical XCT and a micro-XCT ( $\mu$ XCT). With the medical XCT systems an object is kept stationary whilst the detector and the X-ray tube moves around an object. The opposite is observed in a  $\mu$ XCT systems by allowing the object to rotate whilst the detector and the X-ray tube remain stationary. This configuration is optimal, especially for high resolution scanning, in order to achieve stability. The laboratory  $\mu$ XCT based systems generate X-ray beams from a finer focal spot size, which is a requirement for high resolution scanning, and consists of a detector that determines the dynamic range of an image. This setup has a cone beam shape (similar to CBCT) which allows magnification (geometrical) of an object under investigation (Fig. 1.3). Higher magnification is achieved by placing an object close to the X-ray tube which reveals finer structures within an object. The focal spot in this setup determines the highest achievable resolution ( $< 1 \mu\text{m}$ ) but requires a lower X-ray flux which increases the acquisition time for lab-based setups. These systems provide higher dynamic ranges due to a thick scintillator screen that comes with a flat panel detector. For high flux tubes, X-ray optics (lenses) are required in order to obtain high resolution (Cnudde and Boone, 2013). It is important to mention that recent developments in  $\mu$ XCT have adopted designs similar to medical XCT where a sample remains stationary whilst the detector and the X-ray tube rotate around the sample. These types of systems are designed to image dynamic processes where a sample is connected to different equipment to study processes like fluid flow (Bultreys et al., 2016). The sample is kept stationary to avoid any disturbance to the equipment connected to the sample. However, these types of systems are not common in most laboratories.

## CHAPTER 1: Introduction

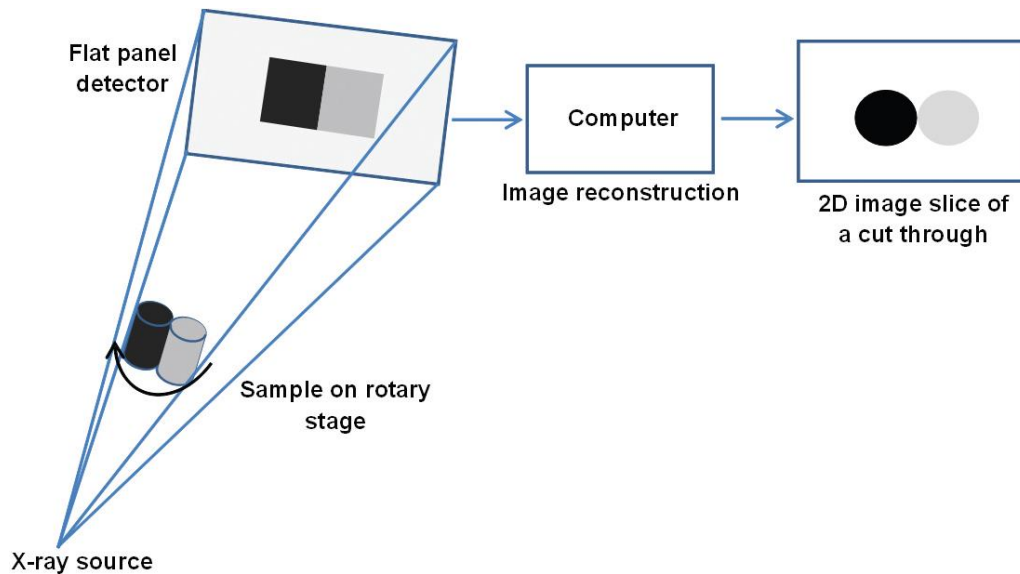


**Fig 1.3.** A schematic diagram of a common lab-based  $\mu$ XCT setup with a conical X-ray beam which allows a geometrical magnification.

#### 1.6.3.1. X-ray Source

The X-ray tube forms an important part of any XCT system and its operation depends on the X-ray interaction with the target material of interest (Cierniak, 2011) in order to produce X-rays. The important parameters of the X-ray source are the size of the focal spot, the energy spectrum of the generated X-rays and the intensity of the X-rays. The spot size determines the highest achievable spatial resolution of the XCT instrument or system. The energy spectrum determines the capability of the X-rays to penetrate through the sample of a given density. There is a high probability for high X-ray energies to penetrate high density samples compared to low density samples (Ketcham and Carlson, 2001). However, when the sample is larger or its density and attenuation coefficient are too high (e.g. iron ore, barite samples, etc) even the high X-ray energies struggle to penetrate the sample. This emphasises the importance of optimal sample size in such cases, and utilisation of higher X-ray intensities and appropriate filter materials to improve X-ray penetration. However, care should be considered when using higher X-ray intensities because they often require a larger focal spot size that can affect the scanning resolution especially for smaller dense or highly attenuating samples.

When X-rays penetrate through the sample they are attenuated by scattering and absorption. During the process of X-ray beam attenuation three physical processes dominate: 1) photoelectric effect, 2) Compton scattering and 3) pair production. During the photoelectric effect process, an inner electron is ejected due to an incident photon transferring all its energy to it. During the Compton scattering process, the outer electron is ejected by the incoming X-ray photon. The incoming X-ray photon then loses part of its energy causing it to be deflected and change direction. In pair production, two electrons with opposite charges are produced due to an interaction of an X-ray photon with a nucleus. For geological samples, the dominant process in the photoelectric effect between 50 – 100keV X-ray energy. Compton scattering process dominates at higher X-ray energies (5 – 10MeV) and beyond this the pair production process takes over. Lab-based XCT systems only consider the photoelectric effect and Compton scattering process due to their low X-ray energy capability (Ketcham and Carlson, 2001).

## CHAPTER 1: Introduction

1.6.3.2. *Detectors*

The current laboratory based XCT systems, with a flat panel detector, uses two main detection principles, direct and indirect sensors that convert X-rays to light. The flat panel detectors with indirect systems consists of layers of scintillators and photodiode matrices. X-rays in the keV energy range are converted to visible light within the layers of the scintillator and each X-ray photon is responsible for ~1000 visible light photons being produced. The flat panel detector photodiodes can have up to 4000 x 4000 matrices of pixels arrangement with the best technology (amorphous silicon technology). Different types of scintillator materials are used depending on the scanning parameters (resolution, X-ray energy range and current). In a case where higher X-ray energies (50 and 200keV) are used, the thickness of the scintillator can affect the efficiency of detection due to the lower X-ray flux. The resolution on the other hand decreases with increasing thickness of the scintillator layer which requires an optimised photodiode and scintillator combination. This is why scintillators like caesium iodide are utilised because they prevent the degradation of the signal through the scintillator path. The flat panel detector pixel size can go down to 50  $\mu\text{m}$  which defines the sample distance limit of the X-ray image projected on the detector plane. When a lower X-ray energy is required to scan smaller samples, detectors with smaller pixel sizes of about 6.5  $\mu\text{m}$  with adequate spatial resolution and good efficiency are available on the market (Hanke et al., 2016).

1.6.3.3. *Limitation of XCT to Study Methodology*

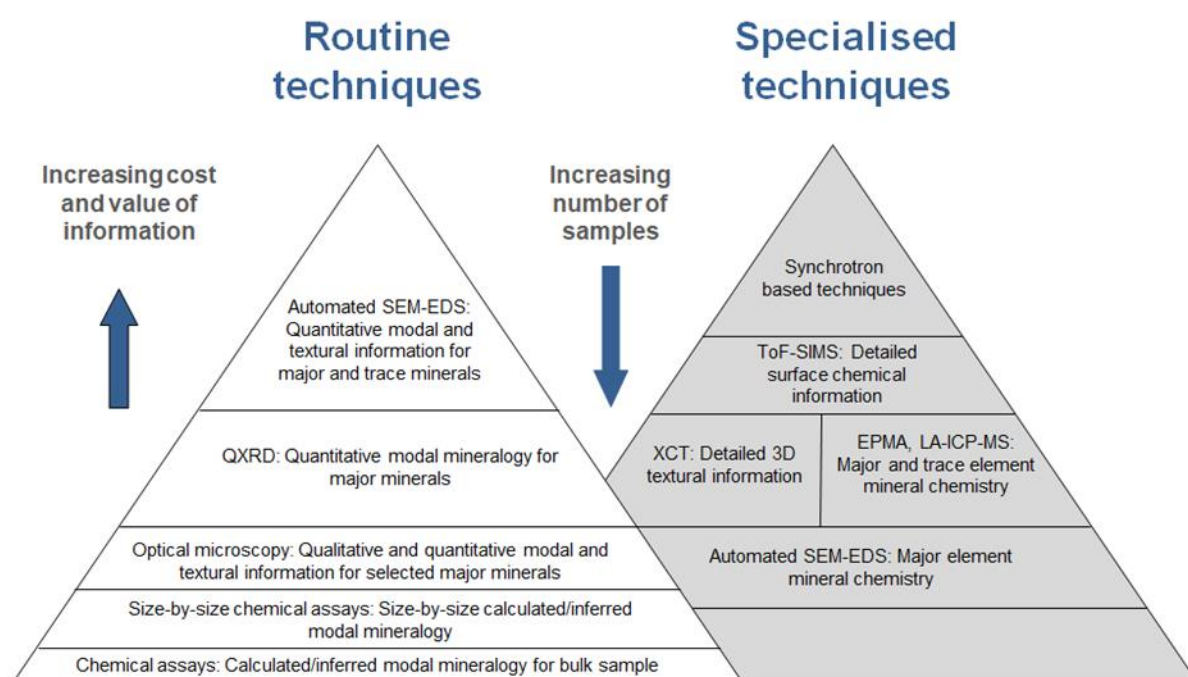
Despite the 3D capability of XCT, which is the main attraction compared to 2D techniques like SEM and QEMSCAN, it has disadvantages as well. One of the major disadvantage of XCT is the polychromatic nature of the beam which leads to beam hardening when scanning larger or denser samples (density > 3g/cm<sup>3</sup>). To minimise this effect, the samples have to be scanned at higher X-ray energies. This is a problem when the sample contains a range of minerals that require a lower X-ray energy to optimise the discrimination between them. This is also a problem when larger samples have to be scanned to obtain meaningful representation of mineralogical and textural information (e.g. grain size distribution). In such a case the sample has to be cut to smaller sizes resulting to multiple scanning which is time consuming. However, smaller sample sizes allow sufficient X-ray penetration, which minimises loss of sample information, and the utilisation of lower X-ray energies, which optimises mineral discrimination or sample contrast. Another disadvantage of the beam is that the set voltage on the system is not equal to an effective X-ray energy of the beam. The effective energy can change depending on the filter material being used which makes it difficult to calculate the exact linear attenuation coefficient of the minerals within the sample. The effective energy of the spectrum can also be affected by the dense sample matrix causing the minerals not to be discriminated due to resulting higher effective X-ray energy and noise within an image. High levels of noise affect the signal-to-noise ratio which is important for mineral discrimination. This is different from the synchrotron X-ray beam which is monochromatic in nature, provides optimal sample contrast, and does not suffer from beam hardening due to its high flux.

In addition to the disadvantages or limitations mentioned above, the resolution is an issue as well which is inherent to the technique. Most laboratory based systems can go down to 3 – 5 $\mu\text{m}$  which makes it difficult to compare high resolution information provided by the 2D techniques with the XCT or  $\mu\text{XCT}$  techniques. This is a major set-back because to obtain high resolution information requires a smaller sample size. Despite the utilisation of smaller sample sizes, the XCT technique provides coarse grain information and the majority of the information is below the resolution capability making it difficult to quantify the full spectrum of the mineralogical information of the sample. The information below the resolution results in mineral or grey

value overlap which affects the true grey values of the minerals. This decreases or increases the actual grey values of the minerals of interest depending on the linear attenuation coefficient of those minerals. This affects the discrimination and quantification of minerals which can lead to misrepresentation of the actual mineralogical information.

### 1.7. Minerals Processing and Process Mineralogy

The focus of this thesis is on the development and application of XCT methodologies and protocols for obtaining mineralogical and textural information on high-density ore samples. These applications also have relevance to the minerals processing industry. Minerals processing also known as ore dressing, or minerals engineering is the separation and concentration of valuable metallic and non-metallic minerals from waste material, also known as gangue (Willis and Napier-Nunn, 2005; Haldar, 2018). It follows after mining and prepares the ore for the hydro- or pyrometallurgical extraction of the valuable metals to produce a commercial end product. Process mineralogy on the other hand is the study of mineralogical characteristics that impact on minerals processing (Becker et al., 2016). This study looks at the application of XCT to process mineralogy. However, a brief review of minerals processing is also warranted to provide additional context to the study. There are three main activities in mineral processing: (1) liberation, (2) separation and concentration, and (3) extraction (Haldar, 2018). Liberation of the valuable minerals from the gangue is accomplished through comminution. This involves a series of crushing and or grinding stages to produce a particle size in which the valuable mineral is not encapsulated within the gangue, and is in an appropriate size range for the desired separation process (Evans and Morrison, 2016). Valuable minerals cannot be efficiently recovered by downstream separation processes if they are not adequately liberated. Separation entails the concentration of the valuable mineral to produce a concentrate and a discard or tailings product. Separation processes include flotation, gravity, magnetic, and optical separation. However, in some circumstances, the concentrate may not be of sufficiently high grade and additional fine grinding is needed to further liberate valuable minerals prior to concentration, or valuable minerals are lost to the tailings because they were not sufficiently liberated prior to processing.





## CHAPTER 1: Introduction

**Fig 1.4.** Different analytical techniques to quantify mineralogical and textural information (Becker et al., 2016)

Alternatively there may be some deleterious minerals or elements that interfere with the efficiency of the separation process and contaminate the concentrate (Cropp et al., 2013). Mineralogical and textural information is critical to the design of these mineral processing circuits, their optimisation, benchmarking and trouble-shooting (Lotter et al., 2018). There are a wide range of analytical techniques that are, and have been used, to do this (Fig. 1.4). These techniques can be divided between routine analytical methods such as QXRD (quantitative X-ray diffraction), chemical assays and automated SEM-EDS (scanning electron microscopes with energy dispersive X-Ray spectrometry) systems, and more specialised techniques such as XCT, synchrotron and EMPA (Electron microprobe analysis). The techniques in the routine methods group, are readily available and have routine protocols to enable personnel at mines to obtain and interpret the information. In contrast, the methods under specialised are not easily accessible for various reasons including logistics and funding (there is currently no synchrotron in Africa), and require the development of routine methods and protocols for a variety of ore types (QEMSCAN - Quantitative Evaluation of Minerals by Scanning Electron Microscopy). However, of these XCT probably shows the most promise to be applied as a routine technique because the instrument itself is relatively straightforward to use. However, it requires the development of routine methods and protocols to facilitate its implementation in mineral processing applications. As previously indicated, this is the focus of this thesis.

## 1.8. References

- Abramovitch, K., and Rice, D. D., 2014. Basic principles of cone beam computed tomography, *Dental Clinics of North America*. 463–484. doi: 10.1016/j.cden.2014.03.002
- Akin, S., Kovscek, A.R., 2003. Computed tomography in petroleum engineering research. *Geol. Soc.* 215, 23–38. <https://doi.org/dx.doi.org/10.1144/GSL.SP.2003.215.01.03>
- Alles, J., Mudde, R.F., 2007. Beam hardening: Analytical considerations of the effective attenuation coefficient of X-ray tomography. *Med. Phys.* 34, 2882–2889. <https://doi.org/10.1118/1.2742501>
- Bam, L.C., Miller, A.J., Becker, M., Basson, I.J., 2019. X-ray Computed Tomography: Practical Evaluation of Beam Hardening in Iron Ore Samples. *Miner. Eng.* 131, 206–215. <https://doi.org/10.1016/j.mineng.2018.11.010>
- Bam, L.C., Miller, J.A., Becker, M., Beer, F.C. De, Basson, I., 2016. X-ray Computed Tomography – Determination of Rapid Scanning Parameters for Geometallurgical Analysis of Iron Ore, in: *Proceedings of the Third AusIMM International Geometallurgy Conference*. Perth, pp. 209–219.
- Becker, M., Wightman, E.M., Evans, C.L., Julius Kruttschnitt Mineral Research Centre, Y., 2016. Process mineralogy. Julius Kruttschnitt Mineral Research Centre.
- Becker, M., Jardine, M.A., Miller, J.A., Harris, M., 2016. X-ray Computed Tomography: A geometallurgical tool for 3D textural analysis of drill core? *Proc. 3rd AusIMM Int. Geometallurgy Conf.* 15–16.
- Bucher, A.M., Wichmann, J.L., Schoepf, U.J., Wolla, C.D., Canstein, C., McQuiston, A.D., Krazinski, A.W., De Cecco, C.N., Meinel, F.G., Vogl, T.J., Geyer, L.L., 2016. Quantitative evaluation of beam-hardening artefact correction in dual-energy CT myocardial perfusion imaging. *Eur. Radiol.* 26, 3215–3222. <https://doi.org/10.1007/s00330-015-4137-x>
- Bultreys, T., Boone, M.A., Boone, M.N., De Schryver, T., Masschaele, B., Van Hoorebeke, L., Cnudde, V., 2016. Fast laboratory-based micro-computed tomography for pore-scale research: Illustrative experiments and perspectives on the future. *Adv. Water Resour.* 95, 341–351. <https://doi.org/10.1016/j.advwatres.2015.05.012>
- Cierniak, R., 2011. X-ray computed tomography in biomedical engineering, *X-Ray Computed Tomography in Biomedical Engineering*. <https://doi.org/10.1007/978-0-85729-027-4>
- Cropp, A.F., Goodall W.R., Bradshaw D.J., 2013. The Influence of Textural Variation and Gangue Mineralogy on Recovery of Copper by Flotation from Porphyry Ore – A Review. In: *2nd International Geometallurgy Conference*. AusIMM, Brisbane, Australia, pp 279–291
- Cnudde, V., Boone, M.N., 2013. High-resolution X-ray computed tomography in geosciences: a review of the current technology and applications. *Earth Sci. Rev.* 123, 1–17. <https://doi.org/10.1016/j.earscirev.2013.04.003>

## CHAPTER 1: Introduction

- Cnudde, V., Masschaele, B., Dierick, M., Vlassenbroeck, J., Hoorebeke, L. Van, Jacobs, P., 2006. Recent progress in X-ray CT as a geosciences tool. *Appl. Geochemistry* 21, 826–832. <https://doi.org/10.1016/j.apgeochem.2006.02.010>
- Evans, C.L., Wightman, E.M., Yuan, X., 2015. Quantifying mineral grain size distributions for process modelling using X-ray micro-tomography. *Miner. Eng.* 82, 78–83. <https://doi.org/10.1016/j.mineng.2015.03.026>
- Evans, C.L., Morrison, R., 2016. Mineral Liberation. In: Becker M, Wightman EM, Evans CL (eds) *Process Mineralogy: JKMRC Monograph Series in Mining and Mineral Processing*, No 6. Julius Kruttschnitt Mineral Research Centre, Brisbane, Australia Fonteneau, L.C.P.J., Gobel, B., Ramanaidou, E.R., 2013. Application of High-Resolution X-ray Computed Tomography to Iron Ore Characterisation, in: *Iron Ore Conference*
- Forsberg, F., Hjortsberg, E., 2012. X-ray microtomography for sequential imaging and analysis of iron ore pellets under reduction, in: *Sixth International Congress on the Science and Technology of Ironmaking*. pp. 1744–1753.
- Haldar, S.K., 2018. Mineral Processing, in: *Mineral Exploration*. Elsevier, pp. 259–290. <https://doi.org/10.1016/B978-0-12-814022-2.00013-7>
- Hampel, U., 2015. X-ray computed tomography, in: *Industrial Tomography*. Woodhead Publishing, pp. 175–196. <https://doi.org/10.1016/B978-1-78242-118-4.00006-X>
- Hanke, R., Fuchs, T., Salamon, M., Zabler, S., 2016. X-ray Microtomography for Materials Characterization, *Materials Characterization Using Nondestructive Evaluation (NDE) Methods*. Elsevier Ltd. <https://doi.org/10.1016/B978-0-08-100040-3.00003-1>
- Jerram, D.A., Higgins, M.D., 2007. 3D Analysis of Rock Textures : Quantifying Igneous Microstructures. *ELEMENTS* 3, 239–245.
- Johnson, R.C., Scott, G.W., Lukey, H.M., 2007. Implications of Mineralogy , Grain Size and Texture on Liberation and Pellet Quality of Great Lakes Iron Ore. *Iron Ore Conf.* 109–11
- Ketcham, R.A., Carlson, W.D., 2001. Acquisition , optimization and interpretation of X-ray computed tomographic imagery : applications to the geosciences. *Comput. Geosci.* 27, 381–400
- Kyle, J.R., Ketcham, R.A., 2003. In situ distribution of gold in ores using High-resolution X-ray computed tomography. *Econ. Geol.* 98, 1697–1701.
- Landis, E.N., Keane, D.T., 2010. X-ray microtomography. *Mater. Charact.* 61, 1305–1316. <https://doi.org/10.1016/J.MATCHAR.2010.09.012>
- Miller, J.D., Lin, C.L., Garcia, C., Arias, H., 2003. Ultimate recovery in heap leaching operations as established from mineral exposure analysis by X-ray microtomography. *Int. J. Miner. Process.* 72, 331–340. [https://doi.org/10.1016/S0301-7516\(03\)00091-7](https://doi.org/10.1016/S0301-7516(03)00091-7)
- Palomo, J. M., Kau, C. H., Bahl, L., Hans, M. G., 2006. Three-dimensional cone beam computerized tomography in dentistry, *Dentistry Today*, 9, 130–135
- Pauwels, R. *et al.* (2012) Future prospects for dental cone beam CT imaging, *Imaging in Medicine*, 4, 551–563. doi: 10.2217/iim.12.45
- Pauwels, R., Jacobs, R., Bosmans, H., Schulze, R., 2015. Technical aspects of dental CBCT: State of the art, *Dentomaxillofacial Radiology*. British Institute of Radiology, 1–20. doi: 10.1259/dmfr.20140224
- Prior, T., Giurco, D., Mudd, G., Mason, L., Behrisch, J., 2012. Resource depletion, peak minerals and the implications for sustainable resource management. *Glob. Environ. Chang.* 22, 577–587. <https://doi.org/10.1016/j.gloenvcha.2011.08.009>
- Quereshy, F. A., Savell, T. A., Palomo, J. M., 2008. Applications of Cone Beam Computed Tomography in the Practice of Oral and Maxillofacial Surgery, *Journal of Oral and Maxillofacial Surgery*, 66, 791–796. doi: 10.1016/j.joms.2007.11.018
- Rozendaal, A., Le Roux, S.G., du Plessis, A., Philander, C., 2018. Grade and product quality control by microCT scanning of the world class Namakwa Sands Ti-Zr placer deposit West Coast, South Africa: An orientation study. *Miner. Eng.* 116, 152–162. <https://doi.org/10.1016/j.mineng.2017.09.001>
- Sato, K., Abe, M., Takatsuji, T., 2018. Development of high-energy and high-resolution X-ray CT. *Precis. Eng.* 54, 276–283. <https://doi.org/10.1016/J.PRECISIONENG.2018.06.004>
- Scarfe, W. C., Farman, A. G., 2008. What is Cone-Beam CT and How Does it Work?, *Dental Clinics of North America*, 52, 707–730. doi: 10.1016/j.cden.2008.05.005
- Schuetz, P., Miceli, A., Jerjen, I., Flisch, A., Hofmann, J., Broennimann, R., Sennhauser, U., 2013. Reducing environmental scattering in industrial computed tomography by system redesign. *NDT E Int.* 58, 36–42. <https://doi.org/10.1016/j.ndteint.2013.04.005>

## CHAPTER 1: Introduction

- Spencer, S., Sutherland, D., 2000. Stereological correction of mineral liberation grade distributions estimated by single sectioning of particles. *Image Anal Stereol Orig. Res. Pap.* 19, 175–182.
- Stock, S., 2011. *Microcomputed Tomography: Methodology and Applications*, 1st ed, Boca Raton: CRC Press. <https://doi.org/doi:10.1201/9781420058772.fmatt>
- Van de Casteele, E., Van Dyck, D., Sijbers, J., Raman, E., 2002. An energy-based beam hardening model in tomography. *Phys. Med. Biol.* 47, 4181–4190. <https://doi.org/10.1088/0031-9155/47/23/305>
- Van Geet, M., Swennen, R., Wevers, M., 2000. Quantitative analysis of reservoir rocks by microfocus X-ray computerised tomography. *Sediment. Geol.* 132, 25–36. [https://doi.org/10.1016/s0037-0738\(99\)00127-x](https://doi.org/10.1016/s0037-0738(99)00127-x)
- Wang, X., Meier, D., Taguchi, K., Wagenaar, D.J., Patt, B.E., Frey, E.C., 2011. Material separation in x-ray CT with energy resolved photon-counting detectors. *Med. Phys.* 38, 1534–1546. <https://doi.org/10.1118/1.3553401>
- Wang, Y., Li, C.H., Hu, Y.Z., 2018. Use of X-ray computed tomography to investigate the effect of rock blocks on meso-structural changes in soil-rock mixture under triaxial deformation. *Constr. Build. Mater.* 164, 386–399. <https://doi.org/10.1016/j.conbuildmat.2017.12.173>
- Wills, B.A., Napier-Munn, T., 2005. *Mineral Processing Technology*, Seventh Ed. ed. Elsevier Science & Technology Books. <https://doi.org/http://dx.doi.org/10.1016/B978-075064450-1/50000-X>
- Zhou, J., Gu, Y., 2016. Geometallurgical Characterization and Automated Mineralogy of Gold Ores, in: Adams, M.D. (Ed.), *Gold Ore Processing*. Elsevier, pp. 95–111. <https://doi.org/10.1016/B978-0-444-63658-4.00006-2>



---

**PAPER PUBLICATION HISTORY**

---

<b>Title</b>	A simple Tool to Calculate X-ray Linear Attenuation Coefficients to Assess Mineralogical Differentiation for X-ray Computed Tomography Scanning
<b>Journal</b>	Geosciences
<b>Status</b>	To be Submitted February 2020
<b>Authors and roles</b>	L Bam – PhD Candidate J Miller – Primary Supervisor M Becker – Secondary Supervisor
<b>Applicant Contribution</b>	Conceptualization, Formal analysis, Methodology, Writing—original draft & editing (90%).

---

# A simple Tool to Calculate X-ray Linear Attenuation Coefficients to Assess Mineralogical Differentiation for X-ray Computed Tomography Scanning

Lunga C. Bam<sup>1,3,\*</sup>, Jodie A. Miller<sup>1</sup> and Megan Becker<sup>2</sup>

1. Department of Earth Sciences, Stellenbosch University, Private Bag X1, Matieland 7601, South Africa; [jmiller@sun.ac.za](mailto:jmiller@sun.ac.za) (J.M.)
  2. Centre for Minerals Research, Department of Chemical Engineering, University of Cape Town, Private Bag, Rondebosch 7701, South Africa; [megan.becker@uct.ac.za](mailto:megan.becker@uct.ac.za)
  3. Department Radiation Science, Necsa, PO Box 582, Pretoria, South Africa
- \* Correspondence: [lunga.bam@necsa.co.za](mailto:lunga.bam@necsa.co.za)

## ARTICLE INFO

### Keywords:

X-ray computed tomography;  
Linear attenuation coefficient;  
Minerals;  
Effective X-ray energy

## ABSTRACT

X-ray computed tomography (XCT) is becoming one of the most important techniques in the geosciences. The technique relies on attenuation coefficient and density differences in order to reveal the internal structure of the rocks. To properly discriminate between minerals using the developed data bank (a simple tool) to calculate linear attenuation coefficient not only depends on the density and X-ray energy but most importantly the specific chemical formula. The elements within the chemical formula determine how the X-ray beam is attenuated. Analysis of a variety of scanned mineral pairs with similar densities and attenuation coefficients indicates that an attenuation coefficient difference of greater than or equal to 6% at 45.5keV effective X-ray energy is required for the effective application of XCT with single energy scanning. This means that mineral pairs, such as quartz and pyrophyllite cannot be discriminated using the current XCT instruments due to the fact that the attenuation coefficient difference is less than 1.9% at 45.5keV effective X-ray energy. Garnet minerals were used as examples to illustrate the importance of knowing the actual chemical formula of the mineral to demonstrate that they can be partially or fully discriminated from each other.

## 1. Introduction

X-ray computed tomography (XCT) is a non-destructive technique that utilizes X-rays to image the 3D internal structure of a wide variety of materials (Ketcham and Carlson, 2001; Mees et al., 2003; Momose and Keiichi, 1999). Soon after its development in the medical sciences in the 1970's (Kalender, 2006), it attracted considerable attention within the geosciences due to its potential to visualise the internal structure of rocks and minerals (Cnudde et al., 2006; Hamdani, 2015; Kyle and Ketcham, 2015). In particular, the ability of the technique to determine the mineral content, distribution of minerals, mineral texture, porosity and pore structure network, at a variety of scales, made it an attractive technique across diverse fields from petrology to palaeontology to minerals processing (Kaufhold et al., 2016; Mees et al., 2003; Miller et al., 2013; Panahi et al., 2012; Siddiqui et al., 2014). In particular, XCT has proven to be an important analytical technique for the analysis of drill cores, that lend themselves to XCT analysis because of their uniform sample geometry. Material

density (Ashi, 1997; Tanaka et al., 2011) as well as ore grade (Le Roux et al., 2015) have been successfully calculated from drill core using advanced segmentation methods. More recently, it has been proposed to combine GLCM with grey level co-occurrence matrices (GLCM) to generate algorithms that will automatically interrogate texture in 3D applications using drill core (Jardine et al., 2018)

XCT images record the difference in density by means of grey values that represent the linear attenuation coefficient of each and every mineral present within the specimen (Kyle and Ketcham, 2015; Mees et al., 2003). The interaction of X-rays with minerals depends not only on the mineral density (a function of mineral chemistry and atomic structure) but also on the thickness (grain size) and effective atomic number of the mineral. This means that if the density variation between the minerals present is large, the X-ray beam is attenuated differently, resulting in distinct grey values. This makes the XCT technique attractive to different material science disciplines. However, if the density difference between minerals is small, then it is difficult for the XCT technique to differentiate them

## CHAPTER 2: Attenuation Coefficients

because of similar attenuation response of the minerals resulting in similar grey values (Mees et al., 2003). Because of this, different combinations of minerals or mineral assemblages are more amenable to interrogation by XCT than others. In particular, some combinations of minerals or mineral pairs cannot be differentiated from one another because of the similarity in attenuation response. In such cases, it is important to know up front, the limitations of the XCT system with respect to the mineral assemblage or problem being worked with.

The objective of this paper is to present a simple way to evaluate whether different minerals can be differentiated on the basis of their linear attenuation coefficient through the development of an attenuation coefficient 'data bank'. The 'data bank' has been developed in the form of a user-friendly excel spreadsheet that can calculate linear attenuation coefficients at any effective energy (with any increment of choice) between 41.7 and 72.6keV which is equivalent to an X-ray energy spectrum of between 60 and 225keV. In comparison, the National Institute of Standards and Technology (NIST) online database calculates linear attenuation coefficients at specific energies (with predetermined increments up to 4 significant digits) which can obscure subtle differences at various energies that can be exploited for mineral differentiation. The NIST database also requires an online connection. The application of the excel spreadsheet is demonstrated by looking at several examples including high density iron-ore minerals, some of which cannot be differentiated by XCT.

## 2. Methodology

The development of the data bank involves several steps. The first step was to collect different energy spectrums of a tungsten target under a high voltage (kV) and convert them

into effective energies equivalent to a monochromatic beam of the X-Ray energy spectrum. This allows evaluation of how mineralogical grey value information is affected by scanning parameters, different filter materials, sample size and beam hardening by comparing the effective linear attenuation difference with the measured grey value difference. Tungsten is normally used as the target in these types of instruments because it has high flux and can withstand high temperatures. The second step was to determine the NIST database for attenuation and energy information for all elements from 41.7 to 72.6keV and compile this information into an excel spreadsheet. The third step was to develop the excel macros that take the compiled NIST elemental data and convert it to linear attenuation coefficients for any mineral.

### 2.1. Tungsten Energy Spectrum

Different energy spectrums of a tungsten target under a high voltage (kV) were collected using a germanium detector (Figure 2.1). The set voltage on the target is equivalent to the maximum energy of the produced spectrum. The spectrum consists of different proportions of various energies because of the polychromatic nature of the X-ray beam. The varying energy proportions interact differently with minerals thus making the associated linear attenuation coefficient calculations complex - minerals absorb more energy at the lower energy range compared to the higher energy range of the spectrum. To simplify the interpretation of the interaction of the X-ray spectrum with a mineral, an effective energy of the spectrum was calculated. An effective energy is a weighted average of an actual polychromatic beam. Although the effective energy has been assumed to be close to 30-40% of the peak energy (Sprawls, 1993), it is more accurate to calculate it for each spectrum.

## CHAPTER 2: Attenuation Coefficients

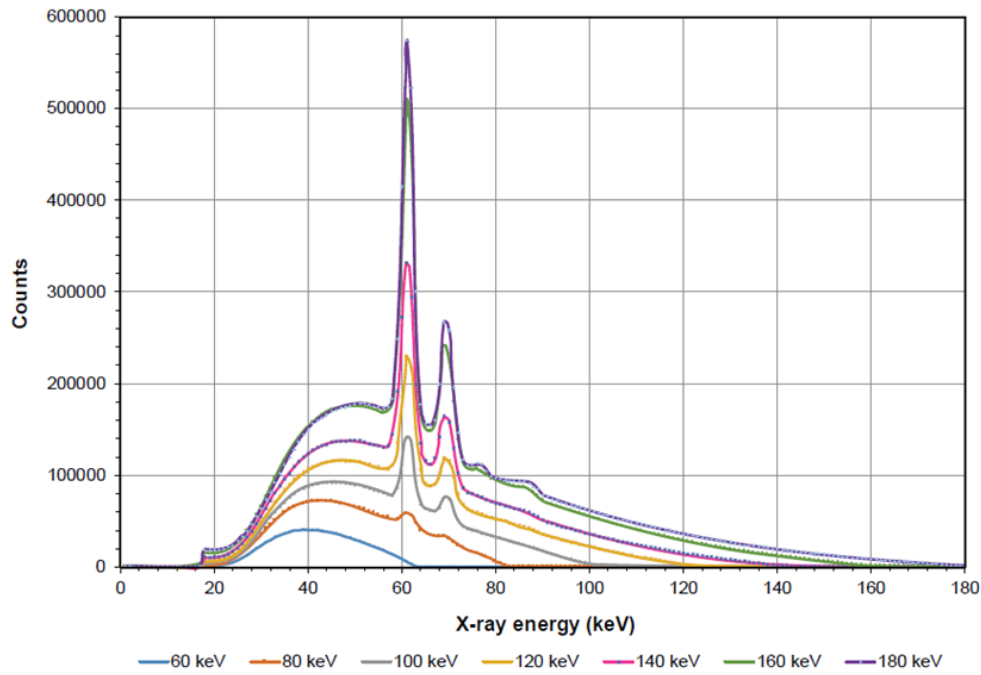


**Fig 2.1.** Different tungsten energy spectra collected at different energies.

One way to determine the effective energy is to use the aluminium half-value layer method (Matsubara et al., 2014; McCullough, 1975; Yada and Onishi, 2016). To do this, the effective energy is calculated by converting the X-ray energy spectrum from polychromatic to monochromatic (Figure 2.2). This is done by combining all the photon energies ( $E$ ) of the spectrum, relative to the count ratio for each photon energy of the spectrum, using Equations 1 and 2. Equation 1 combines all the counts with respect to each energy of the spectrum. The resultant effective energies (Figure 2.2) calculated using Equation 2 are similar to the ones reported by Yada and Onishi (2016) using the same method. The similarities in effective energies reflects similar X-ray energy spectra between the XCT systems.

Conversion of the spectrum into a single energy simplifies the linear attenuation coefficient calculations. In addition to this, it allows a direct comparison of

theoretically calculated linear attenuation coefficients with the experimental ones. This means that the calculated linear attenuation coefficients can be used to predict how minerals will correlate with grey values on radiographs or 2D image slices taken from 3D image volumes. Grey values are a direct representation of the average linear attenuation coefficients of minerals (Akça and Erzenoğlu, 2014; Olariño, 2011). Where samples are high density or larger volume, it can be difficult to calculate accurate linear attenuation coefficients since the X-ray beam is hardened as it passes through the sample (McCullough et al., 1974) causing the effective energy to be higher (Tsuchiyama et al., 2000). This will affect the expected discrimination between the mineralogical information based on the initially calculated linear attenuation coefficients. Therefore, in such a case, a stepwise protocol should be used to determine what is affecting the discrimination between the minerals.

$$Count_{Total} = Count_1(E_1) + Count_2(E_2) + \dots + Count_n(E_n) \dots \quad Eqn1$$

$$Effective\ energy\ (keV) = \frac{Count_1(E_1)}{Count_{Total}} \times E_1 + \frac{Count_2(E_2)}{Count_{Total}} \times E_2 + \dots + \frac{Count_n(E_n)}{Count_{Total}} \times E_n \dots \quad Eqn2$$

## CHAPTER 2: Attenuation Coefficients

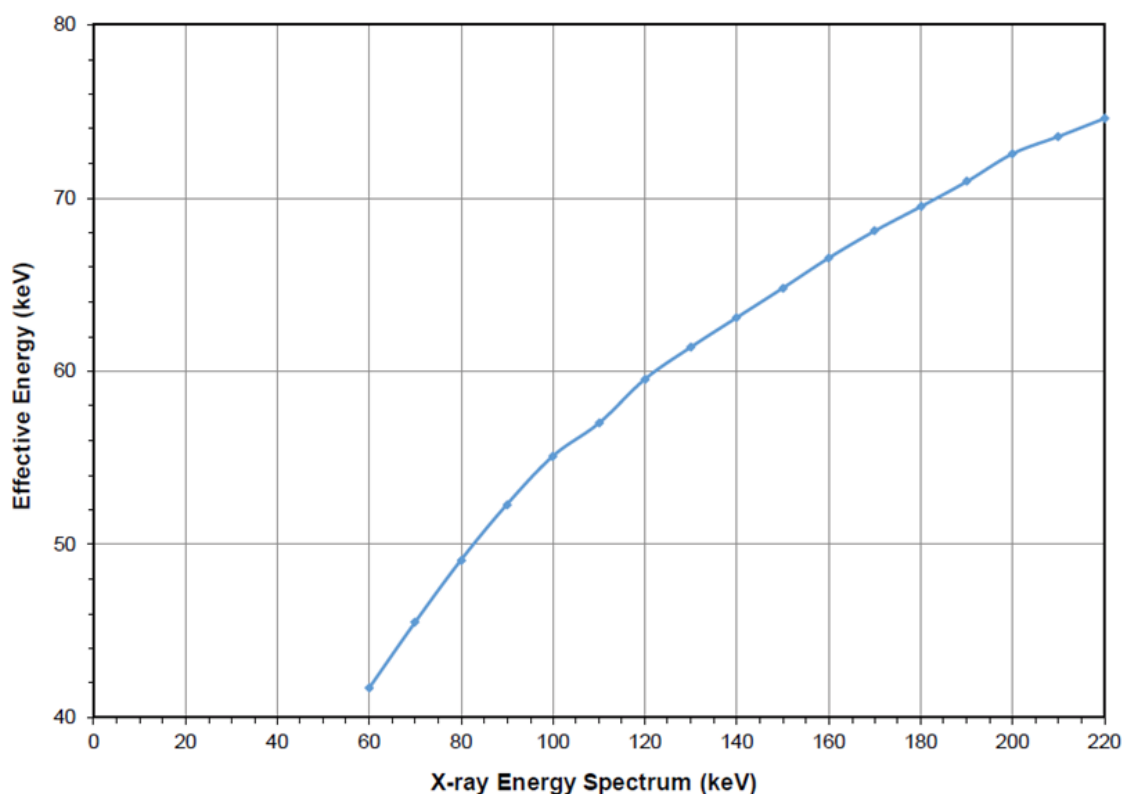


**Fig. 2.2.** Correlation between the effective X-ray energy and the X-ray energy spectrum of the tungsten target.

### 2.2. Development of the Attenuation Coefficient Databank

The mass attenuation coefficient data from NIST represents the mass attenuation coefficients for all elements at different X-ray energies [http://physics.nist.gov/PhysRefData/XrayMassCoef/table3.html]. In order to properly utilise the mass attenuation coefficient data for discrete X-ray energies or X-ray energies similar to the collected spectrums mentioned above, a set of linear and polynomial equations (equations 3-5) were fitted to represent the change of mass attenuation coefficient as the X-ray energy increases (Figure 2.3). Iron has been used as an example to illustrate the decreasing mass attenuation coefficient with increasing X-ray energy and the spike in mass attenuation coefficient at 7.112 keV is due to a K-edge absorption. These equations were fitted for all elements in the periodic table taking into consideration the behaviour of mass attenuation coefficients with respect to energy. Fitting different equations was done to minimise deviations between the expected mass attenuation coefficients with the calculated ones.

$$y = mx + c \quad \text{Eqn3}$$

$$y = ax^2 + bx + c \quad \text{Eqn4}$$

$$y = ax^5 + bx^4 + cx^3 + dx^2 + ex + f \quad \text{Eqn5}$$

The x and y-axis represent the X-ray energy and mass attenuation coefficient respectively. This method was repeated for all the elements including Li, B, C, O, Na, Mg, Al, Si, P, S, Cl, K, Ca, Ti, V, Cr, Mn, Fe, Co, Ni, Cu, Zn, As, Zr, Mo, Ag, Ba, Ta, W, Pb and Bi, which are more common in minerals. In cases where Equation 3 and 4 could not provide satisfactory mass attenuation coefficients, Equation 5 (high order polynomial) was used to minimize deviations between the mass attenuation coefficient calculated in this spreadsheet and that provided by NIST.

The mass attenuation coefficient for minerals,  $\mu/\rho$  (cm<sup>2</sup>/g), was calculated using Equation 6 where  $\omega_i$  is the weight fraction of *i*th element (Akça and Erzeneoilu, 2014; Olarinoye, 2011). The linear attenuation coefficient,  $\mu$  (cm<sup>-1</sup>), was then obtained by rearranging Equation 6 to give Equation 7.

$$\frac{\mu}{\rho} = \sum_i \left( \frac{\mu}{\rho} \right)_i \omega_i \quad \text{Eqn6}$$

$$\mu = \left[ \sum_i \left( \frac{\mu}{\rho} \right)_i \omega_i \right] \rho \quad \text{Eqn7}$$

### 2.3. Development of User Spreadsheet

The databank spreadsheet calculates the linear attenuation coefficient as an output using Equation 7 (Table 2.1). The spreadsheet is designed to be user-

## CHAPTER 2: Attenuation Coefficients

friendly with minimal inputs required to immediately calculate the linear attenuation coefficient for any mineral and can accommodate complex mineral compositions. Calculating the linear attenuation coefficient of different minerals requires a user to insert the actual number of elements (both cations and anions) present within a mineral (ie the exact mineral composition), the mineral density and the relevant effective energy under the appropriate columns (indicated in Table 2.1 which is a representation of the spreadsheet interface). The spreadsheet can calculate the linear attenuation coefficient of the same or different mineral at two different energies simultaneously.

This allows a direct comparison of the linear attenuation coefficient of minerals to better understand the impact of grey value variation on image slices in order to optimize mineralogical discrimination prior to scanning. The voltage is equivalent to the energy spectrum indicated in the column for the tungsten spectrum. The effective energy is converted from the tungsten spectrum and is utilized to calculate the linear attenuation coefficient as an output under the X-ray attenuation coefficient cell. It is important to mention that there is another spreadsheet that exist called the MuCalculator which can also calculate the linear attenuation coefficient for any mineral <https://utexas.app.box.com/v/MuCalc>. However, the spreadsheet calculates the linear attenuation coefficient at specific X-ray energies.

#### 2.4. Validation of Linear Attenuation Coefficients

To validate the ability of the excel spreadsheet to predict mineral discrimination using linear attenuation coefficients, thirteen minerals were scanned using a Micro-focus X-ray computed tomography system (Nikon XTH 225 ST) and their grey values compared. Prior to scanning the minerals were grouped as follows based on linear attenuation coefficient and mineral density: a) almandine, andradite and grossular; b) quartz, kaolinite, dolomite, calcite; c) fluorite, apatite; and d) goethite, chromite, magnetite and hematite. The density information for all the minerals was obtained from (<https://www.mindat.org/>). All the minerals were scanned at 70kV (45.5keV effective energy) using different filter materials as well as having no filter (Table 2.2). The set voltage on the target represents the collected energy spectrum with a maximum energy of 70keV. The samples were scanned at a 20 $\mu$ m resolution with 3000 projections and 4 seconds exposure time. The scanned data was reconstructed using CT Pro 3D software by applying various built-in beam hardening correction factors within the software. All the samples were analysed using VG Studio Max 3.2 software. The region growing tool was used to remove background information from all the minerals in order to deal only with the mineral grey values themselves. It was important to define the mineral

## CHAPTER 2: Attenuation Coefficients

**Table 2.1**

Excel spreadsheet template with inputs under number of atoms in the compound, density and voltage for each mineral. The calculated output is under X-ray attenuation coefficient.

Elements	Number of atoms in the compound	Density of the compound (g/cm <sup>3</sup> )	Effective energy (keV)	Elements	Number of atoms in the compound	Density of the compound (g/cm <sup>3</sup> )	Effective energy (keV)	Voltage kV	Tungsten spectrums	Effective energy (keV)
H		3.75	45.50	H		3.75	74.60	60	60	41.7
He				He				70	70	45.5
Li				Li				80	80	49.1
Be				Be				90	90	52.3
B				B				100	100	55.1
C				C				110	110	57.4
N				N				120	120	59.5
O	12			O	12			130	130	61.3
F				F				140	140	63.1
Ne		1.25E+00		Ne			7.06E-01	150	150	64.8
Na				Na				160	160	66.5
Mg	3			Mg	3			170	170	68.1
Al	2			Al	2			180	180	69.5
Si	3			Si	3			190	190	70.95
P				P				200	200	72.6
S				S				210	210	73.6
Cl				Cl				220	220	74.6

## CHAPTER 2: Attenuation Coefficients

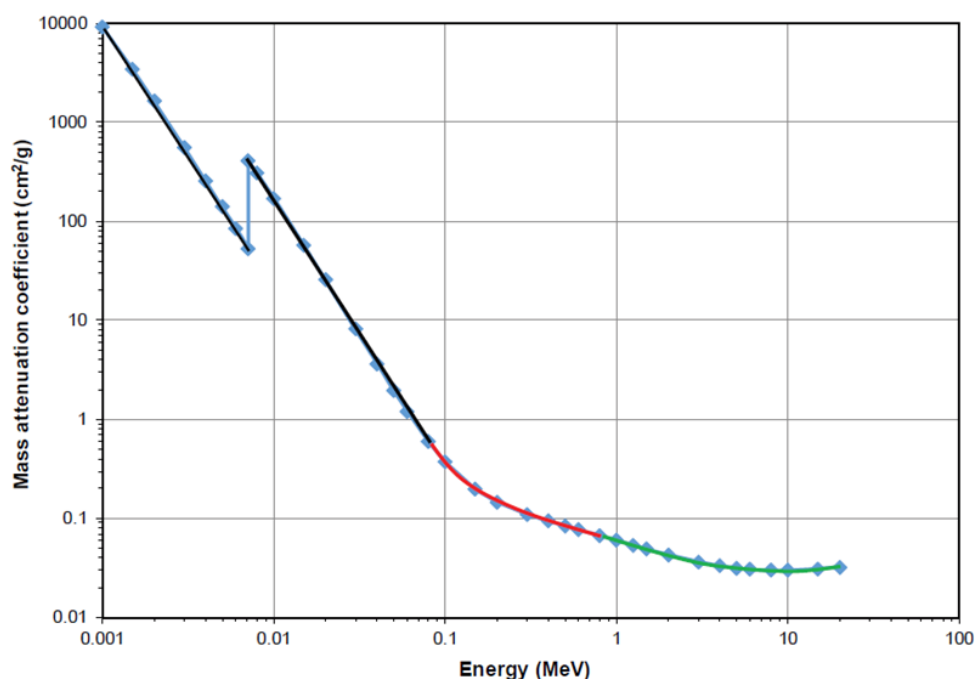


**Fig. 2.3.** The representation of iron mass attenuation coefficient by different equations (linear, second and fifth order polynomial). The black lines represent linear equations (equation 1) and the red and green curves represent the second and fifth order polynomial equations (equation 2 and 3).

grey value range because it was used to assign a false colour to the individual minerals in order to determine how grey values of different minerals overlap with each other. The mineral identities, compositions, as well as compositional homogeneity were confirmed using standardized scanning electron microscopy (SEM) and quantitative evaluation of materials by scanning electron microscopy (QEMSCAN). Individual minerals were prepared into polished sections and running using a FEI QEMSCAN 650F instrument on the field image analysis routine at the University of Cape Town. Measurements were run at 25 kV, 10nA using 100 micron pixel spacing. Then same sections were then used for SEM-EDS analysis conducted at the Electron Microscopy Unit of the Central Analytical Facility (Stellenbosch University, South Africa) using Zeiss EVO MA15VP Scanning Electron Microscope. The measurements were carried out in a nitrogen atmosphere at pressures from 65 to 96 Pa, voltages from 20 kV to 30 kV, working distance for EDS analyses of 8.5 mm and magnifications ranging between 1000x and 5000x. The

validation process also provided information about possible inclusions that may: a) affect expected discrimination between minerals; and b) provide a false assumption that a mineral can be discriminated from another mineral due to the presence of uniformly distributed inclusions that cannot be easily detected by the XCT scanning resolution.

### 3. Results

Here we present the results of this study in two parts. In the first part, we calculate linear attenuation coefficients for a variety of minerals of varying compositional complexity using the compiled spreadsheet. These values are compared to those that can be generated using the NIST database to assess the accuracy of the spreadsheet. Thereafter, mineral linear attenuation coefficients, calculated using the databank, are compared with the mineral grey values, generated using XCT, to evaluate the minimum difference in attenuation coefficient needed to be able to discriminate two minerals using XCT.

**Table 2.2.**

Scanning parameters to optimize discrimination between minerals.

Exposure time (sec)	No of projections	Voltage (kV)/ Effective energy (keV)	Filter material
4	3000	70/45.5	No filter
4	3000	70/45.5	0.25mm Cu
4	3000	70/45.5	1mm Al + 1mm Cu



## CHAPTER 2: Attenuation Coefficients

## CHAPTER 2: Attenuation Coefficients

**Table 2.3.**

Comparison of the NIST and spreadsheet attenuation coefficient for different types of minerals.

Mineral	Chemical formula	Density (g/cm <sup>3</sup> )	Energy (keV)	NIST Attenuation coefficient (cm <sup>-1</sup> )	Spreadsheet Attenuation coefficient (cm <sup>-1</sup> )	%Error	Energy (keV)	NIST Attenuation coefficient (cm <sup>-1</sup> )	Spreadsheet Attenuation coefficient (cm <sup>-1</sup> )	%Error
Acanthite	Ag <sub>2</sub> S	7.24	44.79	79.68	80.6	1.14	62.53	32.43	32.7	0.83
Almandine	Fe <sub>3</sub> Al <sub>2</sub> Si <sub>3</sub> O <sub>12</sub>	4.32	44.79	4.77	4.55	4.56	62.53	2.21	2.19	0.53
Andradite	Ca <sub>3</sub> Fe <sup>3+</sup> <sub>2</sub> Si <sub>3</sub> O <sub>12</sub>	3.86	44.79	4.09	3.91	4.44	62.53	1.91	1.9	0.35
Ankerite	CaFe(CO <sub>3</sub> ) <sub>2</sub>	3.2	44.79	3.33	3.19	4.2	62.53	1.56	1.56	0.00
Apatite	Ca <sub>5</sub> (PO <sub>4</sub> ) <sub>3</sub> OH	3.19	44.79	2.36	2.28	3.39	62.53	1.19	1.19	0.00
Arsenopyrite	FeAsS	6.18	44.79	20.23	20.4	0.83	62.53	8.26	8.51	2.94
Barite	BaSO <sub>4</sub>	4.48	44.79	48.67	48.1	1.17	62.53	20.31	21	3.29
Borax	Na <sub>2</sub> B <sub>4</sub> O <sub>5</sub> (OH) <sub>4</sub> ·8H <sub>2</sub> O	1.7	44.79	0.42	0.41	3.02	62.53	0.34	0.33	2.94
Calcite	CaCO <sub>3</sub>	2.71	44.79	1.8	1.73	4.09	62.53	0.94	0.94	0.54
Carnotite	K <sub>2</sub> (UO <sub>2</sub> ) <sub>2</sub> (VO <sub>4</sub> ) <sub>2</sub> ·3H <sub>2</sub> O	4.91	44.79	38.9	40.6	4.19	62.53	17.83	17.2	3.53
Chalcocite	Cu <sub>2</sub> S	5.6	44.79	16.48	17.2	4.19	62.53	6.72	6.49	3.42
Chalcopyrite	CuFeS <sub>2</sub>	4.2	44.79	9.48	9.58	1.04	62.53	3.95	3.89	1.52
Chlorite	(Mg) <sub>5</sub> Al <sub>2</sub> Si <sub>3</sub> O <sub>10</sub> (OH) <sub>8</sub>	3.2	44.79	1.09	1.04	4.44	62.53	0.73	0.72	1.30
Chromite	FeCr <sub>2</sub> O <sub>4</sub>	4.79	44.79	7.93	8.03	1.21	62.53	3.42	3.4	0.55
Corundum	Al <sub>2</sub> O <sub>3</sub>	4.02	44.79	1.41	1.34	4.96	62.53	0.92	0.91	1.09
Dolomite	CaMg(CO <sub>3</sub> ) <sub>2</sub>	2.85	44.79	1.39	1.33	4.32	62.53	0.8	0.8	0.00
Fluorite	CaF <sub>2</sub>	3.13	44.79	2.5	2.41	3.76	62.53	1.23	1.23	0.38
Gibbsite	Al(OH) <sub>3</sub>	2.34	44.79	0.74	0.7	4.89	62.53	0.52	0.51	2.16
Goethite	FeO(OH)	4.28	44.79	7.34	7.01	4.49	62.53	3.17	3.16	0.22
Grossular	Ca <sub>3</sub> Al <sub>2</sub> Si <sub>3</sub> O <sub>12</sub>	3.65	44.79	2.22	2.12	4.45	62.53	1.19	1.18	0.77
Hematite	Fe <sub>2</sub> O <sub>3</sub>	5.26	44.79	9.89	9.45	4.48	62.53	4.21	4.2	0.16
Ilmenite	FeTiO <sub>3</sub>	4.76	44.79	7.26	6.95	4.34	62.53	3.17	3.13	1.05
Kaolinite	Al <sub>2</sub> Si <sub>2</sub> O <sub>5</sub> (OH) <sub>4</sub>	2.6	44.79	0.91	0.87	4.9	62.53	0.6	0.59	1.95
K-feldspar	KAlSi <sub>3</sub> O <sub>8</sub>	2.56	44.79	1.22	1.16	4.65	62.53	0.71	0.71	0.00
Lepidolite	KLi <sub>2</sub> AlSi <sub>4</sub> O <sub>10</sub> (OH) <sub>2</sub>	2.83	44.79	1.21	1.16	4.45	62.53	0.74	0.73	1.35
Magnetite	Fe <sub>3</sub> O <sub>4</sub>	5.18	44.79	10.03	9.58	4.48	62.53	4.25	4.25	0.14
Molybdenite	MoS <sub>2</sub>	5.00	44.79	29.65	30.5	2.79	62.53	12.03	12.5	3.76
Olivine	Fe <sub>2</sub> SiO <sub>4</sub>	3.32	44.79	5.2	4.97	4.42	62.53	2.27	2.26	0.44
Pecoraite	Ni <sub>3</sub> S <sub>2</sub> O <sub>5</sub> (OH) <sub>4</sub>	3.47	44.79	6.65	6.92	3.87	62.53	2.57	2.7	4.81
Pyrite	FeS <sub>2</sub>	5.01	44.79	8.02	7.81	2.52	62.53	3.48	3.5	0.63
Pyrope	Mg <sub>3</sub> Al <sub>2</sub> Si <sub>3</sub> O <sub>12</sub>	3.75	44.79	1.34	1.28	4.51	62.53	0.87	0.86	1.30
Quartz	SiO <sub>2</sub>	2.65	44.79	1.01	0.96	4.95	62.53	0.64	0.63	1.68
Rynersonite	CaTa <sub>2</sub> O <sub>6</sub>	6.39	44.79	35.64	36	0.99	62.53	15.13	15.2	0.46
Safflorite	CoAs <sub>2</sub>	7.47	44.79	32.11	31.1	3.13	62.53	12.91	13.4	3.66
Siderite	FeCO <sub>3</sub>	3.96	44.79	5.41	5.17	4.47	62.53	2.41	2.404	0.35
Spessartine	Mn <sub>3</sub> Al <sub>2</sub> Si <sub>3</sub> O <sub>12</sub>	4.29	44.79	4.22	4.33	2.51	62.53	2	1.98	0.94
Sphalerite	ZnS	4.1	44.79	11.68	11.9	1.82	62.53	4.78	4.8	0.42
Talc	Mg <sub>3</sub> Si <sub>4</sub> O <sub>10</sub> (OH) <sub>2</sub>	2.75	44.79	0.99	0.94	4.85	62.53	0.64	0.64	0.00
Uvarovite	Ca <sub>3</sub> Cr <sub>2</sub> Si <sub>3</sub> O <sub>12</sub>	3.85	44.79	3.55	3.55	0.15	62.53	1.7	1.69	0.69
Wolframite	FeWO <sub>4</sub>	7.30	44.79	38.12	38.7	1.5	62.53	16.16	16.3	0.86
Zircon	ZrSiO <sub>4</sub>	4.71	44.79	20.06	21.1	4.94	62.53	8.26	8.4	1.67

## CHAPTER 2: Attenuation Coefficients

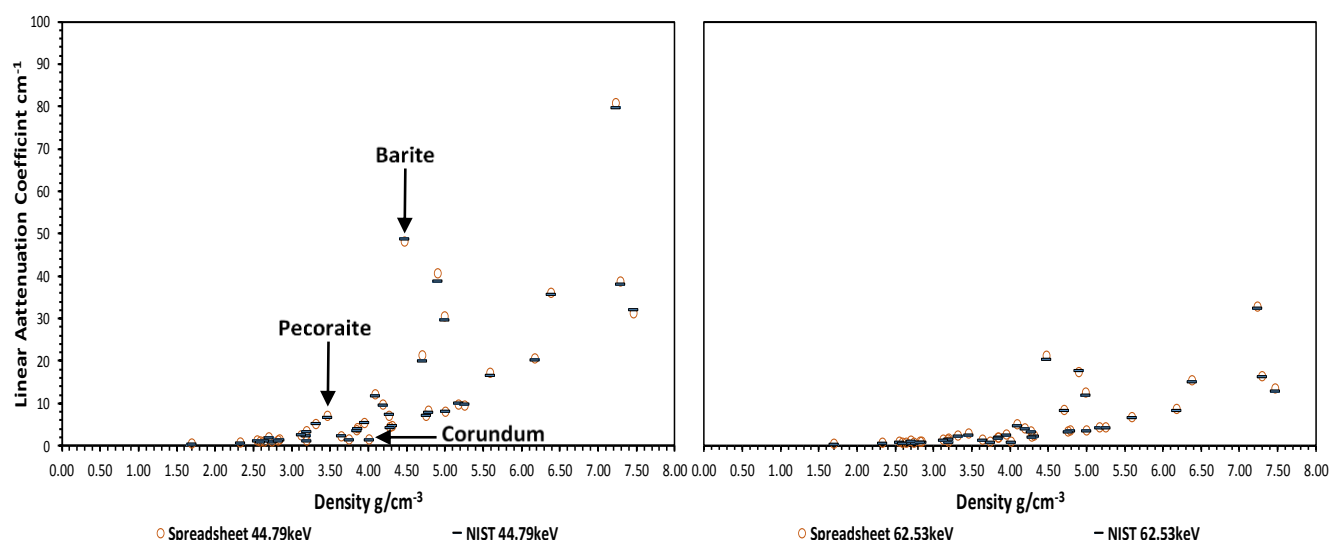


**Fig. 2.4.** Variation of linear attenuation coefficients for different mineral densities calculated with the developed spreadsheet and NIST at: A) 44.79keV and B) 62.53keV X-ray energy

### 3.1. Calculated Linear Attenuation Coefficients

Table 2.3 lists a wide range of minerals (40 in total) with different densities and chemical compositions. The 40 minerals were picked to evaluate different mineral compositional complexity in terms of both the range of elements present in the mineral as well as the mineral structure. It includes minerals regarded as ore minerals (e.g. chalcopyrite, hematite and sphalerite), clay minerals (e.g. kaolinite), carbonates (e.g. calcite and dolomite) and end-member varieties of the same mineral (e.g. pyrope, almandine, grossular, andradite and spessartine garnets). The maximum % error difference between the calculated linear attenuation coefficients using the spreadsheet and those given by the NIST database is 4.96% at 44.79keV and 4.81% at 62.53keV. At 44.79keV nine minerals have a % error less than 2%, whilst at 62.53keV, 22 minerals have a % error less than 2% (Table 2.3). The calculated mineral linear attenuation coefficients increase with increasing density but the trend is not linear and the mineral attenuation is lower at 62.53keV as expected (Fig. 2.4). Interrogation of the data indicates that it is not possible to predict the linear attenuation coefficient based on mineral density alone. Comparison of sphalerite and corundum for example, shows similar densities (4.1 g/cm<sup>3</sup> and 4.02 g/cm<sup>3</sup> respectively) but large differences in linear attenuation coefficient (11.9 cm<sup>-1</sup> and 1.34 cm<sup>-1</sup> respectively). Because the minerals have similar densities, the logical assumption would be that these minerals cannot be differentiated using XCT, which is not true, based on the difference in their linear attenuation coefficients. In contrast, dolomite and corundum have similar attenuation coefficients (1.33 cm<sup>-1</sup> and 1.34 cm<sup>-1</sup> respectively) suggesting they cannot be differentiated using XCT, but these two minerals have significant differences in density (2.85

g/cm<sup>3</sup> and 4.02 g/cm<sup>3</sup> respectively). In this case, the difference in density would suggest these minerals can be differentiated using XCT, which is not true, based on the linear attenuation coefficient information. The above examples illustrate the complexity of trying to evaluate whether XCT is useful for different mineral pairs, although the likelihood of dolomite and corundum naturally occurring in the same rock is low. A more likely combination is dolomite and calcite. In this case, the density of calcite is 2.71 g/cm<sup>3</sup> in comparison to the 2.85 g/cm<sup>3</sup> of dolomite and the linear attenuation of calcite is 1.73 cm<sup>-1</sup> in comparison to the 1.33 cm<sup>-1</sup> of dolomite. In this example, it is unclear if these differences are large enough to be able to differentiate these minerals using XCT. Therefore, the second part of the results presented here, uses the attenuation spreadsheet to evaluate the minimum difference in linear attenuation coefficient needed to differentiate two minerals.

### 3.2. Minimum Attenuation Coefficient Difference to Determine Discrimination

XCT, SEM-EDS and QEMSCAN analysis was undertaken on 31 minerals from Table 2.3 but of these only 13 provided data that could be properly interrogated for grey level variation (Fig. 2.5 and Table 2.4). Table 2.5 shows comparison of different mineral pairs from these 13 minerals. The pairs are based on minerals occurring in the same QEMSCAN polished mount so that the grey values are comparable and reflect the linear attenuation coefficient (Fig. 2.5). Minerals with a linear attenuation coefficient less than 2cm<sup>-1</sup> did not require the utilisation of any filters to optimize grey value variation. This is demonstrated by quartz, kaolinite, dolomite and calcite (Fig.2.5 d,e,f,g) respectively. However, minerals with a linear attenuation coefficient more than 3cm<sup>-1</sup> required

## CHAPTER 2: Attenuation Coefficients

**Table 2.4.**

Grey value variation of different minerals with their corresponding density [<https://www.mindat.org/>] and linear attenuation coefficients.

Mineral	Chemical formula	Density g/cm <sup>3</sup>	Attenuation coefficient cm <sup>-1</sup>	Mean Grey value
Almandine	Fe <sub>3</sub> Al <sub>2</sub> Si <sub>3</sub> O <sub>12</sub>	4.32	4.36	28084.49
Andradite	Ca <sub>3</sub> Fe <sup>3+</sup> <sub>2</sub> Si <sub>3</sub> O <sub>12</sub>	3.86	3.74	34569.42
Grossular	Ca <sub>3</sub> Al <sub>2</sub> Si <sub>3</sub> O <sub>12</sub>	3.65	2.05	22971.93
Quartz	SiO <sub>2</sub>	2.65	0.93	10540.60
Kaolinite	Al <sub>2</sub> Si <sub>2</sub> O <sub>5</sub> (OH) <sub>4</sub>	2.60	0.85	11014.87
Dolomite	CaMg(CO <sub>3</sub> ) <sub>2</sub>	2.85	1.29	15047.84
Calcite	CaCO <sub>3</sub>	2.71	1.66	18285.01
Fluorite	CaF <sub>2</sub>	3.13	2.31	23955.95
Apatite	Ca <sub>5</sub> (PO <sub>4</sub> ) <sub>3</sub> OH	3.15	2.15	21737.91
Goethite	FeO(OH)	4.28	6.70	36097.60
Chromite	FeCr <sub>2</sub> O <sub>4</sub>	4.79	7.70	38856.87
Magnetite	Fe <sub>3</sub> O <sub>4</sub>	5.18	9.15	54895.83
Hematite	Fe <sub>2</sub> O <sub>3</sub>	5.26	9.02	57344.77

application of a filter in order to optimise X-ray penetration and minimise beam hardening. In the case of magnetite and hematite (Fig. 2.5 l,m), the highest density minerals examined, a combination of filter materials and high beam hardening correction factor was used to minimise the impact of beam hardening.

Evaluating the required linear attenuation coefficient difference to determine discrimination between minerals is not trivial. This is due to grey value overlap between minerals which cannot be avoided in most cases, when using XCT. Partly this is because most naturally occurring minerals have inclusions of other minerals in them to some extent. This is well demonstrated by the quartz and kaolinite samples used here. The calculated linear attenuation coefficient difference between these minerals is 9.42%. However, the measured grey value difference between these two minerals was determined to be 4.31%, resulting in only partial discrimination (Fig. 2.5 d,e.). The grey value overlap is due to the presence of small inclusions of quartz and k-feldspar in the kaolinite (Fig. 2.6). A similar situation exists between goethite and chromite (Fig. 2.5 j,k) where the linear attenuation coefficient difference is higher (12.99%) but the grey value difference is lower (7.1%), resulting in only partial discrimination of the two minerals. In this case, the grey value overlap is due to different Fe-concentrations within the goethite matrix. In some cases, the presence of mineral inclusion does not affect the mineral discrimination but still affects the mean grey value that is supposed to represent the true linear attenuation coefficient. This is a case with almandine, which has a higher linear attenuation coefficient than andradite, but has a lower mean grey value (Table 2.4 and Figure 2.6) due to the presence of uniformly distributed pyrope and minor grossular as

inclusions. Despite the presence of these mineral inclusions in almandine, almandine

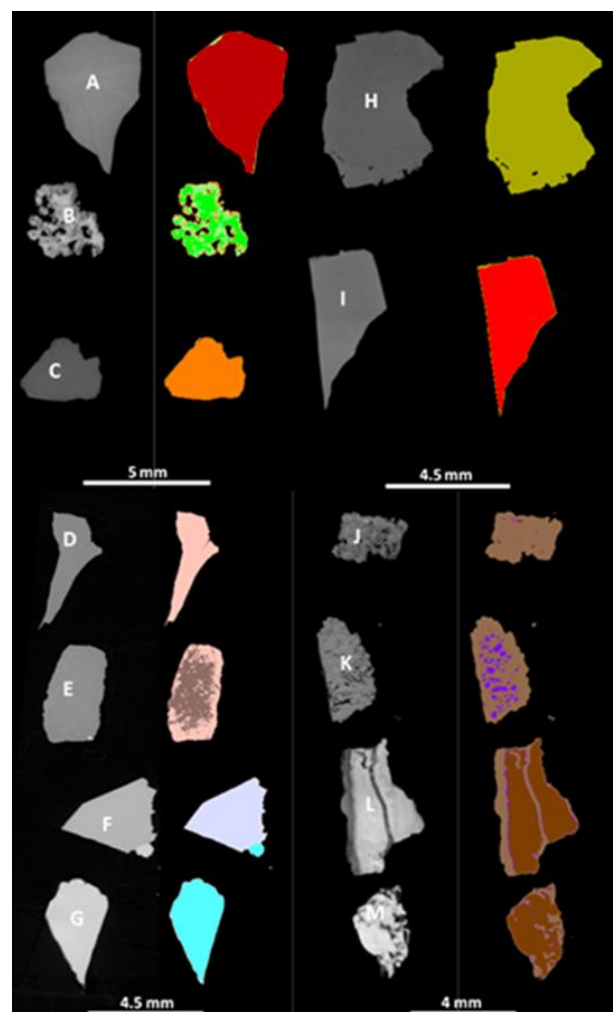


**Fig. 2.5.** Grey value variation of different minerals with their corresponding false colour to illustrate discrimination between minerals at 45.5keV effective energy: A)

## CHAPTER 2: Attenuation Coefficients

almandine, B) andradite, C) grossular, D) quartz, E) kaolinite, F) dolomite, G) calcite, H) apatite, I) fluorite, J)

goethite, K) chromite, L) magnetite and M) hematite.

**Table 2.5.**

Mineral discrimination using linear attenuation coefficient difference in conjunction with grey value and density difference. BH = beam hardening

Mineral comparison	Filter material/BH correction factor	% Grey value difference	% Attenuation coefficient difference	% Density difference	Discrimination
Almandine vs Andradite	<b>0.25mm Cu/2</b>	18.76	14.22	10.65	yes
Almandine vs Grossular		18.20	52.98	15.51	yes
Grossular vs Andradite		33.55	45.19	5.44	yes
Quartz vs Kaolinite	<b>No Filter/2</b>	4.31	9.42	1.89	Partial
Quartz vs Dolomite		29.95	27.60	7.02	yes
Quartz vs Calcite		42.35	43.73	2.21	yes
Kaolinite vs Dolomite		26.80	34.42	8.77	yes
Kaolinite vs Calcite		39.76	49.04	4.06	yes
Dolomite vs Calcite		17.70	22.29	4.91	yes
Fluorite vs Apatite	<b>0.25mm Cu/1</b>	9.26	6.06	0.63	Yes
Goethite vs Chromite	<b>0.25mm Cu/2</b>	7.10	12.99	10.65	Partial
Goethite vs Magnetite	<b>1mm Cu + 1mm Al/3</b>	34.24	26.78	17.37	yes
Goethite vs Hematite		37.05	25.72	18.63	yes
Chromite vs Magnetite		29.22	15.85	7.53	yes
Chromite vs Hematite		32.24	14.63	8.94	yes
Magnetite vs Hematite		4.27	1.42	1.52	no

was clearly discriminated from andradite with a grey value difference of 18.76% and a linear attenuation coefficient difference of 14.22% (Table 2.5 and Figure 2.5). Similarly, apatite and fluorite (Fig. 2.5 h,i) are completely discriminated from one another in terms of their grey value levels (9.26%) but have a lower linear attenuation coefficient difference (6.06%). This is attributed to the fact that there are no inclusions within the minerals. This shows that a minimum linear attenuation coefficient difference of 6% is enough to discriminate between minerals. Minerals with linear attenuation coefficient difference less than this may be difficult to discriminate. Hematite and magnetite have a linear attenuation coefficient difference of 1.42% with a density difference of 1.54%, resulting in a grey value difference of 4.27%. Therefore, hematite and magnetite cannot be discriminated from each other according to Fig. 2.5. Thus, it would seem that minerals with a linear attenuation coefficient difference of less than ~4.3% cannot be differentiated using XCT, whereas minerals with a linear attenuation coefficient difference above ~6% can be differentiated. However, this assumes that the minerals are pure and free of inclusions. If the minerals are not compositionally pure then the presences of inclusions complicate

discrimination as in the case of the quartz and kaolinite samples used here.

#### 4. Discussion

The linear attenuation coefficient database developed above is a practical, user friendly tool for calculating linear attenuation coefficients. It is also very flexible in that it allows the user to calculate attenuation coefficients at any effective X-ray energy between 41.7keV and 74.6 keV and this can be done offline. Comparison of the spreadsheet database with that of the NIST online calculation tool indicates that the difference between the two is less than 5%. The spreadsheet highlights the importance of knowing the exact mineral composition (in terms of specific cation and anion numbers) and density in order to predict which minerals can be discriminated and which can't. In the following discussion, several examples of where this spreadsheet can be used to better set up XCT experiments are demonstrated.

##### 4.1. Mineral Composition and Linear Attenuation Coefficient

For minerals with no solid solution, such as quartz, the calculation of the linear attenuation coefficient is straight forward as the chemical formula is fixed. In the

## CHAPTER 2: Attenuation Coefficients

case of quartz, which is  $\text{SiO}_2$ , the linear attenuation coefficient is  $0.93 \text{ cm}^{-1}$  at  $45.5 \text{ keV}$ . However, for

minerals with solid solution

**Table 2.6.**

Summary of common minerals in iron ores, alongside their formulae and density <https://www.mindat.org/>.

Iron mineral	Formula	Density $\text{g/cm}^3$	Gangue mineral	Formula	Density $\text{g/cm}^3$
Hematite	$\text{Fe}_2\text{O}_3$	5.26	Quartz	$\text{SiO}_2$	2.65
Magnetite	$\text{Fe}_3\text{O}_4$	5.18	Kaolinite	$\text{Al}_2\text{Si}_2\text{O}_5(\text{OH})_4$	2.60
Goethite	$\text{FeO}(\text{OH})$	4.28	Fluorite	$\text{CaF}_2$	3.13
Siderite	$\text{FeCO}_3$	3.96	Barite	$\text{BaSO}_4$	4.48
Chlorite	$(\text{Mg})_5\text{Al}_2\text{Si}_3\text{O}_{10}(\text{OH})_8$	3.20	Apatite	$\text{Ca}_5(\text{PO}_4)_3\text{OH}$	3.19
Pyrite	$\text{FeS}_2$	5.01	Gibbsite	$\text{Al}(\text{OH})_3$	2.34
Ilmenite	$\text{FeTiO}_3$	4.76	Ankerite	$\text{CaFe}(\text{CO}_3)_2$	3.20

substitution, it is necessary to know the exact composition of the mineral in the sample being analyzed. Garnet which is a common mineral in a variety of rocks elegantly illustrates this. The generic formula for garnet is  $\text{X}_3\text{Y}_2(\text{SiO}_4)_3$  with X representing Mg, Fe, Mn or Ca and Y representing Al or Cr (Deer et al., 1992). The example shown in Table 2.1 is of a pyrope garnet, with the composition  $\text{Mg}_3\text{Al}_2\text{Si}_3\text{O}_{12}$  and density  $3.75 \text{ g/cm}^3$  and has the linear attenuation coefficient of  $1.25 \text{ cm}^{-1}$  at  $45.5 \text{ keV}$  effective energy. This is distinct from garnet with different compositions such as almandine  $\text{Fe}_3\text{Al}_2\text{Si}_3\text{O}_{12}$  ( $4.32 \text{ g/cm}^3$ ,  $4.36 \text{ cm}^{-1}$ ), spessartine  $\text{Mn}_3\text{Al}_2\text{Si}_3\text{O}_{12}$  ( $4.29 \text{ g/cm}^3$ ,  $4.16 \text{ cm}^{-1}$ ), andradite  $\text{Ca}_3\text{Fe}^{3+}_2\text{Si}_3\text{O}_{12}$  ( $3.86 \text{ g/cm}^3$ ,  $3.74 \text{ cm}^{-1}$ ), uvarovite  $\text{Ca}_3\text{Cr}_2\text{Si}_3\text{O}_{12}$  ( $3.85 \text{ g/cm}^3$ ,  $3.41 \text{ cm}^{-1}$ ), and grossular  $\text{Ca}_3\text{Al}_2\text{Si}_3\text{O}_{12}$  ( $3.65 \text{ g/cm}^3$ ,  $2.05 \text{ cm}^{-1}$ ) calculated at the same X-ray energy. The difference in the linear attenuation coefficients is a result of differences in the densities and chemical compositions of these minerals even though the structural formula remains constant and the physical properties of all the garnet varieties remains very similar. As a consequence of the differences in linear attenuation coefficient, these minerals will appear differently on a 2D image slice except for almandine and spessartine due to a lower attenuation coefficient difference of 4.6%.

The example given above assumes that garnet exists as one of the end-member compositions, but this is not usually the case, with garnet exhibiting solid solution substitution within both the X and Y cation sites. What this means in practice is that garnet in any given rock will have a linear attenuation coefficient of between  $4.36 \text{ cm}^{-1}$  and  $1.25 \text{ cm}^{-1}$  at  $45.5 \text{ keV}$  depending in its exact composition. For example, a garnet that is dominantly Fe-rich but also containing appreciable amounts of Mg as well as minor amounts of Mn and Ca in the cation proportions  $\text{Fe}_{2.1}\text{Mg}_{0.7}\text{Mn}_{0.15}\text{Ca}_{0.05}\text{Al}_2\text{Si}_3\text{O}_{12}$  would have an approximate composite density of  $4.16 \text{ g/cm}^3$  and a

linear attenuation coefficient of  $3.60 \text{ cm}^{-1}$  at  $45.5 \text{ keV}$ . This is significantly different from the linear attenuation coefficient values for either end-member almandine or pyrope. Assuming a linear attenuation coefficient of either of these end-members



## CHAPTER 2: Attenuation Coefficients

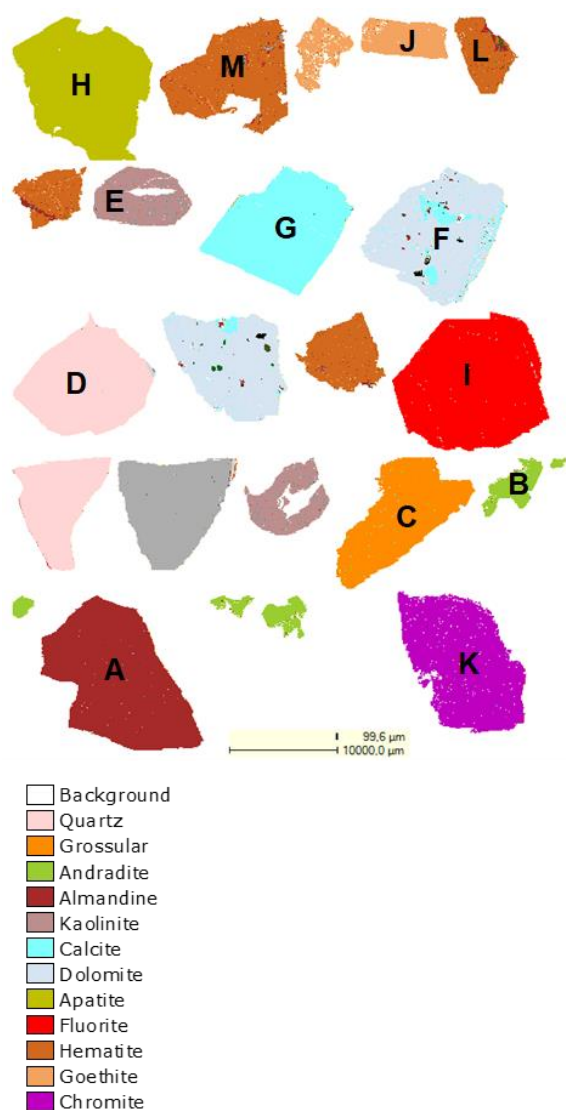


**Fig. 2.6.** Mineral classification using QEMSCAN in order to understand the discrimination between the minerals: A) almandine, B) andradite, C) grossular, D) quartz, E) Kaolinite, F) dolomite, G) calcite, H) apatite, I) fluorite, J) goethite, K) chromite, L) magnetite and M) hematite.

would result in significant error associated with the differentiation of this garnet composition from other minerals with linear attenuation coefficients in this range at 45.5keV. Similarly, using the density of one garnet composition, when in fact a different composition is present, will also result in the calculation of an incorrect linear attenuation coefficient.

#### 4.2. Mineral Density and Attenuation

The linear attenuation coefficient spreadsheet can also be used to illustrate the importance of upfront mineral density and compositional information when differentiating minerals using XCT. To evaluate this issue, iron ore is considered where iron ore mineralisation involves both iron ore minerals themselves (hematite, magnetite and goethite) as well as commonly associated gangue minerals may be present (quartz, kaolinite, gibbsite, chlorite, siderite,

ankerite, fluorite, barite and apatite). The theoretically calculated linear attenuation coefficients for these minerals (Table 2.6) were compared in order to evaluate the impact of different densities on the attenuation coefficient. This is well illustrated by barite ( $\text{BaSO}_4$ ), which has a lower density ( $4.48 \text{ g/cm}^3$ ) than hematite and magnetite ( $5.26$  and  $5.18 \text{ g/cm}^3$ ). These minerals have a minimum density difference 14.83% which suggest that barite should appear darker or with lower grey values than hematite and magnetite. But this is not the case because barite has a higher linear attenuation coefficient of  $46.1 \text{ cm}^{-1}$  at 45.5keV effective X-ray energy which would make it to appear brighter. In contrast, magnetite has a linear attenuation coefficient of  $9.15 \text{ cm}^{-1}$  while hematite is  $9.02 \text{ cm}^{-1}$ . The linear attenuation coefficients of hematite and magnetite are similar because their densities and chemical composition are similar, Table 2.6. In addition to this the majority of the minerals with a density difference  $< 5\%$  presented in Table 2.5 were partially and full distinguishable from each other except for hematite and magnetite. This further emphasizes the need to use linear attenuation coefficient information to predict if minerals can be discriminated or not as compared to using the density information alone.

#### 4.3. Influence of Mineral Composition vs Density on Attenuation Coefficient

Linear attenuation coefficients are much more strongly impacted by mineral composition than they are by density. This would suggest that it is much more important to obtain an accurate composition in order to optimize the discrimination between the minerals than it is to obtain an accurate density. This is illustrated using the example of olivine, which has a general structural formula of  $(\text{Mg,Fe})_2\text{SiO}_4$ , and an average density of  $3.3\text{g/cm}^3$ . Olivine of this composition and density, has a linear attenuation coefficient of  $4.20 \text{ cm}^{-1}$  at an arbitrary effective energy of 41.7keV, which is distinct from olivine of composition  $\text{Mg}_{1.6}\text{Fe}_{0.4}\text{SiO}_4$  with an attenuation coefficient of  $2.6 \text{ cm}^{-1}$  at the same energy and density. Swapping the ratio of magnesium and iron (ie.  $\text{Mg}_{0.4}\text{Fe}_{1.6}\text{SiO}_4$ ) results in an attenuation coefficient of  $5.49 \text{ cm}^{-1}$ , yielding a attenuation coefficient difference of 52.64% from the  $\text{Mg}_{1.6}\text{Fe}_{0.4}\text{SiO}_4$  composition when the same density is used for the calculations. When the same scenario is considered for  $\text{Mg}_{0.4}\text{Fe}_{1.6}\text{SiO}_4$  with a density reduction of 52.64% to  $1.74\text{g/cm}^3$  from its average density of  $3.3\text{g/cm}^3$ , its attenuation coefficient is  $2.9 \text{ cm}^{-1}$  which is 35.41% less than when the density is  $3.3\text{g/cm}^3$ . This means that a 52.64% reduction in density only resulted in a 32.42% reduction in attenuation coefficient for the same composition. Similarly, andradite and uvarovite garnets have almost identical densities ( $3.86$  vs  $3.85 \text{ g/cm}^3$ ) but linear attenuation coefficients of  $4.88$  and  $4.31 \text{ cm}^{-1}$  with a percentage attenuation coefficient difference of 11.68% at 41.7keV. Using density information alone would suggest that these two minerals cannot be discriminated even though their

## CHAPTER 2: Attenuation Coefficients

linear attenuation coefficients suggest that they can be. Thus, a change in composition has more effect on the attenuation coefficient than a change in density and hence knowing the exact composition of the minerals to be interrogated with XCT is critical to evaluate whether XCT is an appropriate tool to use.

## 5. Conclusions

Theoretically calculated linear attenuation coefficients form an important basis for planning XCT scans with optimal image contrast. These attenuation coefficients can be utilised to optimise the X-ray scanning energy to discriminate minerals according to exact mineral compositions as well as density for proper quantification. The data bank presented here is designed not only to be user friendly and compare attenuation coefficient information of two different minerals at the same time but also to be easily available. The discrimination between minerals with an attenuation coefficient difference of less than 6% will be challenging. This will depend on the complexity of the minerals especially if they have inclusions as observed between quartz and kaolinite with grey values difference of 4.31% even though their attenuation coefficient difference is > 9%. Optimal discrimination using attenuation coefficients depends more on the composition but also on scanning parameters including appropriate filter material being. Different minerals respond differently on the type of filter material being used, especially those with a density greater than 3 g/cm<sup>3</sup>. Minerals with a density less than 3 g/cm<sup>3</sup> might not require any application of filter materials in order to optimize discrimination. However, this will depend on the sample size and complexity of the sample being scanned (mineral inclusion). This means that minerals of interest should be well defined and understood prior to scanning so that the limitations associated with discriminating minerals using linear attenuation coefficients can be evaluated before XCT scanning. This will allow effective utilization or application of the XCT technique to the geological samples. Most importantly understanding the limitations of XCT will lead to further refinements of the XCT technique that may in the future overcome these limitations.

## 6. Acknowledgments

The authors would like to thank Necsa (Nuclear Energy Corporation of South Africa) and the management team for funding and access to the Microfocus system in the MIXRAD Lab, which is a DST-NRF (Department of Science and Technology – National Research Funding) funded facility through the NEP-RISP (National Equipment Programme – Research Infrastructure Support Programmes) program. The authors would also like to thank Andrew Watson for his contribution on compiling the diagrams and Madelaine Frazenburg for her SEM-EDS analysis.

The authors would like to acknowledge Gaynor Yorath and the UCT QEMSCAN team for assistance with QEMSCAN analysis. The project is supported through SAMMRI (South African Minerals to Metals Research Institute), grant number: S1511. This work is based on the research supported in part by the National Research Foundation of South Africa (Grant Numbers 86054, 99005). Any opinions, findings and conclusions or recommendations expressed in any publication generated by the NRF supported research is that of the author(s), and that the NRF accepts no liability whatsoever in this regard.

## 7. References

- Akça, B., Erzeneoğlu, S.Z., 2014. The mass attenuation coefficients, electronic, atomic, and molecular cross sections, effective atomic numbers, and electron densities for compounds of some biomedically important elements at 59.5 keV. *Sci. Technol. Nucl. Install.* 2014, 1–9.  
<https://doi.org/10.1155/2014/901465>
- Ashi, J., 1997. Computed Tomography Scan Image Analysis of Sediments, in: Shipley, T.H., Ogawa, Y., Blum, P., Bahr, J.M. (Eds.), *Proceedings of the Ocean Drilling Program, Scientific Results*. pp. 151–159.
- Bam, L.C., Miller, J.A., Becker, M., Beer, F.C. De, Basson, I., 2016. X-ray Computed Tomography – Determination of Rapid Scanning Parameters for Geometallurgical Analysis of Iron Ore, in: *Proceedings of the Third AusIMM International Geometallurgy Conference*. Perth, pp. 209–219.
- Cnudde, V., Masschaele, B., Dierick, M., Vlassenbroeck, J., Hoorebeke, L. Van, Jacobs, P., 2006. Recent progress in X-ray CT as a geosciences tool. *Appl. Geochemistry* 21, 826–832.  
<https://doi.org/10.1016/j.apgeochem.2006.02.010>
- Deer, W.A., Howie, R.A., Zussman, J., 1992. *An introduction to the rock-forming minerals*, second. ed. Pearson Prentice-Hall.
- Evans, C.L., Wightman, E.M., Yuan, X., 2015. Quantifying mineral grain size distributions for process modelling using X-ray micro-tomography. *Miner. Eng.* 82, 78–83.  
<https://doi.org/10.1016/j.mineng.2015.03.026>
- Ghorbani, Y., Becker, M., Petersen, J., Morar, S.H., Mainza, A., Franzidis, J.-P., 2011. Use of X-ray computed tomography to investigate crack distribution and mineral dissemination in sphalerite ore particles. *Miner. Eng.* 24, 1249–1257.  
<https://doi.org/10.1016/J.MINENG.2011.04.008>
- Hamdani, A.H., 2015. X-Ray Computed Tomography Analysis of Sajau Coal, Berau Basin, Indonesia: 3D Imaging of Cleat and Microcleat Characteristics. *Int. J. Geophys.* 2015.
- Jardine, M.A., Miller, J.A., Becker, M., 2018. Coupled X-ray computed tomography and grey level co-occurrence matrices as a method for quantification of mineralogy and texture in 3D. *Comput. Geosci.* 111, 105–117.  
<https://doi.org/10.1016/J.CAGEO.2017.11.005>



## CHAPTER 2: Attenuation Coefficients

- Kalender, W.A., 2006. X-ray computed tomography. *Phys. Med. Biol.* 51, R29–R43. <https://doi.org/10.1088/0031-9155/51/13/R03>
- Kaufhold, A., Zacher, G., Halisch, M., Kaufhold, S., 2016. X-ray Computed Tomography Investigation of Structures in Opalinus Clay from Large Scale to Small Scale after Mechanical Testing. *Solid Earth* 7, 1–19. <https://doi.org/10.5194/se-2016-43>
- Ketcham, R.A., Carlson, W.D., 2001. Acquisition , optimization and interpretation of X-ray computed tomographic imagery : applications to the geosciences. *Comput. Geosci.* 27, 381–400.
- Kyle, J.R., Ketcham, R.A., 2015. Application of high resolution X-ray computed tomography to mineral deposit origin, evaluation, and processing. *Ore Geol. Rev.* 65, 821–839. <https://doi.org/10.1016/j.oregeorev.2014.09.034>
- Le Roux, S.G., Du Plessis, A., Rozendaal, A., 2015. The quantitative analysis of tungsten ore using X-ray microCT: Case study. *Comput. Geosci.* 85, 75–80. <https://doi.org/10.1016/j.cageo.2015.09.009>
- Lin, C.L., Miller, J.D., Nguyen, T., Nguyen, A., 2017. Characterization of Breakage and Washability of ROM Coal using X-ray Computed Tomography. *Int. J. Coal Prep. Util.* 1–14. <https://doi.org/10.1080/19392699.2017.1305364>
- Matsubara, K., Ichikawa, K., Murasaki, Y., Hirose, A., Koshida, K., 2014. Accuracy of measuring half- and quarter-value layers and appropriate aperture width of a convenient method using a lead-covered case in X-ray computed tomography. *J. Appl. Clin. Med. Phys.* 15, 309–316. <https://doi.org/10.1120/jacmp.v15i1.4602>
- Mccullough, E.C., 1975. Photon attenuation in computed tomography. *Med. Phys.* 2, 307–320. <https://doi.org/10.1118/1.594199>
- McCullough, E.C., Baker, H.L., Wayne Houser, O., Reese, D.F., 1974. An Evaluation of the Quantitative and Radiation Features of a Scanning X-Ray Transverse Axial Tomograph: The EMI Scanner. *Radiology* 111, 709–715. <https://doi.org/10.1148/111.3.709>
- Mees, F., Swennen, R., Van Geet, M., Jacobs, P., 2003. Applications of X-ray Computed Tomography in the Geosciences, 215th ed. The Geological Society London, London,.
- Miller, J.A., Faber, C., Rowe, C.D., Macey, P.H., du Plessis, A., 2013. Eastward transport of the Monapo Klippe, Mozambique determined from field kinematics and computed tomography and implications for late tectonics in central Gondwana. *Precambrian Res.* 237, 101–115. <https://doi.org/10.1016/j.precamres.2013.09.007>
- Miller, J.D., Lin, C.L., Cortes, A.B., 1990. A Review of X-Ray Computed Tomography and Its Applications in Mineral Processing. *Miner. Process. Extr. Metall. Rev.* 7, 1–18. <https://doi.org/10.1080/08827509008952663>
- Miller, J.D., Lin, C.L., Garcia, C., Arias, H., 2003. Ultimate recovery in heap leaching operations as established from mineral exposure analysis by X-ray microtomography. *Int. J. Miner. Process.* 72, 331–340. [https://doi.org/10.1016/S0301-7516\(03\)00091-7](https://doi.org/10.1016/S0301-7516(03)00091-7)
- Momose, A., Keiichi, H., 1999. The possibility of Phase-Contrast X-Ray Microtomography. *Japanese J. Appl. Physisc* 38, 6250–6269.
- Olarinoye, I., 2011. Variation of effective atomic numbers of some thermoluminescence and phantom materials with photon energies. *Res. J. Chem. Sci.* 1, 64–69.
- Panahi, H., Kobchenko, M., Renard, F., Mazzini, A., Scheibert, J., Dysthe, D., Jamtveit, B., Malthesorenses, A., Meakin, P., 2012. A 4D Synchrotron X-Ray-Tomography Study of the Formation of Hydrocarbon- Migration Pathways in Heated Organic-Rich Shale. *Soc. Pet. Eng. J.* 18, 366–377. <https://doi.org/10.2118/162939-PA>
- Reyes, F., Lin, Q., Udodo, O., Dodds, C., Lee, P.D., Neethling, S.J., 2017. Calibrated X-ray microtomography for mineral ore quantification. *Miner. Eng.* 110, 122–130. <https://doi.org/10.1016/J.MINENG.2017.04.015>
- Siddiqui, I., Solangi, S.H., Soomro, A.A., Warar, M.A., Samoon, M.K., Ajmal, S., 2014. Application of X-ray computed tomography for analyzing cleats and pores for coalbed methane in coal from thar coalfield. *Can. J. pure Appl. Sci.* 8, 2743–2749.
- Sprawls, P., 1993. Physical Principles of Medical Imaging, second ed. ed, The Physical Principles of Medical Imaging. Aspen Publishers, Michigan. <https://doi.org/10.12685/027.7-1-2-32>
- Tanaka, A., Nakano, T., Ikehara, K., 2011. X-ray computerized tomography analysis and density estimation using a sediment core from the Challenger Mound area in the Porcupine Seabight , off Western Ireland. *Earth Planets Sp.* 63, 103–110. <https://doi.org/10.5047/eps.2010.12.006>
- Tsuchiyama, A., Hanamoto, T., Nakashima, Y., Nakano, T., 2000. Quantitative evaluation of attenuation contrast of minerals Tsuchiyama 2000.pdf. *J. Mineral. Petrol. Sci.* 95, 125–137. <https://doi.org/10.2465/jmps.95.125>
- Tsuchiyama, A., Uesugi, K., Nakano, T., Ikeda, S., 2005. Quantitative evaluation of attenuation contrast of X-ray computed tomography images using monochromatized beams. *Am. Mineral.* 90, 132–142. <https://doi.org/10.2138/am.2005.1552>
- Yada, N., Onishi, H., 2016. Validation of Computed Tomography-based Attenuation Correction of Deviation between Theoretical and Actual Values in Four Computed Tomography Scanners. *Asia Ocean. J. Nucl. Med. Biol.* 4, 81–819. <https://doi.org/10.7508/aojnmb.2016.02.004>

## CHAPTER 3: Rapid Scanning Parameters

---

**PAPER PUBLICATION HISTORY**

---

<b>Title</b>	X-Ray Computed Tomography – Determination of Rapid Scanning Parameters for Geometallurgical Analysis of Iron Ore
<b>Journal</b>	The third international AUSIMM Geometallurgy Conference proceedings
<b>Status</b>	Published
<b>Authors and roles</b>	L C Bam – PhD Candidate J A Miller – Primary Supervisor M Becker – Secondary Supervisor F C De Beer – Thesis Advisor I Basson - Thesis Advisor
<b>Applicant Contribution</b>	Conceptualization, Formal analysis, Methodology, Writing—original draft & editing (85%).

---

# X-Ray Computed Tomography – Determination of Rapid Scanning Parameters for Geometallurgical Analysis of Iron Ore

L C Bam<sup>1,2</sup>, J A Miller<sup>3</sup>, M Becker<sup>4</sup>, F C De Beer<sup>5</sup> and I Basson<sup>6,7</sup>

## ABSTRACT

Geometallurgy brings together geologists, mine planners and process engineers to extract meaningful mineralogical and textural information from an ore body, with a view to predicting its metallurgical response. Preferably, automated analytical techniques, which provide mineralogical and textural information should process a large number of samples quickly, relatively inexpensively and reliably. Micro-focus X-ray Computed Tomography ( $\mu$ XCT) is capable of producing 3D volumetric information on texture and mineralogy that satisfies some of these criteria.  $\mu$ XCT has been used extensively to study the porosity and internal pore structure of iron ore pellets as part of downstream processing. It has not been widely applied to earlier mineralogical and textural analysis of unprocessed ore, due to the limited ability of X-rays to penetrate high density samples. In this contribution, we propose scanning methods to overcome this limitation, thereby facilitating a broader application of  $\mu$ XCT to iron ore resource management.

## INTRODUCTION

In the past, iron ore mines have typically exploited high-grade ores, which are characterized as having on the order of 60-67 wt% Fe (Beukes, Gutzmer and Mukhopadhyay, 2002). Because of this high grade, the ore usually requires minimal upfront processing before it is sent for further processing and smelting. Typical contaminants of ore, which cause downstream complications and penalties, thereby requiring further processing, include  $\text{Al}_2\text{O}_3$  >5 wt. %,  $\text{SiO}_2$  >10 wt. % (Rao et al, 2009; Nayak, 2014), clay minerals, Mn, P and base metals (Vatandoost et al, 2013). In contrast, new discoveries of iron ore and expansion of existing iron ore mines focus increasingly on higher tonnage (Aasly and Ellefmo, 2014) but poorer-quality ores, which are typically <60 wt per cent Fe, although in some cases extending to <40% wt% Fe (Das et al, 2007). In these instances, bulk quality criteria need to be met and mineralogical and textural variability of ore needs to be characterized to enable full exploitation of the deposit. These parameters are determined

by geometallurgical models, which require geologists, mine planners and process engineers to extract meaningful mineralogical and textural information (Lund, 2013) in order to represent the full variability of the ore body and to predict its metallurgical response (Newcombe, 2011). Such models tend to be ore deposit-dependent or -specific (Newcombe, 2011; Lund, 2013; Williams, 2013).

The complex and often variable mineralogical characteristics of low-grade ore make it difficult to accurately predict its true processing behavior. This is due to textural variability (e.g. hard, microcrystalline, massive, laminated, conglomeratic) as well as gangue minerals and elements (e.g.  $\text{Al}_2\text{O}_3$ ,  $\text{SiO}_2$ , Mn, clays, base metals). Hapugoda et al, (2011) emphasize mineral characterization to better understand the relationship between minerals of interest and gangue minerals and the way this determines grind size for liberation and beneficiation process performance. Ores with similar Fe grades may show variable processing behavior and product quality, due to differences in gangue texture and mineralogy (Vatandoost et al, 2013; Sinha et

1. PhD candidate, Department of Earth Sciences, Stellenbosch University, Matieland 7601, South Africa.
2. Scientist, Radiography/Tomography Section, NECSA, Radiation Science Department, Pretoria 0001, South Africa. Email: [lunga.bam@necsa.co.za](mailto:lunga.bam@necsa.co.za)
3. Senior Lecturer, Department of Earth Sciences, Stellenbosch University, Matieland 7601, South Africa. Email: [jmiller@sun.ac.za](mailto:jmiller@sun.ac.za)
4. Senior Research Officer, Centre for Minerals Research, Department of Chemical Engineering, University of Cape Town, Rondebosch 7701, South Africa. Email: [megan.becker@uct.ac.za](mailto:megan.becker@uct.ac.za)
5. Chief Scientist, Radiography/Tomography Section, NECSA, Radiation Science Department, Pretoria 0001, South Africa. Email: [frikkie.debeer@necsa.co.za](mailto:frikkie.debeer@necsa.co.za)
6. Extraordinary Senior Lecturer, Department of Earth Sciences, Stellenbosch University, Matieland 7601, South Africa.

## CHAPTER 3: Rapid Scanning Parameters

7. Director, Tect Geological Consulting, Tokai, South Africa, Email: [ianbasson@tect.co.za](mailto:ianbasson@tect.co.za)

al, 2015). As such, it is critical that information concerning these often subtle mineralogical and textural changes is incorporated into the geometallurgical block model, which represents the 3D spatial variability of these parameters.

Characterization of ore texture and mineralogy relies on a suite of analytical techniques to provide robust, reliable and accurate information. Common techniques include scanning electron microscopy (SEM), auto-SEM-EDS techniques (MLA, QEMSCAN, TIMA), optical microscopy and hyperspectral imaging (Hapugoda et al, 2011; Murphy and Monteiro, 2013; Lund, 2013; Jeong and Nousiainen, 2014; Donskoi et al, 2016). Each of these techniques have 'fit for purpose' applications in ore characterization across the minerals beneficiation flowsheet depending on the sample size, particle size, mineralogy, turnaround time and other necessary information required to inform associated decisions (Hapugoda et al, 2011). However, all of the above mentioned techniques provide measurements in 2D and do not capture the full mineralogical and textural variability of the ore in 3D. For successful geometallurgical models, mineralogical and textural measurements must characterize the variability of a large number of samples quickly, relatively inexpensively, reliably, preferably automatically and with minimal sample preparation. Crucially these measurements also need to be linked to beneficiation response so that the geometallurgical block model provides information on feed grade, ore hardness, recovery, product quality and throughput (Lund, 2013). In recent years, 3D micro-focus X-ray computed tomography ( $\mu$ XCT) has been continuously developing as a technology for a wide range of applications. As such there has been a concerted effort in the geosciences and minerals engineering fields to understand the benefits that can be achieved using this technology (Ketcham and Carlson, 2001; Cnudde and Boone, 2013; Hamdani, 2015; Kyle and Ketcham, 2015). One such opportunity is the application of  $\mu$ XCT the geometallurgical characterization of iron ore.

The capability of  $\mu$ XCT to produce 3D volumetric information on texture and mineralogy establishes it as a potential technique for the logging of drill core, analogous to its application in forestry. Here, routine on-line scanning of logs determines density and moisture content, as these parameters are used to optimize the drying process (Wei, Leblon and Racque, 2011). The technique has also been used extensively to study porosity and internal pore structures of iron ore pellets as part of downstream processing (Forsberg and Hjortsberg, 2012; Khozyainov and Yakushina, 2012; Hjortsberg et al, 2013; Yang et al, 2014). However,  $\mu$ XCT has not been widely applied to upstream mineralogical and textural analysis of original or unprocessed iron ore due to limitations in the ability of the X-rays to penetrate high-density samples. In addition, mineralogical characterization is not as straightforward as that applied in automated SEM-EDS techniques, due to the complex nature of the X-ray beam and its sample interaction. Therefore, a more detailed understanding of original sample is required. Comparison of  $\mu$ XCT image slices with auto-SEM-EDS techniques is one means which this can be acquired to develop a working knowledge of the

ore mineralogy and characteristics (Cnudde and Boone, 2013; Nwaila et al, 2013).

In this contribution we outline scanning methods to overcome some of these limitations and consequently to facilitate the broader application of  $\mu$ XCT as a geometallurgical tool. Different  $\mu$ XCT parameters (X-ray energy, exposure time and number of projections) were applied to evaluate image quality. This contribution aims to:

- identify problems associated with scanning high density samples;
- present a procedure to select suitable scanning parameters
- suggests optimal image contrasts for selected scanning parameters.

A complimentary paper by Becker et al, (2016) discusses the potential for XCT as a geometallurgical tool for the analysis of drill core, and proposes an approach for quantification of ore texture in 3D.

## MICRO-FOCUS X-RAY COMPUTED TOMOGRAPHY

Micro-focus X-ray computed tomography ( $\mu$ XCT) or X-ray computed tomography (XCT) is a non-destructive technique that uses an X-ray beam to probe objects or samples in order to visualize the 3D internal structures (Momose and Hirano, 1999; Mees et al, 2003; Davis and Elliott, 2006; Malcolm and Liu, 2011; Tanaka, Nakano and Ikehara, 2011). The principle of XCT is shown in Figure 3.1. Essentially an XCT system consists of an X-Ray source, a sample stage and a flat panel detector. The sample is placed between the source and the detector (Lin and Miller, 2002), and the sample rotates whilst the X-ray source and the detector remain stationary (Cnudde and Boone, 2013). A series of radiographs are obtained during 360° of rotation. This set-up provides stability which is particularly important for high resolution scans, although the quality of output radiographs depends on the set-up of scanning parameters. Radiographs are then reconstructed to form a virtual 3D volume.

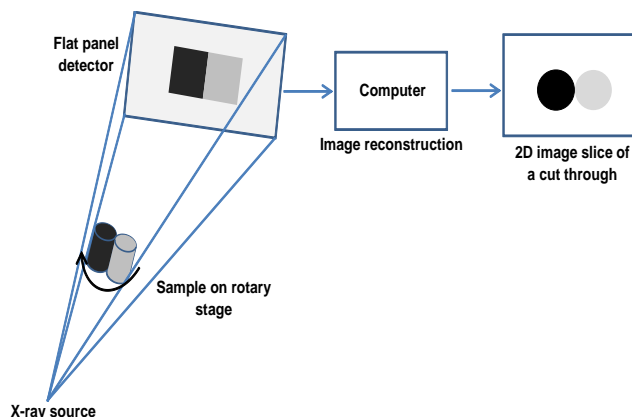


FIG 3.1 – Components and the principle of X-ray computed tomography.

## Scanning Parameters

The quality of the reconstructed volume depends principally on the resolution (voxel size) and image contrast. The resolution is dependent on sample size (Jerram and Higgins, 2007), detector pixel size and X-ray focal spot. The latter two are fixed by the system being used and cannot be modified whilst the sample size can sometimes be reduced to improve resolution. However, the image contrast varies significantly depending on different scanning parameters. Important scanning parameters are X-Ray energy, exposure time, beam current, and number of projections. Different combinations of these parameters provide different image contrasts and determine the quality of the information obtained and acquisition time, however, optimal data acquisition requires proper selection of scanning parameters. Due to recent developments in the capability of XCT, such as increased resolution, high X-Ray beam intensity, energy and decreased scan time, it has also become possible to investigate time-dependent or dynamic processes such as fluid flow that require real-time tomography (Panahi et al, 2012; Myers et al, 2014).

### *X-ray Source and Energy*

The most important parameter of the X-ray source is the focal spot size which determines the maximum energy and beam of the X-Ray beam (Paulus et al, 2000). The X-Ray beam interacts with the sample and is scattered and absorbed by the sample resulting in an attenuated beam that is collected by the detector. The three main processes responsible for attenuation are:

1. photoelectric absorption
2. Compton scattering
3. pair production.

The photoelectric effect is dominant, for geological/mineralogical samples, at low X-ray energies (50 – 100keV). At higher energies (5 – 10MeV) Compton scattering is dominant and beyond this range, pair production attenuation prevails. Unless high X-ray energy sources are used, only photoelectric effects and Compton scattering processes need to be considered (Ketcham and Carlson, 2001). High energy X-rays are much more effective than lower energy ones but are not

ideal to obtain high image contrast. To achieve good image contrast a lower X-Ray energy is often used together with high current to optimize image quality and signal to noise ratio. High current provides high X-ray beam intensity, which is required to improve the underlying counting statistics. In turn, higher intensities require larger focal spots or longer exposure time (Ketcham and Carlson, 2001).

Common laboratory X-ray source produces a polychromatic and continuous spectrum (Baker et al, 2012) with a wide range of energies (Figure 3.2). Due to the nature of the X-ray spectrum, quantitative measurements become complicated through the creation of artefacts in XCT images due to stronger attenuation of X-rays with lower energies (Panahi et al, 2012). In addition, because of the complex nature of the spectrum, the attenuation coefficients of minerals are not easily obtained. To effectively predict the attenuation coefficients of minerals, the effective energy of the spectrum is calculated using the weighted average method. The correlation of the X-ray energy spectrum with its effective energy is shown in Figure 3.3. The weighted average method considers the percentage contribution of each X-ray energy bin of the spectrum relative to the counts. This allows for the improvement of X-ray energy selection to maximize sample contrast and penetration. Prior knowledge on the sample composition and mineralogy is imperative to predict the X-ray energy required for scanning, for a given sample. This allows contrast enhancement by using theoretical attenuation coefficients to select the energy that clearly discriminates the minerals within the sample.

### *Reconstruction*

Reconstruction software currently provides a pre-reconstruction transformation of radiographs. This allows the optimization of contrast and minimization of noise by applying digital filters available within the software. To perform a reconstruction of a specimen, the specimen should be within the field of view during full rotation (3600). For optimized and reconstructed quality images, several common types of artefacts, which are inherent to the XCT technique, needs to be minimized.



### CHAPTER 3: Rapid Scanning Parameters

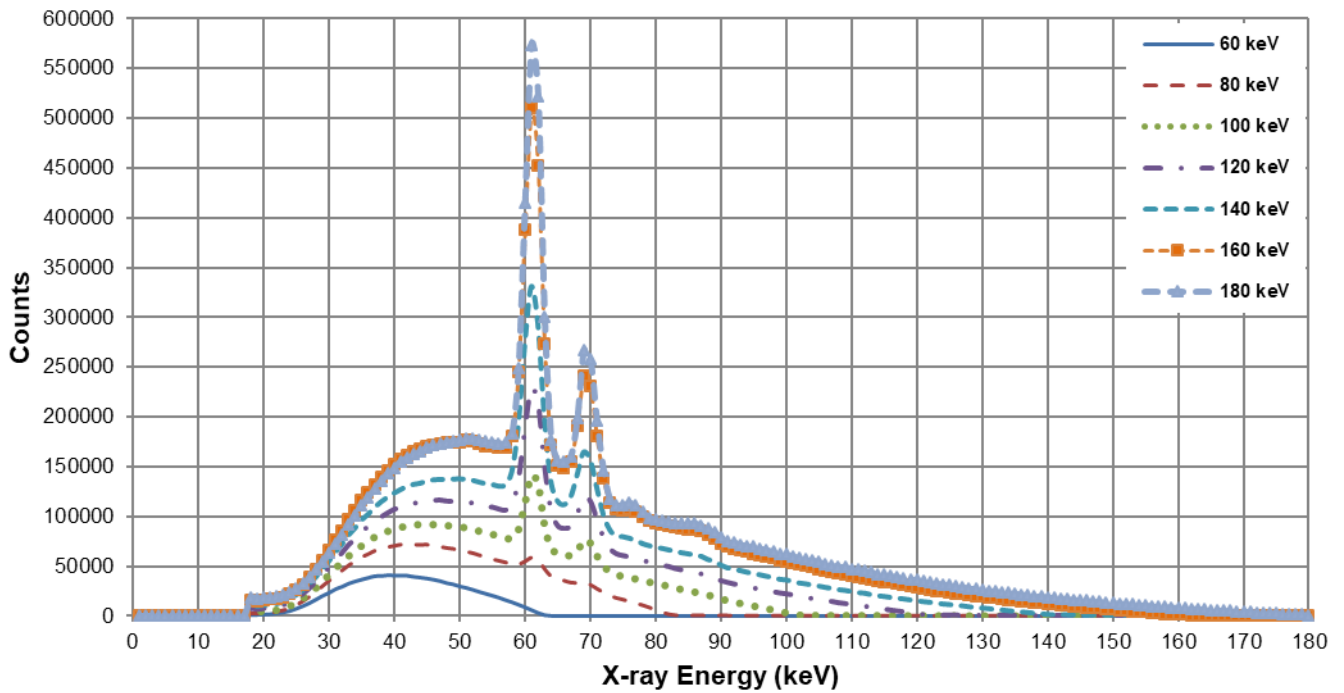


FIG 3.2 – Tungsten X-ray energy beam spectra measured at different energies of 60, 80, 100, 120, 140, 160 and 180 keV.

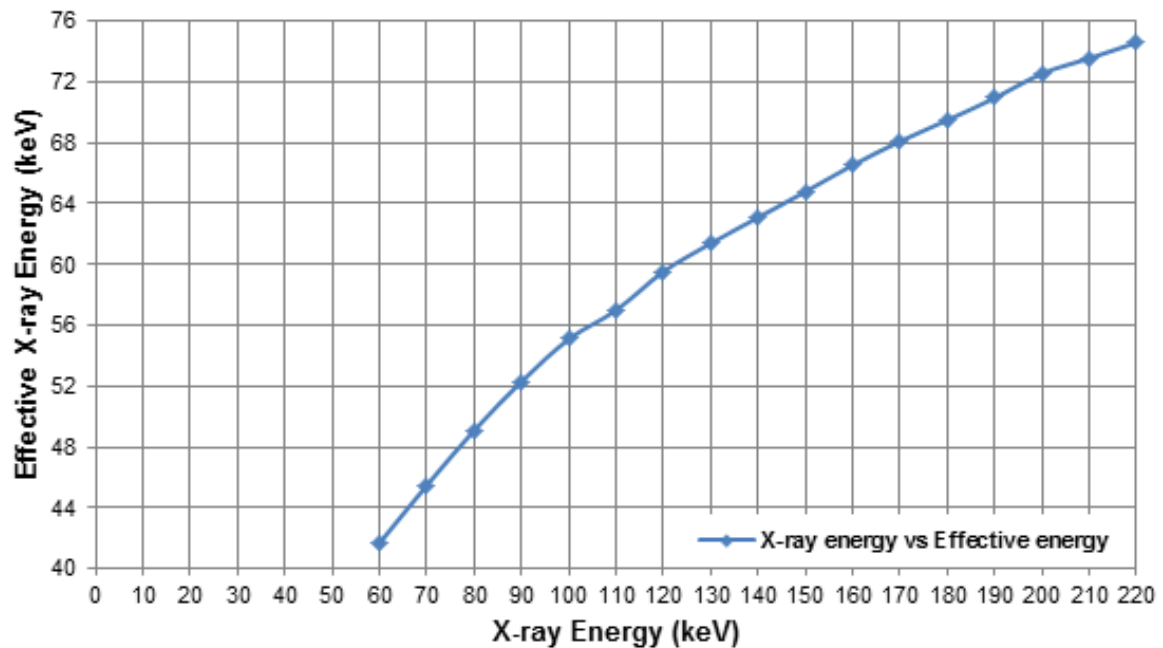


FIG 3.3 – Correlation between X-ray energy spectrums to their effective X-ray energy.

This includes optimizing acquisition conditions and during reconstruction, further reduction of artefacts, such as:

- misalignment artefact due to sample movement, misaligned X-ray source, axis of rotation and misaligned detector
- ring artefacts due to unresponsive or dead pixels of the detector as depicted on Figure 3.4
- line artefacts during reconstruction which are due to minimum number of projections.

The most important artefact in XCT images is beam hardening, particularly when scanning very dense specimens (Figure 3.4). Beam hardening refers to the preferential attenuation of low-energy X-rays when a polychromatic X-ray beam passes through an object (Tsuchiyama et al, 2005; Wildenschild et al, 2002; Malcolm and Liu, 2011). There are several ways to reduce beam hardening effect:

- use of a high energy X-ray beam
- utilization of filter materials which hardens the X-ray beam

- utilization of a beam hardening correction factor which is normally incorporated within many reconstruction software packages (Mees et al, 2003).

Beam hardening artefacts, which prevent quantitative measurement due to poor contrast between two materials of different densities, appear mainly as bright sample borders in the reconstructed slices as depicted in Figure 3.4 (Baker et al, 2012).

### *Signal to noise ratio*

To quantify image quality in tomography, common measures like signal-to-noise (SNR) ratio and contrast are normally used (Dalehaug, 2013; Kraemer, Kovacheva and Lanza, 2015). Noise is one of the main factors that decreases image quality (Kong, 2008; Olubamiji, 2011). Noise usually comes from X-ray photon fluctuation and also from the digital hardware characteristics such as reading out noise (Boas and Fleischmann, 2012). The ultimate source of noise is the random, statistical noise arising from the detection of a finite number of X-ray quanta in the projection measurements (Hanson, 1981). The final image quality of a reconstructed image slice is influenced by all tomographic processes (hardware, scanning parameters, reconstruction and filtering). To minimize noise, the combination of the current with the voltage should meet the proposed standards for penetration, which is between 10 and 20 per cent to reach optimal SNR (Kraemer, Kovacheva and Lanza, 2015). The SNR, effectively a measure of the detectability of an object within a noisy image, describes the ratio between the signal (mean grey value) and the noise (standard deviation of the mean) (Schmidt, 2009) within the region of interest (ROI) (Kraemer, Kovacheva and Lanza, 2015; Kong, 2008).

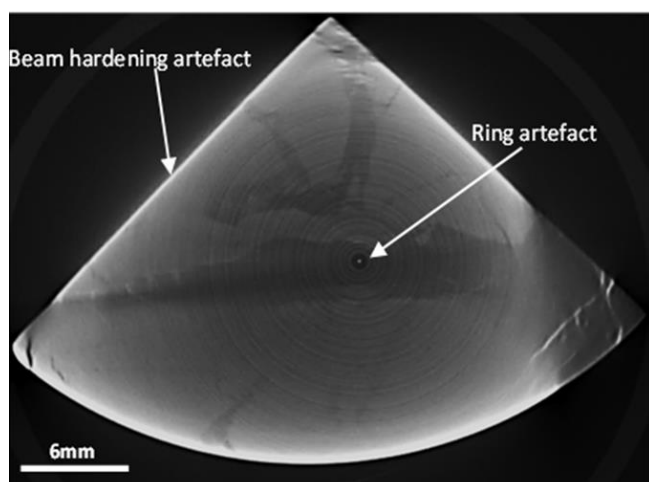


FIG 3.4 – Ring and beam hardening artefacts on an XCT image slice.

## MATERIALS AND METHODS

### Sample Selection and Characterization

The iron ore sample used in this study is a banded iron ore formation containing 45 wt% Fe<sub>2</sub>O<sub>3</sub>. The mineralogy of the sample was initially characterized using an FEI QEMSCAN 650F at the University of Cape Town on coarse iron ore particles ~ 30 mm in size to characterize unbroken ore textures (field images). Figure 3.5 shows an example of a false colour image of a 2D section analyzed by QEMSCAN. The mineralogy is relatively simple with hematite and quartz in equal proportions (other minor phases detected in the QEMSCAN characterization of various ore particles included mica, feldspar, apatite and chlorite). Although the bulk mineralogy is simple, the sample is texturally heterogeneous principally in the variable distribution and form of hematite. This makes scanning rather difficult because hematite has a high average density which hinders X-ray penetration through the sample along the thicker regions of hematite. The iron ore sample was a half cylinder (6 x 13 cm) and to minimize problems due to high density and thickness the sample was cut into two quarter samples. The quarter sample design allows more penetration of X-rays through the sample as it rotates during the acquisition of radiographs, especially along the thinner part of the sample.

### Experimental Approach

A series of experiments were developed to determine the optimal scanning conditions for maximum contrast and signal to noise ratio when scanning high density iron ores. Scans were conducted using a NIKON XTH 225 ST system based at NECSA (South Africa Nuclear Energy Corporation) in the MIXRAD (Micro-focus X-ray Radiography/Tomography) facility (Hoffman and Beer, 2012). This system is a high resolution system consisting of a tungsten target with a 3.7 µm spot size with the ability to scan between 0 and 220 keV. The maximum resolution achievable at the detector is 200 µm which is equal to the detector pixel size. For the optimization of the scanning parameters the experiments were designed in two phases.

#### *Phase One*

Phase one involved determining the optimal X-ray energy to scan the iron ore quarter core, to optimize exposure time and number of projections in phase two. The sample was subjected to different X-ray energies (60 to 180 keV) with an increment of 20 keV to determine the required minimum or maximum X-ray energy. The selected X-ray energy was paired with a current high enough to give 10 per cent X-ray penetration. To minimize experimental error the sample was not moved from the X-ray system for the duration of scanning. A similar grey value range was used to calculate the 10 per cent X-ray penetration to minimize analysis error. The selected exposure time for this phase was kept constant at 0.354 sec and this is the minimum exposure time that produces the minimum image contrast required for the reconstruction. The number of projections were

## CHAPTER 3: Rapid Scanning Parameters

determined using the Nyquist sampling theorem (Lange and Hentschel, 2007). This was performed by measuring the number of pixels on a radiograph covering the longest x-axis of the sample and multiplying with  $\pi/2$ . The resulting number of 773 is the minimum number of projections to represent information at a 68  $\mu\text{m}$  scanning resolution. This also means that information at 68  $\mu\text{m}$  resolution would not be quantifiable by using fewer projections than are suggested by the theorem unless all particles/grains within the sample are  $>68 \mu\text{m}$ . The number of projections are also resolution dependent due to the sample size. To minimize noise and artefacts the number of projections was increased by a third to 1030

and all scans were conducted with this number of projections to determine optimal X-ray energy.

### Phase Two

Phase two was used to determine the optimal exposure time and number of projections using the optimal X-Ray energy determined in phase one. The exposure time was varied between 0.354 and 4 sec to determine the required exposure time for optimal contrast and SNR ratio. The number of projections were varied between 258 and 1030, in order to evaluate the required number of projections that produce a reconstructed image slice

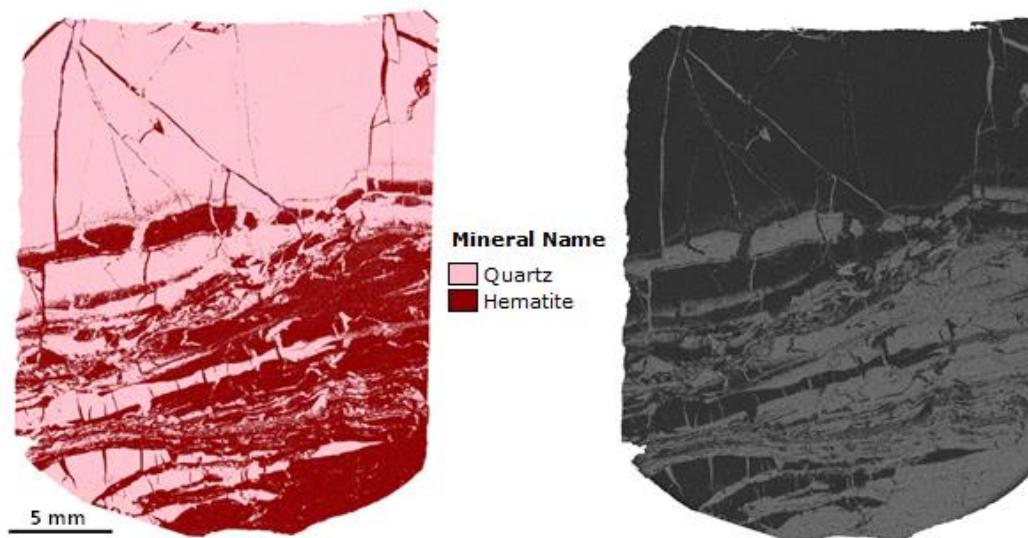


FIG 3.5 – (a) QEMSCAN false colour image and (b) backscattered electron (BSE) image illustrating the heterogeneous iron ore texture. The darker and lighter grey values on the BSE image represent quartz and hematite respectively.

with the least noise. The number of projections less than 773 (which is also referred to as undersampling) were used to determine the effect of a larger angle of rotation to image contrast. Due to the longer time required to conduct these scans, 1030 was used as a maximum number of projections. This also allowed enough time in between the scans to remove the afterglow effect on the detector due to excessive use of the detector. During radiograph acquisition using different parameters, the sample was not removed from the sample stage to allow direct measurements of contrast and SNR at the same position on the image slice.

### Image Reconstruction

The acquired radiographs were reconstructed using the CT Pro 3D reconstruction software. This applies a mathematical back-projection procedure to transform 2D radiographs into a virtual 3D volumetric data (Tsuchiyama et al, 2005). The reconstruction software provides an open window to assess the automatic reconstruction process. The window displays a slice at a specific position of the sample and this slice can be changed by the user to assess the default reconstruction value on other slices. All scans were reconstructed at the same slice position and using the automated reconstruction option to minimize human error. The reconstruction was performed in two ways: (a) reconstruction without beam hardening correction and (b) reconstruction with beam hardening correction. The

sample was cropped to minimize image and volume size, whilst the same axes dimensions were applied to all the scans to obtain the same image and volume size.

### Volume Analysis

The reconstructed data was analyzed using VGStudio rendering software version 2.2, which allows rendering of the sample in 3D. Upon loading of the volume data, a calibration method was used to maintain a similar grey value range for all the samples. This required defining the sample background and the grey value of the mineral of interest in 2D. Image slices appear in three views:

1. top view
2. right view
3. front view.

Only top view image slices were saved and used for further image analysis in the open-source software imageJ. To minimize false image contrasts, no contrast enhancement was performed on the image histogram.



## RESULTS

### X-ray Attenuation

Figure 3.6 shows a plot of the linear attenuation coefficient of hematite and quartz as a function of X-ray effective energy. The hematite attenuation coefficient decreases as the X-ray energy is increased. However, there is little change in the attenuation coefficient of quartz as the X-ray energy is increased. Attenuation coefficients were calculated using an in-house

spreadsheet, compiled from information on the NIST website (<http://physics.nist.gov/PhysRefData/XrayMassCoef/tab3.html>). The spreadsheet requires inputs of X-ray energy, density of a compound and number of elements within the compound. The output is an attenuation coefficient of the selected mineral or compound. From the attenuation coefficient plot, it is evident that theoretical discrimination between hematite and quartz is pronounced. In practice, the required X-ray energy for scanning depends on sample thickness and geometry as well as the distribution of dense minerals.

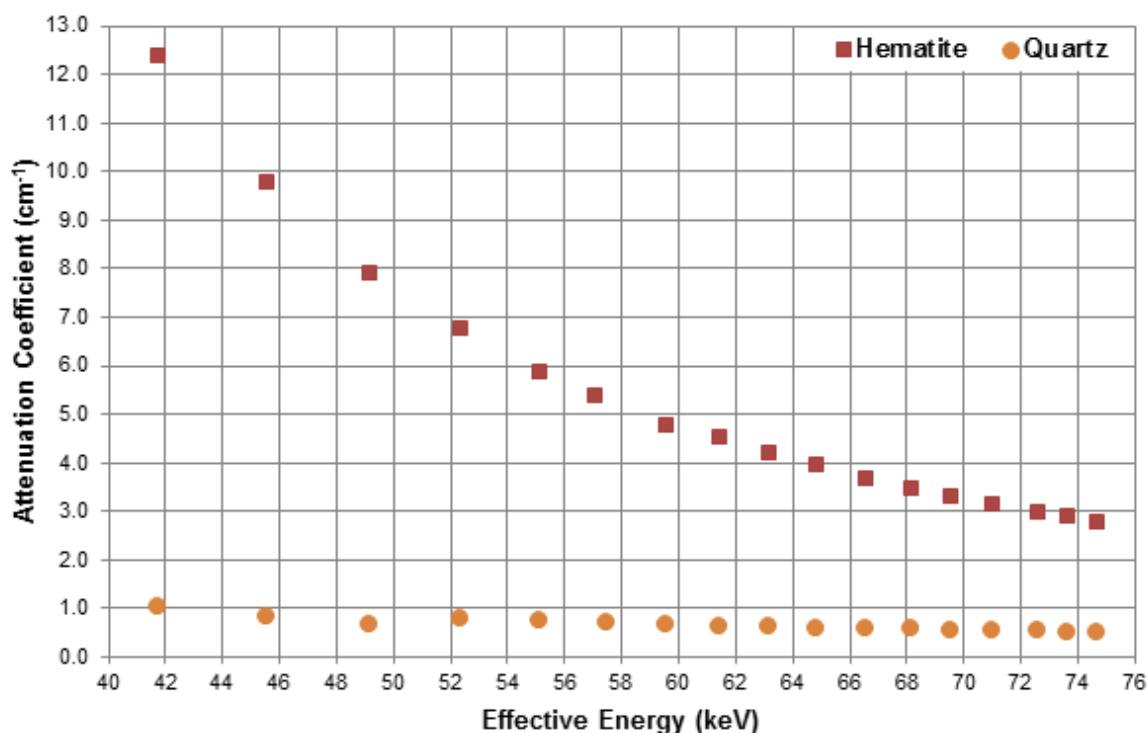


FIG 3.6 – Attenuation coefficient for hematite and quartz as a function of effective energy.

### X-ray Penetration and Contrast

There is no contrast and no quantification without X-ray penetration. Different X-ray energies were varied from 60 to 180 keV and are demonstrated in Figure 3.7. Visual image contrast improvement is observable between 60 the 80keV image slices; beyond the 80keV, visual inspection to determine optimal contrast is limited. A subjective visual assessment by the user is not a reliable means to judge the image quality correctly (Kraemer, Kovacheva and Lanza, 2015) and a more quantified approach is necessary. From Figure 3.8, it is clear that poor image contrast is associated with low X-ray energy, whilst an increase in X-ray energy improves image quality for a specific X-ray energy range. Hematite and

quartz contrast were calculated based on the yellow boxes drawn on Figure 3.7 on the 100 and 120keV image slices. The boxes were drawn on the same position across all image slices. The optimal image contrast was achieved between 140 and 180keV. By referring to Figure 3.3; 140, 160 and 180keV are equivalent to 63.1, 66.54 and 69.5keV which are effective energies of the applied X-ray energy spectrum. For optimal image contrast 140keV (63.1keV) was selected due to high contrast, Figure 3.8. The theoretically calculated attenuation coefficient is also higher at 63.10 (4.24 cm⁻¹) compared to 66.54 (3.97 cm⁻¹) and 69.50keV (3.72 cm⁻¹), Figure 3.6. The attenuation coefficient difference for both hematite and quartz is also larger at 63.10 compared to 66.54 and 69.50keV which provides improved image contrast.

### CHAPTER 3: Rapid Scanning Parameters

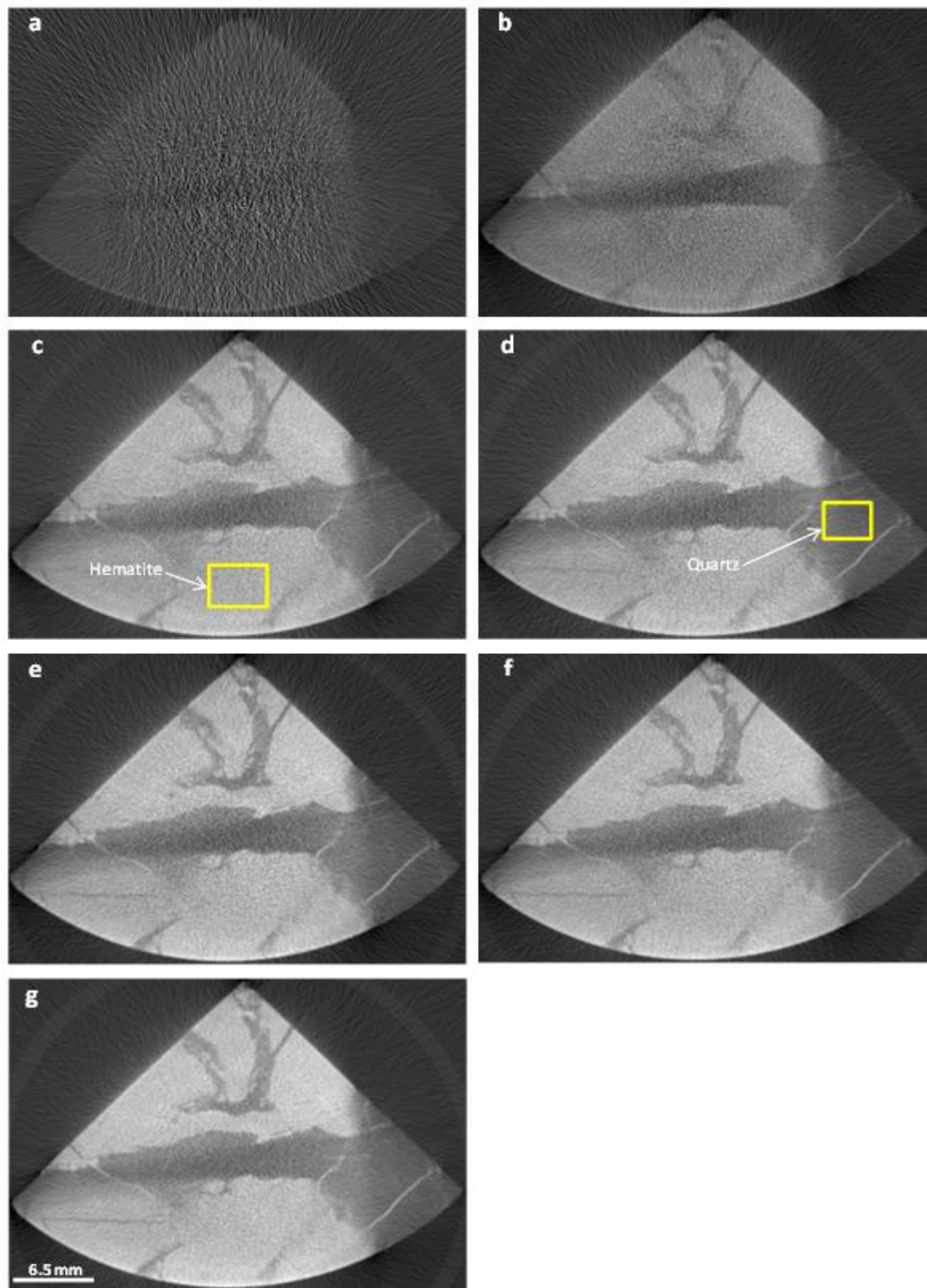


FIG 3.7 – Shows the effect on increasing X-ray energy to image contrast at (a) 60keV, (b) 80keV, (c) 100keV, (d) 120keV, (e) 140keV, (f) 160keV and (g) 180keV. Detectable contrast difference is only visual between 60 and 80keV, beyond 100keV it is rather difficult to differentiate contrast between the image slices.

## CHAPTER 3: Rapid Scanning Parameters

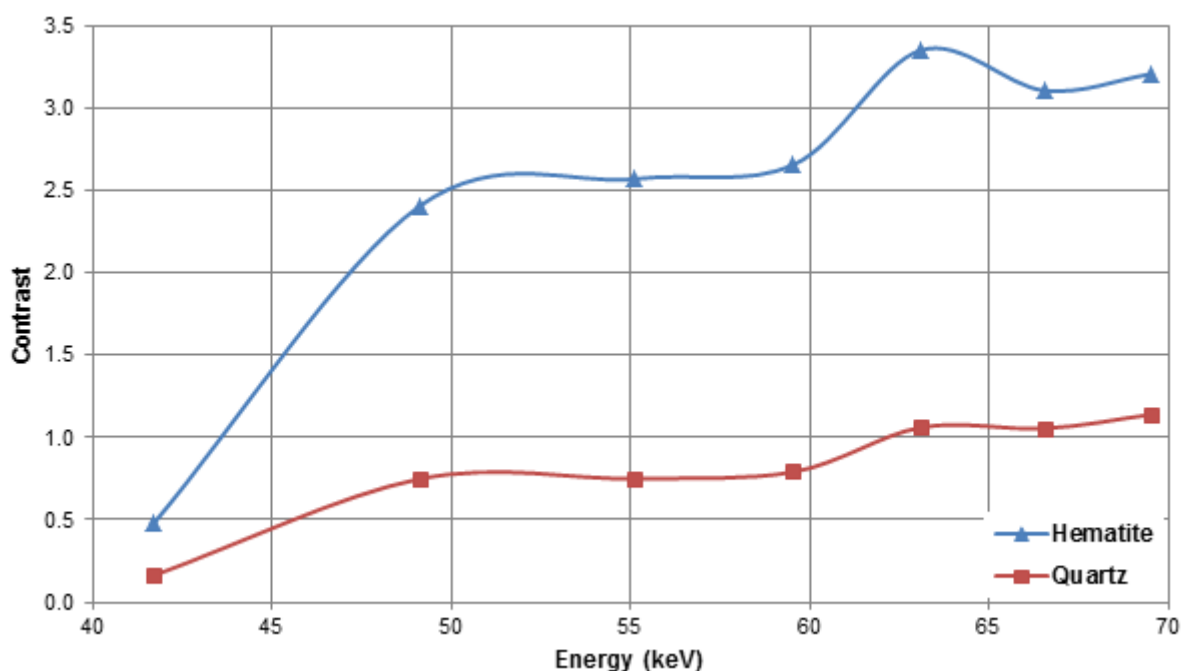


FIG 3.8 – Contrast distribution as a function of energy for hematite and quartz.

## Beam Hardening Correction

The applied beam hardening correction is built into the CT Pro 3D reconstruction software. Such a correction removes the difference in grey values that represent the same mineral/material. The degree of the correction varies between 1 and 6. Samples with overall lower density are usually reconstructed using the value of 1 (no effect or correction). Depending on the attenuation of the X-ray beam through the sample, the value is gradually increased until the white lines on the edges of the sample are removed. For the quarter sample the correction value used to minimize beam hardening was 3. The plastic, cylindrical sample container was used to monitor the effect of beam hardening correction on the sample. Values greater than 3 are too aggressive and affect the distinction between plastic, background and quartz grey values. For instance, quartz regions on Figure 3.9(a) are not clearly visible for discriminative quantification measurements, compared to Figure 3.9(d) after a beam hardening correction has been applied. Both line and histogram profiles on Figure 3.9(e) and (f) show major improvements after beam hardening correction, which is vital when scanning hematitic ore samples. Note that both the histogram and line profile were drawn on the same region of the image slices before and after beam hardening correction, for the purpose of direct comparison.

## Signal to Noise Ratio

The SNR and sample contrast (hematite and quartz contrast) were quantified within the yellow boxes drawn on Figure 3.10(a) and (e). The SNR of hematite on figure 3.10(b) increases with the number of projections beyond 258. No increase in SNR beyond 515 projections occurred and only fluctuations were observed. The beam hardening correction improves hematite SNR. Increasing

the number of projections also increases SNR and it is highest for 1030 projections as depicted on Figure 3.10(f). Quartz SNR on Figure 3.10(c) also shows many fluctuations between 258 and 1030 projections regardless of increasing number of projections. However, the beam hardening correction removes this fluctuation and a slight increase in SNR is observed above 258, Figure 3.10(g). The sample contrast also showed a major increase after beam hardening correction was applied, Figure 3.10(h). The contrast doubled which demonstrates the effect beam hardening has on the image information. The hematite SNR and sample contrast on Figure 3.10(b), (d), (f) and (h) show a decrease at 2 sec exposure time and 773 projections. This was attributed to the ring artefact. The exposure time shows minimal effect on the SNR as it is increased for all number of projections. Due to this 0.354 sec was selected as the optimal exposure time to scan the quarter sample coupled with 1030 projections due to higher SNR.

## DISCUSSION

The developed method can be applied to any iron ore samples with similar sample dimensions, resolution and hematite content. It is unbiased to XCT systems and sample geometry, however a minimum of 10 per cent penetration is a requirement for scanning. If penetration is less than 10% due to different sample geometry and hematite content, the entire procedure of phase one and two should be repeated to determine the optimal parameters for scanning. XCT system geometries (distance from the X-ray source to a detector), focal spot and detector sizes differ from system to system. Due to this reason the sample scanning resolution and number of projections would change. The number of projections can then be re-calculated by applying Nyquist sampling theorem as mentioned under phase one.

## CHAPTER 3: Rapid Scanning Parameters

The determined scanning parameters resulted in high quality images by using SNR and image contrast as indicators for rapid scanning. These images can thereafter be used for

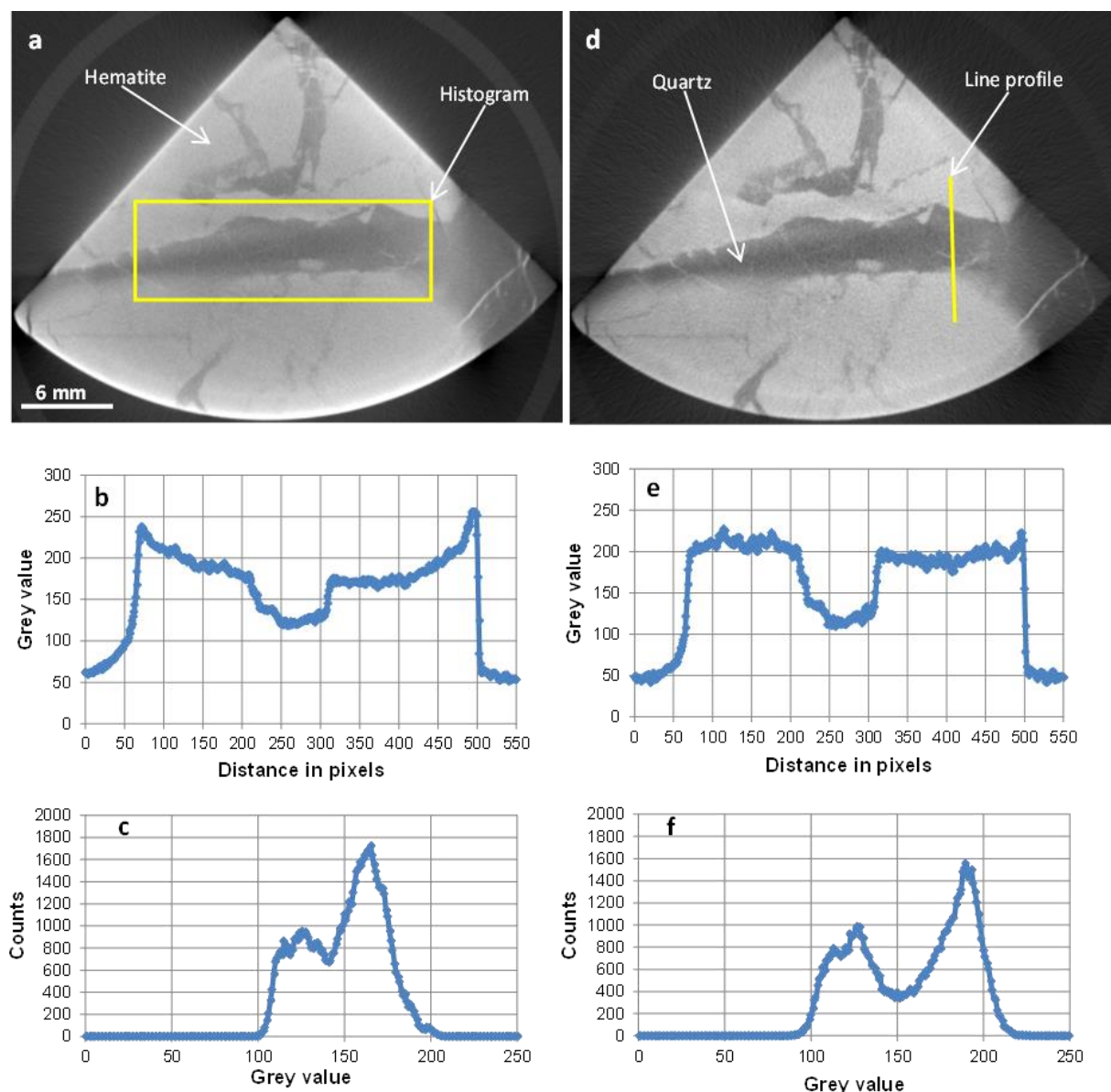


FIG 3.9 - (a) Image slice with no beam hardening correction applied, (b) and (c) line and histogram profile distribution for grey values for both hematite and quartz before beam hardening correction, (d) image slice with beam hardening correction applied, (e) and (f) line and histogram profile distribution of hematite and quartz grey values after beam hardening correction.

3D visualization, and more importantly - quantification. This quantification may include parameters such as: porosity, permeability, 'simple' bulk mineralogy, grain shape and grain size distribution, mineral association and texture (Kyle and Ketcham, 2015). These output parameters can be considered key inputs to geometallurgical models (Hoal, Woodhead and Smith, 2013). In the context of iron ore, the recent paper by Donskoi et al, (2016), emphasised the importance of textural information for the understanding, prediction and optimization of downstream processing performance. A number of case studies were used to illustrate this using a 2D optical image analysis system for automated textural characterisation developed by CSIRO (Donskoi et al, 2016). In an accompanying paper to this study, a method for 3D quantification of texture from XCT

volumes has been proposed (Becker et al, 2016). The method is based on 3D grey level co-occurrence matrices and showcased for a nickel sulfide ore.

The ability of XCT to rapidly provide 3D mineralogical and textural information positions the technique as a potential analytical tool for implementation on mining sites. This capability broadens the application of XCT into geometallurgy, from drill core logging through to minerals processing. The concept of XCT logging would ideally be paired with other 'sensors' to provide complimentary information to develop robust knowledge (Mutina and Bruyndonckx, 2013) of the ore characteristics and the variability thereof. This will improve the accuracy of ore body block modelling and its ability to predict the distribution of minerals of interest

## CHAPTER 3: Rapid Scanning Parameters

and their association with gangue minerals. Accurate block models result in reduced mining costs and allow better management of ore variability. Rapid scanning

facilitates large numbers of samples being processed for proper ore characterization on mine operational time frames.

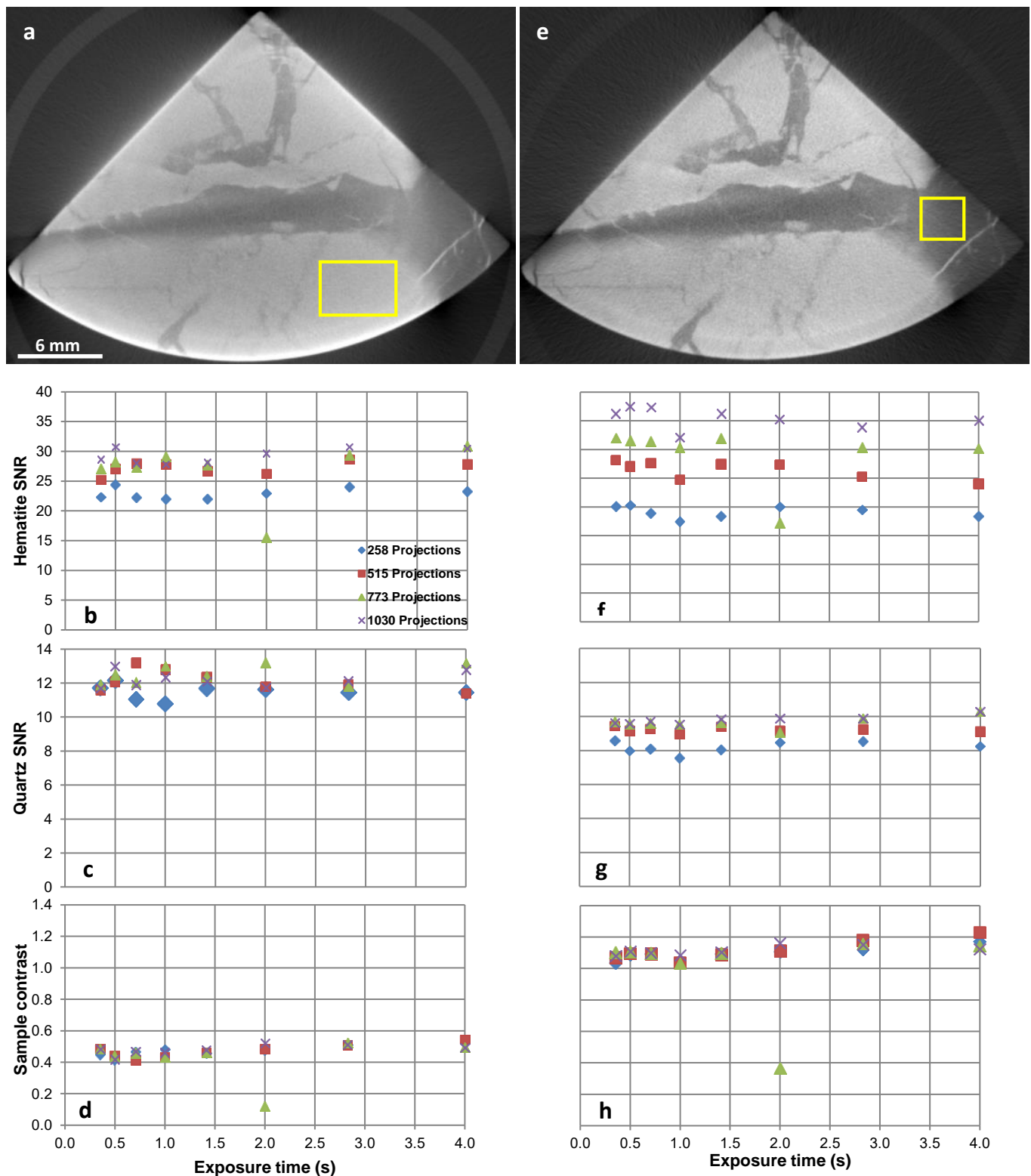


FIG 10 – (a) Image slice before beam hardening correction; (b, c and d) hematite signal to noise ratio (SNR), quartz SNR, and sample contrast (hematite and quartz contrast) before beam hardening correction; (e) image slice after beam hardening; (f, g and h) hematite SNR, quartz SNR and sample contrast after beam hardening corrections has been applied.



## CONCLUSION

- A robust methodology has been developed to scan the hematite ore. Further work is recommended to validate on different iron ore mineralogy and geometry including cylindrical geometry.
- The availability of rapid 3D mineralogical and textural information for the characterization of the ore meets the requirements of a geometallurgical test (quick scanning and analysis, easily accessible data and minimal sample preparation). Ultimately this information needs to be coupled with the minerals processing response.
- With the constant development of XCT systems and continuously improving scanning methods, the XCT is seen as one of the most influential techniques within the near future for the characterization of ores to aid minerals processing for the production of high quality products.

## ACKNOWLEDGEMENTS

The authors would like to thank NECSA and the management team for funding and access to the Micro-Focus system in the MIXRAD Lab, which is a DST-NRF (Department of Science and Technology – National Research Funding) funded facility through the NEP-RISP (National Equipment Programme – Research Infrastructure Support Programme) program. The project is generously supported through the South African Minerals to Metals Research Initiative. This work is based on the research supported in part by the National Research Foundation of South Africa (Grant Numbers 86054, 85533). Any opinions, findings and conclusions or recommendations expressed in any publication generated by the NRF supported research is that of the author(s), and that the NRF accepts no liability whatsoever in this regard.

## REFERENCES

- Aasly, K and Ellefmo, S, 2014. Geometallurgy applied to industrial minerals operations. *Mineralproduksjon*, 1170(5), pp.21–34.
- Baker, D R, Mancini, L, Polacci, M, Higgins, M D, Gualda, G A R and Hill, R J, 2012. An introduction to the application of X-ray microtomography to the three-dimensional study of igneous rocks. *Lithos*, 148, pp.262–276.
- Becker, M, Jardine, M A, Miller, J A and Harris, M, 2016. X-ray Computed Tomography: A geometallurgical tool for 3D textural analysis of drill core? In *3rd AusIMM International Geometallurgy Conference*.
- Beukes, N J, Gutzmer, J and Mukhopadhyay, J, 2002. The geology and genesis of high-grade hematite iron ore deposits. In *Australian Institute of Mining and Metallurgy Publication Series*. pp. 23 – 29.
- Boas, F E, and Fleischmann, D, 2012. CT artifacts : Causes and reduction techniques. *Imaging Med*, 4, pp.229–240.
- Cnudde, V and Boone, M N, 2013. High-resolution X-ray computed tomography in geosciences: a review of the current technology and applications. *Earth Science Reviews*, 123, pp.1–17.
- Dalehaug, I, 2013. *Optimization in CT*. Norwegian University of Science and Technology.
- Das, B, Prakash, S, Das, S K and Reddy, P S R, 2007. Effective Beneficiation of Low Grade Iron Ore Through Jigging Operation. *Journal of Minerals & Materials Characterization & Engineering*, 7, pp.27–37.
- Davis, G R, and Elliott, J C, 2006. Artefacts in X-ray microtomography of materials. *Materials Science and Technology*, 22(9).
- Donskoi, E, Poliakov, A, Holmes, R, Suthers, S, Ware, N, Manuel, J and Clout, J, 2016. Iron ore textural information is the key for prediction of downstream process performance. *Minerals Engineering*, 86, pp.10–23.
- Forsberg, F and Hjortsberg, E, 2012. X-ray microtomography for sequential imaging and analysis of iron ore pellets under reduction. In *6th International Congress on the Science and Technology of Ironmaking*. pp. 1744–1753.
- Hamdani, A H, 2015. X-Ray Computed Tomography Analysis of Sajau Coal , Berau Basin , Indonesia : 3D Imaging of Cleat and Microcleat Characteristics. *Internationa Journal of Geophysics*, 2015.
- Hanson, K M, 1981. Noise and contrast discrimination in computed tomography. In T. H. Newton & D. G. Potts, eds. *Technical Aspects of Computed Tomography*. St. Louis Missouri: C.V. Mosby, pp. 3941–3955.
- Hapugoda, S, Manuel, J R, Peterson, M J and Donskoi, E, 2011. Determination of Iron Ore and Gangue Mineral Associations using Optical and Backscattered Electron Images with Electron Probe Microanalysis. In *IRON ORE CONFERENCE*.
- Hjortsberg, E, Forsberg, F, Gustafsson, G and Rutqvist, E, 2013. X-ray microtomography for characterisation of cracks in iron ore pellets after reduction. *Ironmaking and Steelmaking: Processes, Products and Application*, 40(6), pp.399–406.
- Hoal, K O, Woodhead, J and Smith, K S, 2013. The Importance of Mineralogical Input into Geometallurgy Programs. In *The second AUSIMM international geometallurgy conference*. pp. 17–25.
- Hoffman, J W and Beer, F C, 2012. Characteristics of the Micro-Focus X-ray Tomography Facility (MIXRAD) at Necsa in South Africa. In *18th World Conference on Nondestructive Testing*. pp. 1–12.
- Jeong, G Y and Nousiainen, T, 2014. TEM analysis of the internal structures and mineralogy of Asian dust particles and the implications for optical modeling. *Atmospheric Chemistry and Physics*, 14(14), pp.7233–7254.
- Jerram, D A and Higgins, M D, 2007. 3D Analysis of Rock Textures : Quantifying Igneous Microstructures. *ELEMENTS*, 3(4), pp.239–245.
- Ketcham, R A and Carlson, W D, 2001. Acquisition , optimization and interpretation of X-ray computed tomographic imagery: applications to the geosciences. *Computers & Geosciences*, 27, pp.381–400.

## CHAPTER 3: Rapid Scanning Parameters

- Khozyainov, M S and Yakushina, O A, 2012. X-ray Computed Tomography Analysis of Geomaterials. In *Advanced Research in Scientific Areas*. pp. 1490–1494.
- Kong, F, 2008. Quality Evaluation for Digital Radiography Inspection Based on Imaging Parameters. In *17th World Conference on Nondestructive Testing*. Shangai, pp. 1–5.
- Kraemer, A, Kovacheva, E and Lanza, G, 2015. Projection based evaluation of CT image quality in dimensional metrology. In *Digital Industrial Radiology and Computed Tomography*. pp. 1–10.
- Kyle, J R and Ketcham, R A, 2015. Application of high resolution X-ray computed tomography to mineral deposit origin, evaluation, and processing. *Ore Geology Reviews*, 65, pp.821–839.
- Lange, A and Hentschel, M P, 2007. Direct Iterative Reconstruction of Computed Tomography Trajectories (DIRECTT). In *International Symposium on Digital industrial Radiology and Computed Tomography*. Lyon, pp. 1–10.
- Lin, C and Miller, J D, 2002. Cone beam X-ray microtomography - a new facility for three-dimensional analysis of multiphase materials. *MINERALS & METALLURGICAL PROCESSING*, 19(2), pp.65–71.
- Lund, C, 2013. Mineralogical, Chemical and Textural Characterisation of the Malmberget Iron Ore Deposit for a Geometallurgical Model. Lulea University of Technology.
- Malcolm, A A and Liu, T, 2011. Case Studies in the Use of Computed Tomography for Non-Destructive Testing , Failure Analysis and Performance Evaluation. In *Singapore International NDT Conference & Exhibition*. pp. 1–15.
- Mees, F, Swennen, R, Van Geet, M and Jacobs, P, 2003. *Applications of X-ray Computed Tomography in the Geosciences* 215th (ed: F. Mees et al), (The Geological Society London: London).
- Momose, A and Hirano, K, 1999. The Possibility of Phase-Contrast X-Ray Microtomography. *Japanese Journal of Applied Physisc*, 38(1), pp.625–629.
- Murphy, R J and Monteiro, S T, 2013. Mapping the distribution of ferric iron minerals on a vertical mine face using derivative analysis of hyperspectral imagery (430–970nm). *ISPRS Journal of Photogrammetry and Remote Sensing*, 75, pp.29–39.
- Mutina, A and Bruyndonckx, P, 2013. Combined micro-X-ray tomography and micro-X-ray fluorescence study of reservoir rocks: applicability to core analysis. *Microscopy and Analysis - Compositional Analysis Supplement*, 27(4), pp.4–6.
- Myers, G R, Geleta, M, Kingston, A M, Recur, B, and Adrian, P, 2014. Improving dynamic tomography , through Maximum a Posteriori estimation. In *Proceedings of SPIE*. pp. 1–9.
- Nayak, N P, 2014. Mineralogical Characterization of Goethite- Lateritic Ore & its Implication on Beneficiation. *International Journal of Engineering Sciences & Research Technology*, 3(11), pp.288–291.
- Newcombe, B, 2011. Lessons Learned from Geometallurgical Investigations Carried Out on a Nickel Sulfi de Flotation Plant. In S. Dominy, ed. *The First AusIMM International Geometallurgy Conference*. Australasian Institute of Mining and Metallurgy, pp. 139–150.
- Nwaila, G, Becker, M, Ghorbani, Y, Petersen, J, Reid, D L, Bam, L C, de Beer, F C and Franzidis, J-P, 2013. A geometallurgical study of the Witwatersrand gold ore at Carletonville, South Africa. In *The Second AusIMM International Geometallurgy Conference*. The Australasian Institute of Mining and Metallurgy: Melbourne, pp. 75–84.
- Olubamiji, A, 2011. The Influence of Filtration , Tube Current and Number of Projections on CBCT Image quality. Tempere University of Technology.
- Panahi, H, Kobchenko, M, Renard, F, Mazzini, A, Scheibert, J, Dysthe, D, Jamtveit, B, Malthé-Sorenses, A and Meakin, P, 2012. A 4D Synchrotron X-Ray-Tomography Study of the Formation of Hydrocarbon- Migration Pathways in Heated Organic-Rich Shale. *SPE Journal of Petroleum Engineers*, 18(2), pp.366–377.
- Paulus, M J, Gleason, S S, Kennel, S J, Hunsicker, P R and Johnson, D K, 2000. High Resolution X-ray Computed Tomography : An Emerging Tool for Small Animal Cancer Research. *Neoplasia*, 2(1-2), pp.62–70.
- Rao, D S, Kumar, T V V, Rao, S S, Prabhakar, S and Raju, G B, 2009. Mineralogy and Geochemistry of A Low Grade Iron Ore Sample from Bellary-Hospet Sector , India and Their Implications on Beneficiation. *Journal of Minerals & Materials Characterization & Engineering*, 8(2), pp.115–132.
- Schmidt, T G, 2009. Optimal “image-based” weighting for energy-resolved CT. *Medical Physics*, 36(7), pp.3018–3027.
- Sinha, M, Nistala, S H, Chandra, S and Mankhand, T R, 2015. Mineralogy of Iron Ores of Different Alumina Levels from Singhbhum Belt and Their Implication on Sintering Process. *Journal of Minerals and Materials Characterization and Engineering*, 3, pp.180–193.
- Tanaka, A, Nakano, T and Ikehara, K, 2011. X-ray computerized tomography analysis and density estimation using a sediment core from the Challenger Mound area in the Porcupine Seabight , off Western Ireland. *Earth Planets and Space*, 63(2), pp.103–110.
- Tsuchiyama, A, Uesugi, K, Nakano, T and Ikeda, S, 2005. Quantitative evaluation of attenuation contrast of X-ray computed tomography images using monochromatized beams. *American Mineralogist*, 90, pp.132–142.
- Vatandoost, A, Beven, B J, Campbell-Hardwick, S and Young, J, 2013. A Geometallurgical Approach for Iron Ore Product Evaluation. In *The Second AusIMM International Geometallurgy Conference*. Melbourne, pp. 259–266.
- Wei, Q, Leblon, B and La Rocque, A, 2011. On the use of X-ray computed tomography for determining wood properties: a review. *Canadian Journal of Forest Research*, 41, pp.2120–2140.
- Wildenschild, D, Hopmans, J W, Vaz, C M P, Rivers, M L, Rikard, D and Christensen, B S B, 2002. Using X-ray computed tomography in hydrology : systems , resolutions , and limitations. *Journal of Hydrology*, 267, pp.285–297.
- Williams, S R, 2013. A Historical Perspective of the Application and Success of Geometallurgical Methodologies. In *The Second AUSIMM International*

### CHAPTER 3: Rapid Scanning Parameters

*Geometallurgy Conference*. Brisbane: The Australasian Institute of Mining and Metallurgy, pp. 37–47.

Yang, B H, Wu, A X, Miao, X X, Liu, J Z, 2014. 3D characterization and analysis of pore structure of packed

ore particle beds based on computed tomography images. *Transactions of Nonferrous Metals Society of China (English Edition)*, 24(3), pp.833–838.



## Supplementary notes on scanning parameters

Provided below are supplementary notes outlining additional information on the determination of rapid scanning parameters on dense samples as undertaken in Chapter 3. The supplementary notes have been added to give better context to the scanning parameters that were being optimized. The determination of rapid scanning parameters depends on the sample being scanned and the scanning parameters (exposure time, number of projections, current, and X-ray energy or voltage) required to represent the true sample information. Samples with high density or high attenuating phases will require different scanning parameters as compared to the ones with less attenuating phases.

### *Focal Spot size*

The focal spot size of a XCT system should be maintained in order to minimise errors associated with an increased spot size. This is important because the focal spot size determines the X-ray flux and resolution capability of the XCT system. To maintain the focal spot size the combination of the voltage (kV) and current ( $\mu\text{m}$ ) of the X-ray beam should not have a resulting power (W) greater than the scanning resolution. The XCT system used in this study does allow the resulting power to be well controlled or locked such that an increase in the voltage does not change the focal spot size to be larger than the required scanning resolution. However, the system does allow the power to be increased slightly beyond the scanning resolution but there is a limit, (e.g. the scanning resolution of  $3\mu\text{m}$  should not have a power greater than 7W in order to minimise errors associated with an increased spot size). The scanning resolution for the samples in this case was  $68\mu\text{m}$  due to the larger sample size. Because of this, the current was increased to make sure that a 10% X-ray penetration was achieved. The increased spot size was not an issue in this case because the power of the X-ray beam was not more than 68W which did not affect the scanning resolution and sample information. Although not the case in this study, an overly increased spot size gives a false scanning resolution, which can affect the true dimensions of the particle or grain sizes at that resolution. More information about the system (NIKON XTH 225 ST system) can be found in this website <https://www.nikonmetrology.com/en-us/product/xt-h-225-st>.

### *X-ray Energy*

The X-ray energy spectrum of the XCT system determines the penetrating capability through the sample. To determine the optimal X-ray energy the sample was exposed to different X-ray spectrum energies (60 to 180keV). This was done to obtain a minimum of 10% X-ray penetration and optimal sample contrast when paired with the current. The X-ray energy spectrum that provided optimal and similar sample contrast was between 140keV and 180keV which led to the selection of a 140keV X-ray energy spectrum with an effective energy of 63.1keV. This X-ray energy was then used to scan the sample and evaluate other scanning parameters such as the number of projections and exposure time. Sample contrast was determined by dividing the mean grey value of hematite with that of quartz.

### *Number of Projections*

The number of projections when scanning high density samples are very important because they determine the quality of the sample information at the scanning resolution. To determine the required number of projections for any scanning resolution, the Nyquist theorem method was used. The method determined the number of projections to be 773. This means is that the Nyquist method determined the required number of projections given the resolution ( $68\mu\text{m}$ ) and sample width as discussed under Phase One section in the published manuscript. The resolution was determined by the sample height in order to capture the full sample. The hematite and quartz grains are very large as shown in Figure 3.7 of this chapter and the scanning resolution was adequate to resolve the individual particles. A

minimum of 8 voxels is required to define any particle or grain shape at any scanning resolution and this was achievable in this case due to larger hematite and quartz grain sizes.

However, although the number of projections were determined using the Nyquist method as mentioned above, in reality more projections were evaluated. The evaluated number of projections were 258, 515, 773 and 1030. The projections were evaluated using signal-to-noise ratio (SNR) in order to determine the optimal number of projections for this particular study. The highest SNR was associated with 1030 number of projections. The SNR in this case is defined as a measure of the detectability of an object within a noisy image, and describes the ratio between the signal (mean grey value) and the noise (standard deviation of the mean) within the region of interest.

### *Filter Materials*

The utilisation of different filter materials is important because they optimise X-ray penetration and sample information especially when dealing with high density samples. However, in this case the filter materials were not used due to the geometry of the sample, distribution and amount of hematite within the sample. The application of a beam hardening correction during the reconstruction was found to be adequate to correct for beam hardening artefacts in this case as discussed under the Beam Hardening Correction section and as shown in Figure 3.9 (b) and (e).

### *Beam Hardening and Exposure Time Evaluation*

The evaluation of beam hardening when dealing with high density samples is important in order to determine its impact on the sample information. To do this, the SNR ratio was determined for both quartz and hematite by using a region of interest (ROI) to assess the quality of the sample information. The ROI for quartz was selected close to a hematite region to check how different scanning parameters (number of projections and exposure time) would improve this regions SNR. The process would be biased by selecting a quartz region that is less affected by beam hardening. This would imply that the beam hardening is either decreasing or increasing which would not be the case.

Selecting ROIs for quartz that are further from hematite or high impact beam hardening would result in higher SNR with increasing exposure time and number of projections. However, this would be irrelevant and not give more information about the impact of beam hardening (on both quartz and hematite) which is the focus of this study. The motivation behind this study is to use SNR as a guideline or indicator to select optimal and rapid scanning parameters with minimised beam hardening. Therefore, after carefully evaluating all the combinations of the scanning parameters using SNR, the rapid scanning parameters were determined to be 0.354 sec, 1030 number of projections, 140keV spectrum energy (63.1keV effective energy) and beam hardening correction factor of 3. These parameters allowed the sample to be scanned in less than 7 minutes.

---

**PAPER PUBLICATION HISTORY**

---

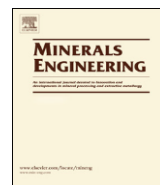
<b>Title</b>	X-ray Computed Tomography: Practical Evaluation of Beam Hardening in iron ore samples.
<b>Journal</b>	Minerals Engineering
<b>Status</b>	Published
<b>Authors and roles</b>	L C Bam – PhD Candidate J A Miller – Primary Supervisor M Becker – Secondary Supervisor I J Basson – Thesis Advisor
<b>Applicant Contribution</b>	Conceptualization, Formal analysis, Methodology, Writing—original draft & editing (85%).

---



Contents lists available at ScienceDirect

Minerals Engineering

Journal homepage: [www.elsevier.com/locate/mineng](http://www.elsevier.com/locate/mineng)

# X-ray Computed Tomography: Practical Evaluation of Beam Hardening in iron ore samples

Lunga Cleartone Bam <sup>a,c\*</sup>, Jodie Ann Miller <sup>a</sup>, Megan Becker <sup>b</sup>, Ian James Basson <sup>a,c</sup>*a* Department of Earth Sciences, Stellenbosch University, Private Bag X1, Matieland 7601, South Africa*b* Centre for Minerals Research, Department of Chemical Engineering, University of Cape Town, Private Bag, Rondebosch 7701, South Africa*c* Tect Geological Consulting, Unit 3 Metrohm House, Paardevlei, South Africa*d* Department Radiation Science, Necsa, PO Box 582, Pretoria, South Africa

## ARTICLE INFO

### Keywords:

X-ray tomography  
Beam Hardening  
Noise  
Loss of information

## ABSTRACT

X-ray computed tomography is a non-destructive 3D analytical technique, which in recent years has gained more widespread applications to characterise the internal structure of materials in minerals processing and metallurgical studies. Successful application of the technique relies on effective X-ray penetration. Ore samples with high average specific gravities (e.g. iron ore, massive sulfide ores) inhibit X-Ray penetration causing beam hardening artefacts that reduce data quality and limit further analysis. This contribution presents a practical way to evaluate the degree of beam hardening using a case study iron ore sample. The method quantifies the degree of beam hardening that leads to a loss of sample information, through comparing the known pore surface area of an aluminium standard sample with that of an iron ore sample. This comparison is defined as a %Error. Porosity and sample mineralogy are confidently quantified when the %Error is less than 10%. Above 10%, there is inconsistent loss of sample information (porosity and relatively low dense sample mineralogy) and the results from the volumes cannot be trusted which indicates that smaller sample sizes need to be scanned. This practical method can be routinely applied in other applications and samples with density higher than iron ore.

## 1. Introduction

The ability to characterise and quantify the internal structure of rocks, minerals, particles, drill core and packed particle beds has made X-ray computed tomography (XCT) an increasingly popular method of 'ore characterisation' within both the geosciences and minerals engineering studies (Cnudde and Boone, 2013; Mees et al., 2003; Wang et al., 2015). Its non-destructive ability to rapidly scan samples, and easily locate dense phases typically representing valuable base metal sulphides, gold and platinum group mineral (PGM) grains, further adds to its attractiveness, especially when dealing with low grade ores (g/t). In addition, the method does not suffer from stereological error which is encountered when measurements are made from 2D particle sections (Evans and Morrison, 2016; Spencer and Sutherland, 2000), for example those routinely prepared for process mineralogy using automated scanning electron microscope with energy

dispersive spectrometry (auto SEM-EDS) technologies such as QEMSCAN, MLA, TIMA, and Mineralogic.

Specific uses of XCT with respect to minerals engineering include characterisation and quantification of mineralogy and texture within drill core samples, which is important since it provides an indication of the ore characteristics ahead of mining and processing (Jardine et al., 2018; Lin et al., 2017a). This would include quantification of the grain size distribution of valuable minerals that can be used to define the required grinding for liberation (Evans et al., 2015). Following grinding, XCT provides a means of assessing the potential separation efficiency (Lin et al., 2017a; Miller et al., 2009). Other applications of XCT in process engineering include the analysis of the distribution of defects within particles after comminution to further understand the mechanisms of particle breakage, as well as differences between comminution devices (Charikinya et al., 2015; Garcia et al., 2009). In

\* Corresponding author at: Department of Earth Sciences, Stellenbosch University, Private Bag X1, Matieland 7601, South Africa.  
E-mail addresses: [lunga.bam@necsa.co.za](mailto:lunga.bam@necsa.co.za) (L.C. Bam), [jmiller@sun.ac.za](mailto:jmiller@sun.ac.za) (J.A. Miller), [megan.becker@uct.ac.za](mailto:megan.becker@uct.ac.za) (M. Becker), [ianbasson@tect.co.za](mailto:ianbasson@tect.co.za) (I.J. Basson).

<https://doi.org/10.1016/j.mineng.2018.11.010>

Received 6 June 2018; Received in revised form 12 September 2018; Accepted 7 November 2018

0892-6875/ © 2018 Elsevier Ltd. All rights reserved.

leaching studies, XCT has been used to understand leach progression on both the particle scale, as well as through a packed bed (Dhawan et al., 2012; Fagan-Endres et al., 2017; Ghorbani et al., 2011). Possible future applications of XCT could even extend to its use as an online technology for routine characterisation of run of mine ore (Lin et al., 2017b).

In all of the above examples, efficient application of the XCT relies on the ability of the X-ray beam to be able to penetrate the sample in order to resolve the internal geometry. This condition is best met when there is a pronounced variation in atomic composition between minerals of interest (Mees et al., 2003). However, where a pronounced variation in atomic compositions is absent or where all atomic compositions are very similar, a situation commonly encountered with many of the ore minerals that are treated in minerals processing and metallurgy, XCT is not able to highlight or resolve features of interest. This represents the techniques' primary limitation. The XCT technique maps out the spatial distribution of X-ray attenuation which increases with increasing atomic number or density (Louis et al., 2006). The difference in X-ray linear attenuation provides a contrast which can be used for mineral differentiation based on their differing densities (Koeberl, 2002; Mees et al., 2003). Contrast is a function of X-ray energy, beam current, exposure time and the number of projections obtained (Bam et al., 2016; Kraemer et al., 2015). Improper utilisation of these parameters results in poor image contrast, noisy images and artefacts that render the resultant data unusable.

In high density samples X-ray penetration is important because it allows optimal image contrast, quantification of information within a scanning resolution, and reduces image noise and beam hardening. Contrast optimization requires the elimination of common XCT artefacts during reconstruction such as: a) beam hardening artefact, which is related to the presence of dense objects; b) ring artefact, which is related to the detector pixel defect; c) line artefact, which is related to the presence of anomalously bright pixels in the radiographs and d) misalignment artefact, which is related to the imperfect alignment of source, detector and axis of rotation (Mees et al., 2003). Current and past research focussed on eliminating beam hardening artefacts through utilisation of different filter materials and the optimization of different mathematical models to correct for the variation in linear attenuation coefficient or grey value variations of single dense materials (Ketcham and Hanna, 2014; Meganck et al., 2009; Stowe and Curran, 2016; Van de Castele, 2004). However, to our knowledge there has been no analysis to evaluate the amount of information that is simply lost from denser and thicker samples due to beam hardening artefacts or whether this information can be recovered.

The features most affected by beam hardening artefacts are (1) porosity and (2) differentiation of relatively low density minerals such as silicates and carbonates (which in many cases represent the gangue minerals in ores). The effects of beam hardening become more pronounced with increasing

sample size and density. The utilisation of XCT to quantify porosity is fairly simple, because in most cases the density difference between pore spaces and sample matrix or minerals is large. In high density materials like iron ore and massive sulphide ores, the quantification of pore information is not straight forward because of the inherent noise introduced by beam hardening artefacts. In the case of iron ore, knowledge of porosity and textural characteristics are relevant for predicting and optimising downstream processing (Clout and Manuel, 2015; Donskoi et al., 2016).

The aim of this paper is to develop a practical way to evaluate the loss of sample information due to beam hardening in high density materials. The evaluation of information loss is done using iron ore as a case study but the principles are applicable to many high density ore types. The practical evaluation was achieved by introducing a standard aluminium sample, with known properties, to indirectly evaluate the beam hardening and to determine the optimal sample size that results in a minimum of beam hardening artefacts and information loss. The results have important implications for minerals processing because the loss of sample information may bias ore characterisation, and consequently lead to incorrect interpretations of the efficiencies and deficiencies in minerals processing circuits.

## 2. Artefacts in X-ray tomography

Unavoidable artefacts are common in most XCT systems. In most cases, the artefact type is a function of sample properties or improper utilisation of the XCT system, in terms of parameter settings and reconstruction (Schulze et al., 2011). There are many different types of XCT artefacts, of which the most common are ring, metal, scatter, motion, cone beam, beam hardening and noise (Boas and Fleischmann, 2012).

### 2.1. Common Artefacts

Ring artefacts, created by unresponsive or uncalibrated detector pixels/elements are visible as concentric rings centred around the location of the axis of rotation (Davis and Elliott, 2006), and are particularly prominent when scanning homogeneous samples (Schulze et al., 2011). The artefact can be eliminated by moving the detector or specimen slightly (viz. a few pixels) between projections, to reduce the severity of the ring artefact (Davis and Elliott, 2006). Metal artefact is caused by the presence of high density materials, during the filter back projection reconstruction. This is a streaking or star-shaped artefact that degrade image quality and obscure valuable information (Mouton and Megherbi, 2013). Scattering artefact is caused by the diffracted X-ray beam deviating from its original path after interacting with the sample, thereby disproportionately increasing the measured intensities of other areas in the sample. Scatter causes streak artefact similar to that caused by beam hardening and also reduces sample contrast (Schulze et al., 2011; Siewerdsen et al., 2006). This artefact is usually minimised by changing the object-to-detector gap,



limiting the field of view, using of an anti-scatter grid and by applying an algorithmic correction of X-ray scatter (Siewerdsen et al., 2006). Motion artefact is the result of the misalignment of X-ray source, object and detector, causing inconsistencies in the back-projection reconstruction process. Given that the X-ray source and detector are stationary and only the object is moving during the scanning process, the reconstruction does not account for the movement because it is not integrated in the reconstruction process (Schulze et al., 2011). This artefact causes blurring and double edges along sample edges. The above artefacts are systematic and result from the X-ray source, sample stage, detector behaviour and characteristics and are relatively fixed. Sample induced artefacts, which include beam hardening and noise, are variable and depend on the size, geometry and composition of the sample. These artefacts are explained below.

## 2.2. Beam Hardening

Beam hardening artefacts, from scanning samples with high density compositions, are attributed to the polychromatic nature of X-ray sources of current lab-based XCT systems. As the polychromatic X-ray beam passes through dense samples, lower X-ray energies are absorbed more than high X-ray energies. This result in an X-ray beam that is depleted in lower energies, hence the phrase “hardening”. This hardened beam is attenuated less as it continues to penetrate the sample (Wildenschild and Sheppard, 2013). The X-ray beam initially experiences a higher effective attenuation coefficient at the beginning of its passage through the material, compared to further in, resulting in the grey value variation within reconstructed images of uniform material to appear more attenuated near the edges (Bam et al., 2016; Wildenschild and Sheppard, 2013). There are several ways to minimize beam hardening artefacts: a) use of a high energy X-ray beam; b) utilisation of filter materials which harden the X-ray beam; c) smaller samples and d) utilisation of beam hardening correction factors which are incorporated within many reconstruction software packages (Bam et al., 2016; Ketcham and Carlson, 2001; Mees et al., 2003; Wildenschild et al., 2002). Utilisation of synchrotron technology eliminates beam hardening artefacts because of the monochromatic nature of the high flux radiation (Wildenschild et al., 2002) but the current technology of lab-based XCT systems has not met the level of a synchrotron X-ray source.

A number of studies have examined methods to optimally eliminate beam hardening artefacts. Hardware filtering is one of the most popular methods to reduce beam hardening (Van de Castele, 2004). Meganck et al. (2009) and Ay et al. (2013) have shown the advantages of utilising different filter materials to minimise beam hardening artefacts, but this results in prolonged scanning times, on the order of a few hours. Prolonged scan times would limit the online application of XCT for routine characterisation of high density ores for process mineralogy, although an attempt has been made to determine the shortest scanning time possible (on the order of a few minutes) whilst still achieving optimal image contrast with high signal-to-noise ratio in the case of iron ores (Bam et al., 2016). Another

commonly-applied method for beam hardening correction is the linearization procedure, which corrects the experimentally-measured attenuation coefficients curve with respect to thickness, such that it corresponds to an expected linear curve. The main disadvantage is that the method only works on a two-component system (e.g. air and some material). Van de Castele (2004) demonstrated the use of a bimodal energy model which corrects for the beam hardening artefacts for a multi-component system, compared to the linearization of a two-component system. Ketcham and Hanna (2014) developed an iterative optimization algorithm to find a generalized, spline-interpolated transform that minimizes the beam hardening artefacts. This corrects the affected areas of the sample instead of correcting the entire sample although its disadvantage is that it can introduce secondary artefacts or over-correct. Stowe and Curran (2016) demonstrated a predictive correction method to suppress beam hardening streak artefacts, which performed better than commercially available streak artefact correction methods, but was inferior to iterative reconstruction. Most beam hardening correction methods were developed based on a well-known sample composition, density and thickness characterisation (Ketcham and Hanna, 2014). The application of these approaches to heterogeneous samples wherein the correction is typically highly nonlinear (Park et al., 2016, 2015) is significantly more complex and has not yet been attempted.

## 2.3. Noise

Noise is defined as an unwanted random or non-randomly distributed disturbance of a signal that tends to obscure the signal's information content (Jaju et al., 2013). There are two sets of noise that need to be considered in reconstructed images: a) additive noise that stems from round-off errors or electrical noise and b) photon-count noise (quantum noise) that should follow a Poisson distribution (Schulze et al., 2011). Noise manifests as inconsistent attenuation coefficients or grey values in the reconstructed image or larger deviations in areas where a constant attenuation is expected (Schulze et al., 2011). From a qualitative point of view, noise makes small features more difficult to identify. If the signal-to-noise ratio (SNR) is low, it can result in additional holes, which are perceived as pores, with a diameter equal to the pixel or voxel size. The ability to segment features based on grey values or attenuation coefficient is consequently more difficult. When the effect of noise is not large for a given sample, the linear attenuation coefficient may be determined by taking an average over many voxels, a technique which becomes possible due to the insignificant standard error, in turn due to the increased number of voxels used to determine the average linear attenuation coefficient (Davis and Elliott, 2006). However, the determination of linear attenuation coefficient would not be possible when dealing with beam hardening and scattering artefacts due to the increased standard error.

Like all imaging techniques, X-ray imaging is subject to noise. The lower limit of this noise level is determined by the number of detected photons and equals Poisson noise (Cnudde and Boone, 2013). In practice, image noise is a function of many parameters

such as resolution and sample size; it is not constant throughout the image and it is higher at the centre of the sample due to the increased X-ray attenuation, while it is anisotropic in the reconstructed images. This is noticeable in samples with a higher aspect ratio such that X-rays passing along the longer dimension are highly attenuated resulting in random streaks. Images of solid specimens or higher attenuating materials will have a lower SNR than those with high porosity. However SNR is optimal when X-ray penetration is about 16% or higher through the centre of the sample (Davis and Elliott, 2006).

### 3. Methodology

#### 3.1. Sample Preparation

The methodology for evaluating the degree of beam hardening uses a hematite stepped-wedge to quantify the loss of information. An aluminium cylindrical sample was also used as a standard reference sample and scanned together with a stepped-wedge sample in order to correlate the deviation of the quantified pore surface area of the aluminium standard sample with the degree of beam hardening of the hematite stepped-wedge sample.

##### 3.1.1. Hematite Stepped-wedge

The normal sample geometry for beam hardening evaluation is cylindrical in order to keep the X-ray penetration constant throughout. However, the geometry and the distribution of high density materials/minerals do not always allow constant X-ray penetration. A hematite (SG 5.3) stepped wedge (53 x 20mm) with five thickness levels of 4, 14, 24, 34 and 47mm, respectively, was manufactured to evaluate the impact of beam hardening in a consistently non-cylindrical sample. The hematite stepped-wedge sample also had a specularite crystal vein running through all the thicknesses of the sample and was used to evaluate the impact of the beam hardening artefacts (Fig. 4.1.). The evaluation of beam hardening artefact is not unique to iron ore only. Sample materials with similar or greater densities than hematite can also be cut in a stepped-wedge design to evaluate the impact of beam hardening.

##### 3.1.2. Core Samples

A series of apatite-magnetite drill cores from the Norrbotten Province in Sweden were selected to assess the effect of different sample geometries and thicknesses on X-ray penetration. The samples consist of magnetite (SG 5.18), ferromagnesian silicates, mica and amphibole (SG 3-3.2), apatite (SG 3.2) and Na-feldspar (SG 2.65), similar to samples used by (Lund, 2013). Samples were cut into different geometries (diameter x height): cylindrical (38 x 34mm), half cylinder (19 x 34mm) and quarter cylinder (17 x 20mm) in order to vary their thicknesses (Fig. 4.2).

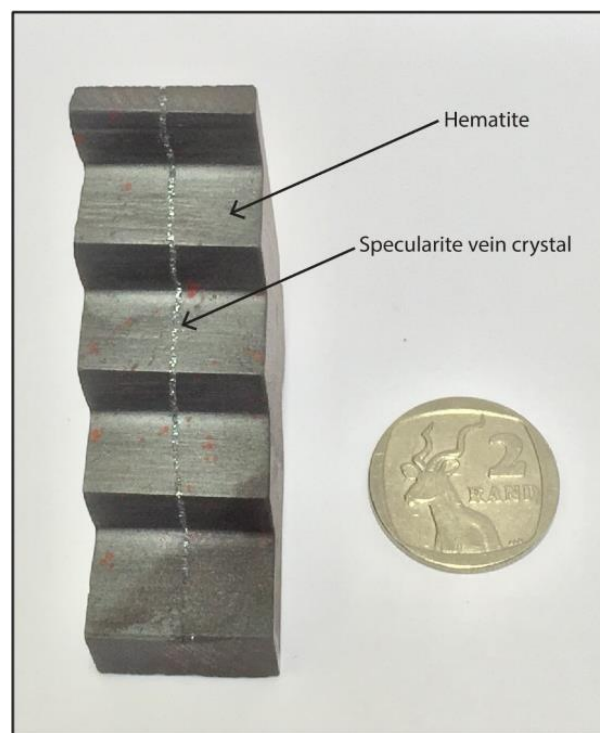


**Fig 4.1.** Hematite stepped-wedge sample with different thickness.

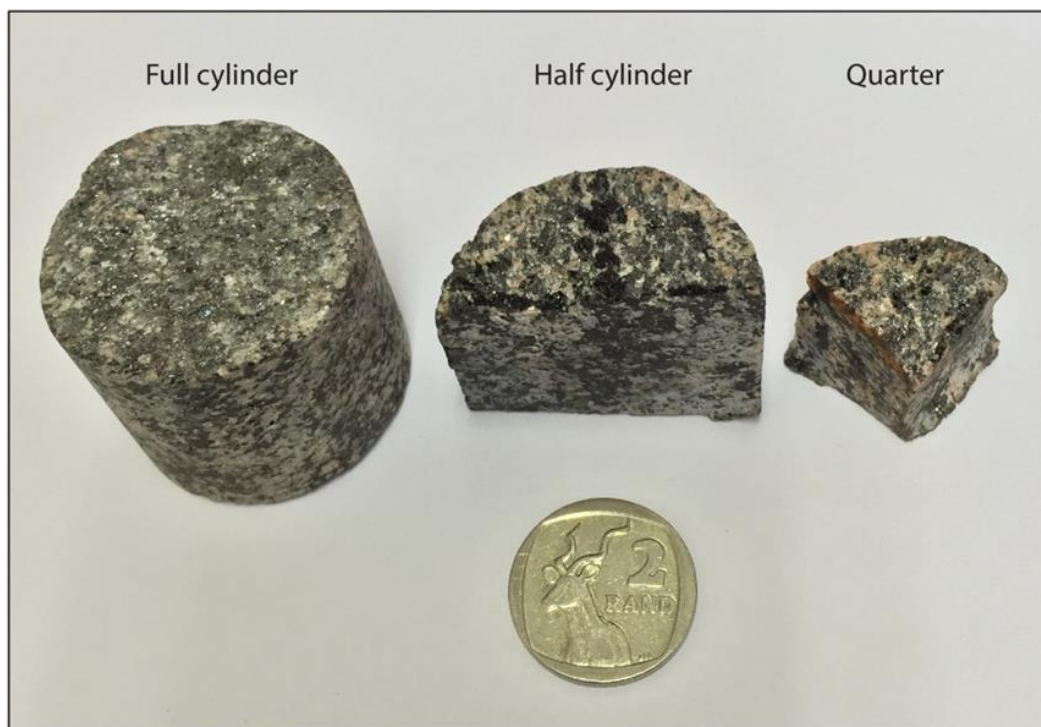


**Fig 4.2.** Different sample geometries of apatite-magnetite cores to evaluate beam hardening effect due to different geometries: cylindrical (38 x 34mm), half cylinder (19 x 34mm) and quarter cylinder (17 x 20mm).

### 3.1.3. Aluminium Standard Sample

A cylindrical aluminium standard sample was manufactured to indirectly assess the effect of beam hardening. A 2mm diameter vertical pore was drilled through the sample to assess the quality of the scan (Fig. 4.3). For the stepped-wedge set-up, the aluminium standard sample was placed behind the stepped-wedge sample in order to evaluate the impact of beam hardening for every thickness increment. For the core samples, the aluminium standard sample was placed behind the longest path length of each sample geometry because they are prone to beam hardening artefacts.

### 3.2. Scanning Protocol

Samples were scanned at different X-ray energies (100 to 180 keV) with an increment of 20keV to evaluate beam hardening, and quantify porosity information and scan quality with increasing X-ray energy. The combination of X-ray energy and beam current was selected such that image saturation was avoided. The density difference between hematite and air is large and it is reasonably expected that quantified porosity information should be consistent or within an acceptable error margin. Different X-ray energies also provides a means of assessing the optimal X-ray energy for scanning, based on optimal signal-to-noise ratio and contrast (Bam et al., 2016). All samples were scanned at the same resolution of 0.0328mm to minimise biases associated with varying grey values at different scanning resolutions. All the samples were scanned at 4 second exposure time with 2000 projections to improve sample penetration, image contrast and to decrease noise within images. For background correction for each radiograph the X-ray system (Nikon XTH 225 ST) uses a built in shading correction method that acquires a dark and bright

images to correct for background and normalize the grey value variation on the radiographs during scanning (Hoffman and de Beer, 2012).

The scans were reconstructed using CT Pro 3D reconstruction software which has a built in beam hardening correction method which can be used to minimize beam hardening artefact for any sample material. The degree of correction varies between 1 and 6 and the applied degree of correction for this work was 3, similarly to the one used by Bam et al. (2016). After reconstruction the data was analysed using VGStudio 3.1 software in order to generate image slices. The image slices were further evaluated using ImageJ software in order to assess the impact of beam hardening with respect to sample size. A combination of aluminium (1mm) and copper (1mm) filter materials were used during scanning to minimise the impact of beam hardening (Meganck et al., 2009).

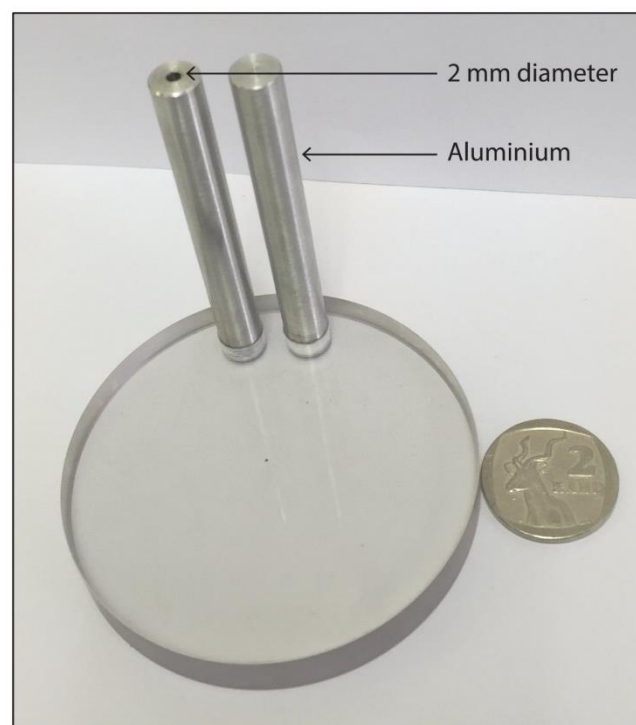
### 3.3. Scan Quality

Image quality may be directly assessed by the SNR, which also assists in determining optimal scanning parameters. The SNR was quantified for each incremental hematite thickness to obtain the average SNR for all X-ray energies (Fig. 4.4A). The quantified SNR for the 4mm thickness, before beam hardening correction was applied, indicates minimal variation between 100 and 180keV (Fig. 4.4B) compared to the corrected results. After the beam hardening correction was applied, the SNR shows a decrease from 100 to 140keV, with a small variation between 140 and 180keV (Fig. 4.4C). This suggests that there is no need for beam hardening correction for the 4mm thickness increment.

With increasing thickness increments, from 14 to 47mm, an increase in SNR was encountered, before beam hardening correction was applied, demonstrating



that X-ray penetration increases with increasing X-ray energy, but stabilises between 160 and 180keV, based on a small variation in SNR. Beam hardening correction produces similar SNR across all X-ray energies and from 14 to 47mm thickness increments. This suggests that the sample information to be quantified (in this case, porosity) for each of the stepped-wedge thicknesses should be evaluated the same or with minimum variation due to similar SNR. However, an overall decrease in SNR is observed as the stepped-wedge thicknesses increases and this would introduce errors when porosity information is quantified for the whole sample.



**Fig 4.3.** Aluminium standard sample with a 2mm pore diameter utilised to indirectly assess the impact of beam hardening artefacts for hematite and core samples.

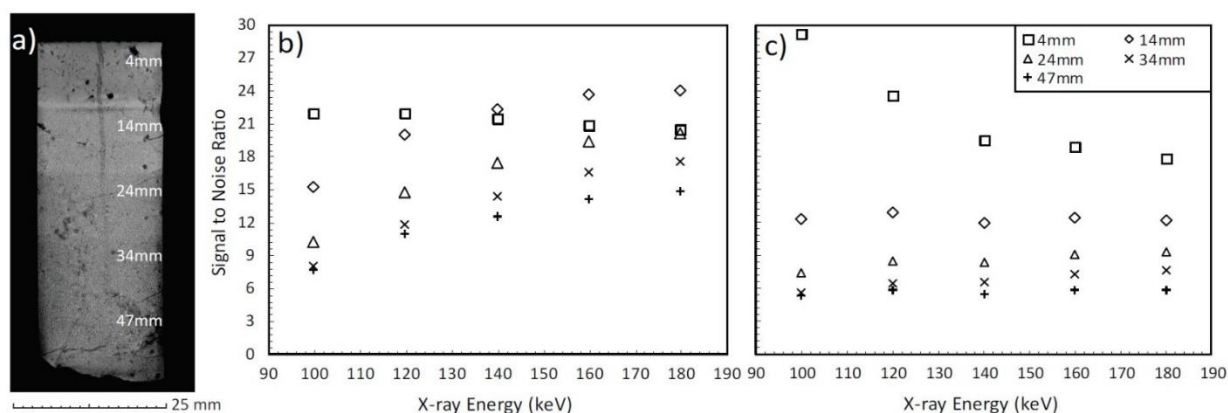


**Fig 4.4.** (a) Hematite stepped-wedge longitudinal image showing different thickness regions, (b) SNR of different thicknesses of the hematite stepped-wedge before and (c) after beam hardening correction was applied.

### 3.4. Line Profiles

The standard method to evaluate beam hardening is through line profiles across different sample thicknesses and by observing the behaviour of grey values of the single material/mineral which are expected to be similar. These grey values also represent the attenuation coefficient of the single material. Figures 4.5A to 4.5E shows line profiles of the 4, 14, 24, 34 and 47mm thickness increments before a beam hardening correction. There is a curved or non-linear increase in grey values, with increasing X-ray energy, between 100 and 180keV which means that the X-ray penetration has improved with increasing X-ray energy. However, an overlap of grey values is observed between 140 and 180keV, an effect that is

more pronounced from 14 to 47mm, between 100keV and 120keV, and between 140 and 180keV, before beam hardening correction. This indicates that an increase in beam hardening artefacts with increasing sample thickness increases the amount of noise within an image. After the beam hardening correction was applied (Fig. 4.5F-J), a horizontal line profile of the grey values was observed for the 4mm increment for all X-ray energies (Fig. 4.5F). Figures 4.5G to 4.5J show an overlap of grey values even after beam hardening correction, possibly implying that its application has limitations.

## 4. Results and discussion

### 4.1. Loss of Information Due to Beam Hardening

Beam hardening causes a variation in grey values, for the same material, due to variable X-ray attenuation: the extent of this is largely unknown because sample properties are initially unknown. This is circumvented by using phantom samples, with known properties, in the same scan, to indirectly evaluate beam hardening on the actual sample. Figure 4.6A shows a longitudinal image of the hematite stepped-wedge sample with the specularite vein. From Figure 4.1 it is evident that the specularite vein is pervasive; however, it is apparent from the XCT images of the same sample (Fig. 4.6A) that the vein is only observable from 4 to 24mm but, due to beam hardening, apparently disappears in increasingly thicker increments

### 4.2. Porosity Information

To further understand the effect of beam hardening, porosity information was quantified at different X-ray energies. Porosity information was derived from pore grey values within the 4mm increment to minimize errors that might result from thicker parts of the sample. In samples that are not affected by beam hardening the pore grey value is selected by using the average grey value of all the pores within the sample because they have a similar variation of grey values. The selection of the average pore grey value was guided by utilising the partial volume effect technique of the two component system (pore and hematite) that

represents a clear boundary between the two materials.

Figures 4.6B and 4.6C shows the quantified maximum pore volume within the specularite vein before and after beam hardening correction to demonstrate the loss of information. The vein was ring-fenced or isolated for each thickness increment, in order to evaluate the loss or decrease in pore volume for its maximum detectable pores. An increase in pore volume was observed with increasing thickness increments (Fig. 4.6B and 4.6C) and this does not represent the disappearance of the vein phenomena that is observed on Fig. 4.6A. This is one of the errors introduced by beam hardening because the disappearance of the vein suggests that the quantified maximum pore volume should decrease with increasing thickness increments. The disappearance of the vein also gives an indication of what happens to the low density minerals especially those that are represented by only a few pixels. Figures 4.6B and 4.6C also shows consistency of the quantified maximum pore volume within the 4mm thickness across all the X-ray energies as compared to 14 and 24mm thickness before and after beam hardening correction was applied. Porosity information also shows consistency within the 4mm thickness increment, with a maximum of 1.21% difference between no beam hardening and beam hardening-corrected images (Fig 4.7A and 4.7B), eliminating the need for such a correction. However, for 14, 24, 34 and 47mm thicknesses increments with a maximum percentage difference in porosity of 11.39%, 7.32%, 10% and 23.37% respectively, were observed.

## CHAPTER 4: Practical Evaluation of Beam Hardening

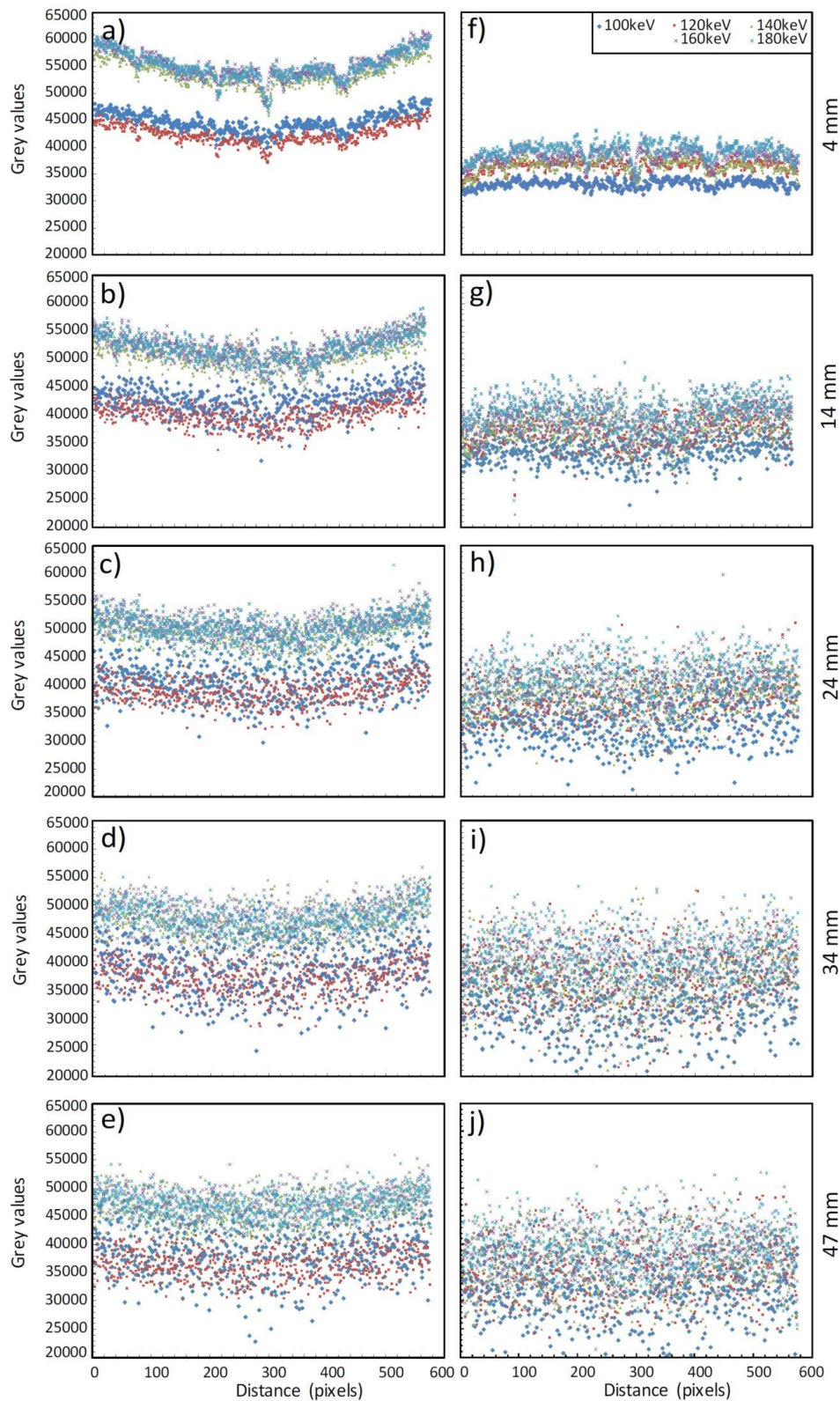


**Fig 4.5.** (a) to (e) show line profiles for different thickness increments of the hematite stepped-wedge before the beam hardening correction was applied, and (f) to (j) shows line profiles after beam hardening correction was applied.

#### 4.3. Beam Hardening Evaluation Method

Beam hardening was evaluated by positioning an aluminium standard sample, with an internal pore diameter of 2mm and surface area of 3.142mm<sup>2</sup>, behind the stepped-wedge sample (Fig. 4.8). The

protruding top part of the aluminium standard sample provided a standard reference. The selected average pore grey value for the protruding part of the aluminium is selected similarly to the average pore grey value of the 4mm thickness of the hematite stepped-wedge. The

## CHAPTER 4: Practical Evaluation of Beam Hardening

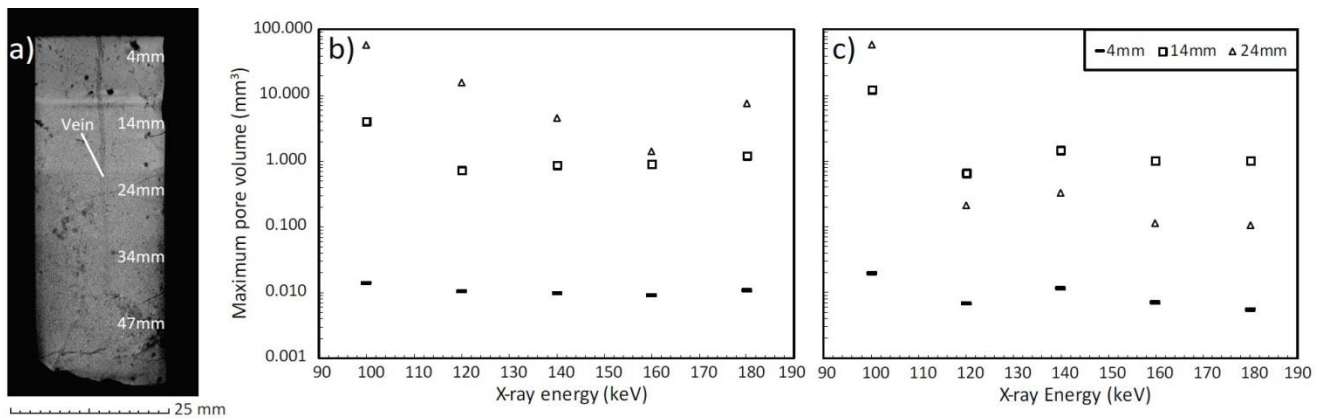


**Fig 4.6.** (a) Longitudinal image slice of the stepped-wedge showing the loss of information with increasing sample thickness, (b) The variation of quantified maximum pore volume of 4, 14 and 24mm thickness at different X-ray energies before beam hardening correction was applied, and (c) Quantified maximum pore volume after beam hardening correction was applied.

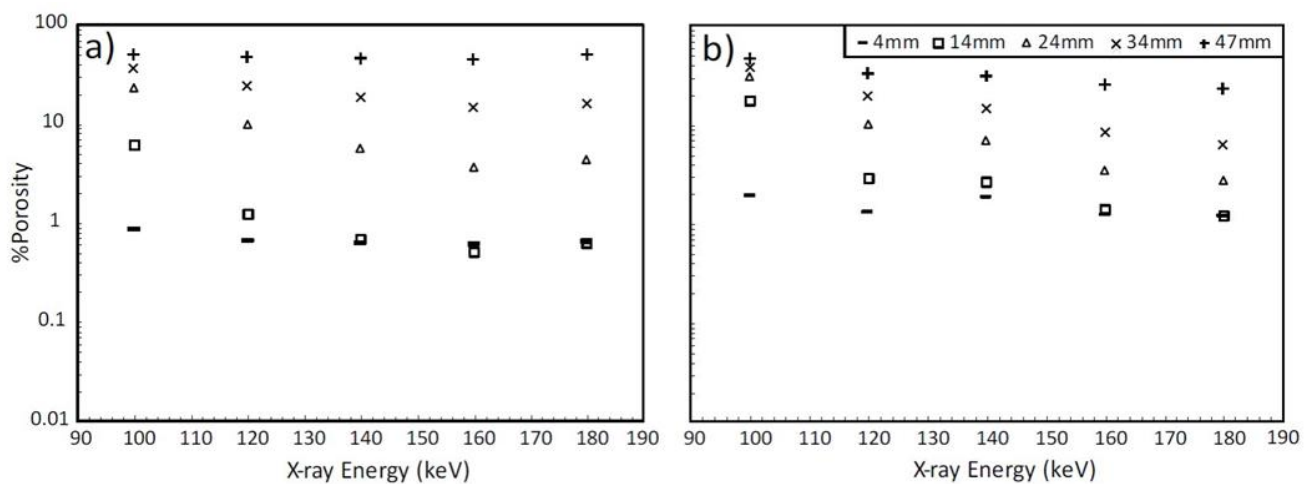


**Fig 4.7.** (a) Porosity information of different stepped-wedge thicknesses and different X-ray energies before the beam hardening correction was applied, and (b) Porosity information after the beam hardening correction was applied.

known internal surface area was compared to the calculated surface area in each image slice, for the region outside the hematite sample, and for each thickness increment of the stepped-wedge. To simplify the pore surface area measurements, the aluminium standard sample was cropped and isolated from the background as pore and background grey values are very similar. The beam hardening artefacts for each thickness was evaluated by means of error analysis (using the percentage error formula) to evaluate the quality of the scan of the hematite sample.

Figures 4.9A and 4.9B show the quantified pore surface area for each slice of the aluminium standard sample across each thickness increment of the hematite stepped-wedge sample, at different X-ray energies. The quantified pore surface area for the aluminium region outside of the stepped-wedge is repositioned to 0mm thickness for both Figs. 4.9A and 4.9B. The horizontal lines are positioned at 3.142 mm<sup>2</sup> to show the deviation of the expected pore surface area from the measured pore surface area. Only the pore surface area of the protruding portion of the aluminium standard sample and the 4mm thickness increment show good agreement, before and after beam hardening correction. From the 14 mm to 47mm

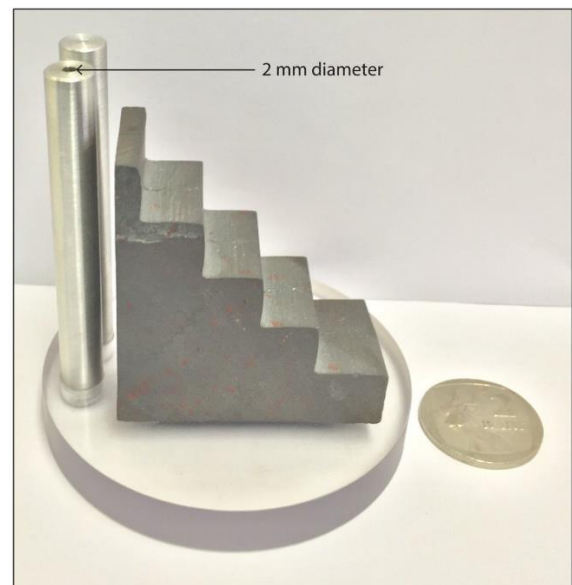


**Fig. 4.8.** Shows the positioning of the aluminium standard samples in order to indirectly evaluate the impact of beam hardening for each thickness.



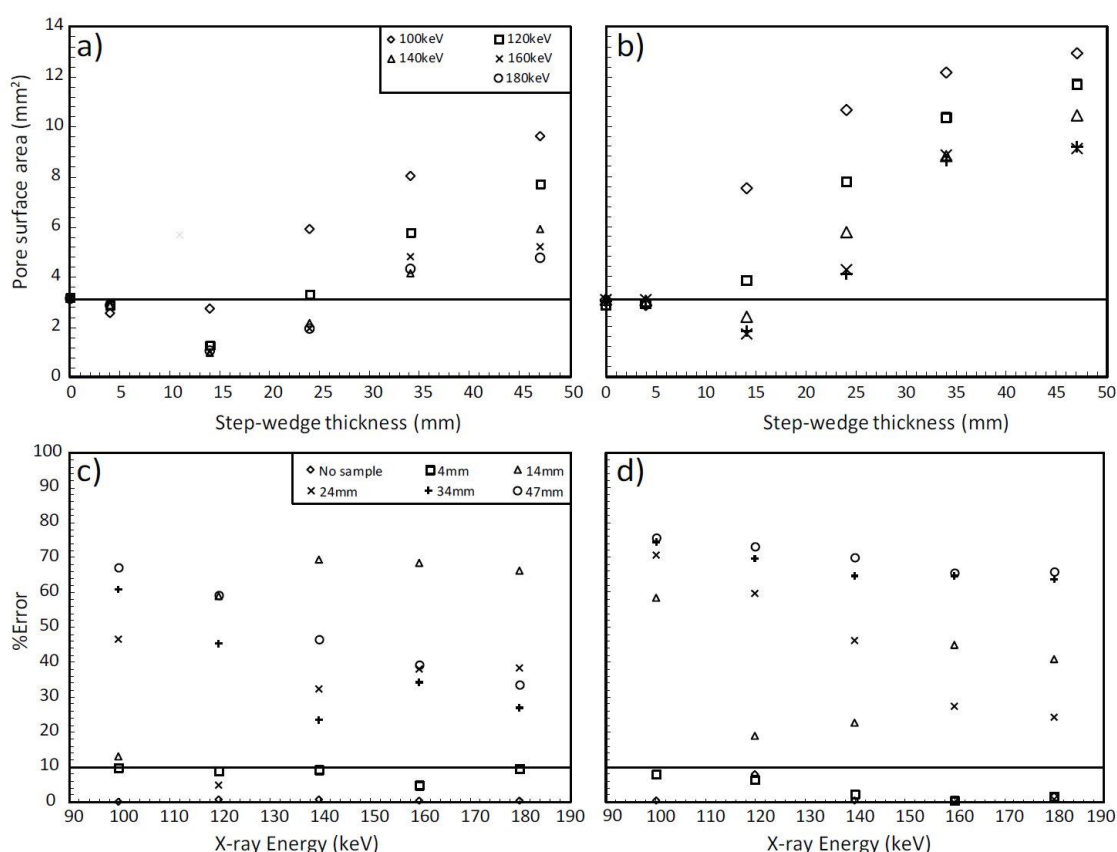


**Fig 4.9.** (a) and (b) Shows the calculated pore surface area of the aluminium standard sample before and after the beam hardening correction was applied, and (c) and (d) show the variation of the scan quality due to increasing sample thickness.

thickness increment there is an increase in calculated pore surface area, for each X-ray energy, both before and after beam hardening correction. The increase in pore surface area represents the amount of noise present due to progressive beam hardening with increasing thickness increments, causing deviation of calculated pore surface area from expected pore surface area. The comparison of calculated pore surface area with the expected one represents an indirect but practical way of evaluating the effect of beam hardening for each thickness of the hematite sample. It was observed that correlation between calculated and expected surface areas was optimal when the %Error was less than 10%, as shown on Figs. 4.9C and 4.9D. Any %Error greater than 10% results in inconsistent porosity information with larger percentage differences. This means that the quantified porosity and maximum pore volume between 14 and 47mm thickness increments cannot be used. This is due to %Error equal to or greater than 20%, and is reflected by diminishing pore information within the vein at 14 and 24mm thickness and complete loss of the vein information from 34 to 47mm thickness.

#### 4.4. The Application of the Aluminium Standard Sample to Different Sample Geometries

The effectiveness of the aluminium standard sample was further evaluated by scanning it together with different sample geometries (cylindrical, half cylinder and quarter cylinder) of apatite-magnetite ore. The aluminium standard sample was positioned along the thicker part of all the sample geometries to evaluate the impact of beam hardening with respect to

sample geometry or size. Based on results in Fig. 4.10 it is clear that the %Error decreases with decreasing sample size after beam hardening correction was applied as would be expected. The aluminium region outside all the samples was from 100 to 170 slice numbers and slice numbers greater than this represents the sample from top to bottom. For full and half cylinder samples the %Error is higher than 10% before and after beam hardening correction was applied. This means that the data does not contain enough information for further quantification of the volume size and shape of pores and low density minerals. It is only at 180keV for the half cylinder sample that different parts of the sample showed %Error less or equal to 10% after beam hardening correction was applied. This means that these sample regions can be extracted for further analysis. A significant improvement in %Error was observed for the quarter cylindrical sample with %Error less than 10% between 140 and 180keV before and after beam hardening correction was applied. The application of the aluminium standard sample demonstrated its effectiveness to determine regions of samples affected by beam hardening which means it can also be used to assess other dense sample types.

Due to the effectiveness and the easy application of the aluminium standard sample to determine if the sample is quantifiable it can be easily paired with the beam hardening correction method developed by Ketcham and Hanna (2014). This is an adaptive method that applies a variable correction based on the degree of beam hardening, although it requires

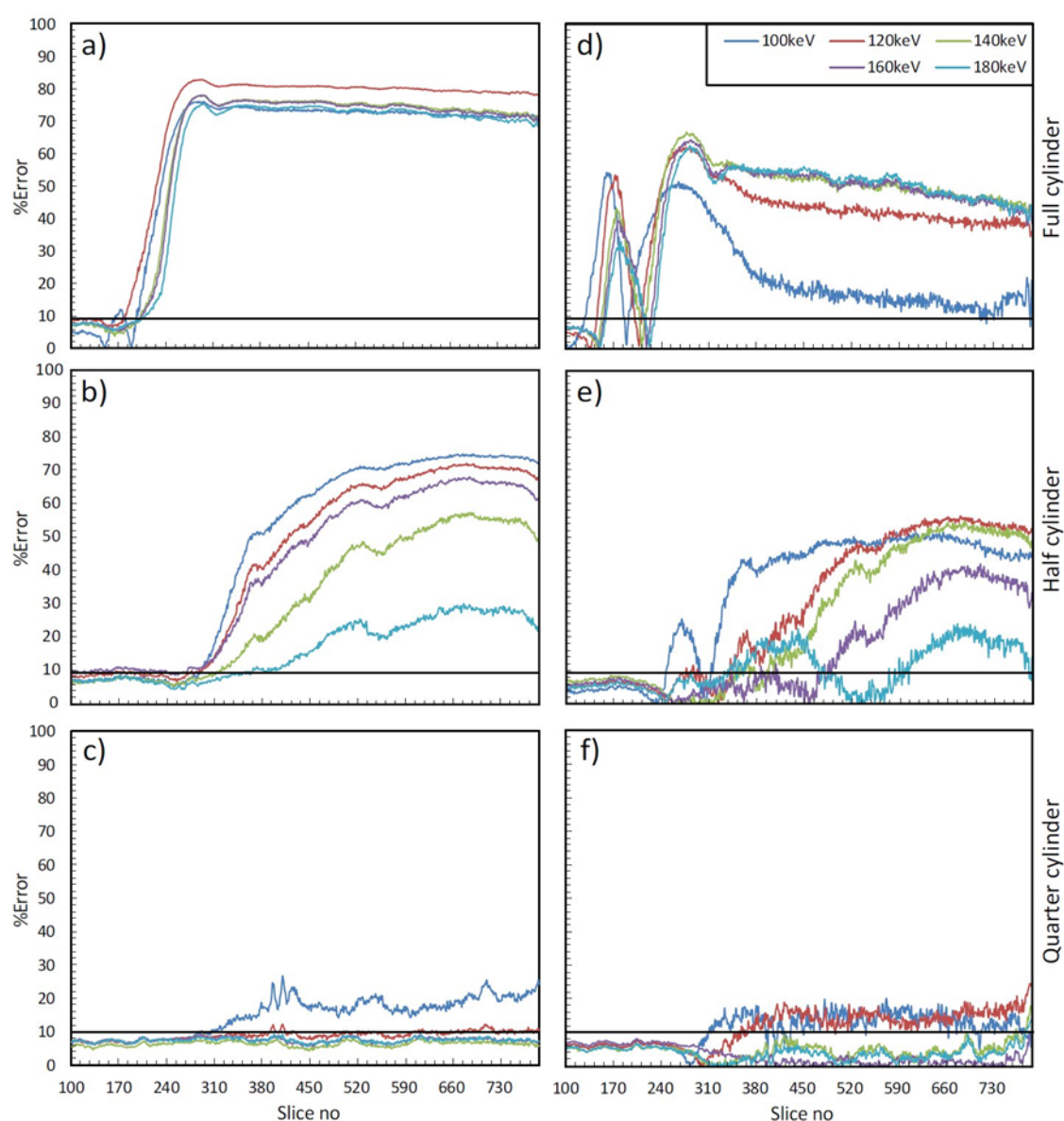


**Fig 4.10.** (a) to (f) Shows the scan qualities of full, half and quarter cylinder of the apatite-magnetite sample before and after beam hardening correction was applied.

an experienced instrument scientist to identify sample areas that are affected by beam hardening. The main advantage of this method is that it allows for quantification of the %Error providing a clear indication of the degree of beam hardening throughout the sample. The %Error greater than 10% is an indication that beam hardening artefacts exist and the correction of this adaptive method can be applied such that the %Error is less than 10%.

## 5. Conclusions

Beam hardening artefacts remain a significant problem in the scanning of high density samples by XCT. This is compounded when the full extent of information loss as a result of beam hardening is unknown, particularly when scanning high density and complex ore samples. This paper presented a methodology to indirectly determine the impact of beam hardening on sample information loss by utilising a specially manufactured cylindrical aluminium standard sample. The quantification of the %Error (a measure of the loss of information) was correlated with

the hematite stepped-wedge sample to determine the sample thickness that results in loss of sample information (porosity and mineralogy). The key steps of the method are: (i) Scan the dense sample together with an aluminium cylindrical sample that has an internal, single pore, (ii) Scan the sample at different X-ray energies to determine the optimal X-ray energy for scanning and determine the impact of beam hardening and consistency of sample information (porosity in this case), (iii) Quantify the pore surface area of the aluminium standard sample to determine the deviation between calculated pore surface area from expected pore surface area, and (iv) Calculate and utilise the %Error to determine the degree of beam hardening on sample information. A %Error greater than 10% results in inconsistent sample information that cannot be compared at different X-ray energies, indicating loss of sample information. A %Error greater than 20% indicates substantial loss of sample information due to the presence of stronger beam hardening artefacts.

With this approach an optimal sample size for dense ore samples was determined and found to be associated with the quarter sample because it is the

smallest sample compared to the full and half ore size. The half cylinder sample also had sample regions that had %Error less than 10% at 180keV after a beam hardening correction was applied, which means that those regions can be isolated and used for further analysis. Although a circular geometry is often assumed to give the best results, this is actually only valid if the circular geometry is monomineralic. The results of this study indicate that it is the absolute size of the sample that is critical and not necessarily the geometry of the sample since the quarter-core gave acceptable %Error values. The evaluation of %Error as a function of sample size therefore provides in-depth information with respect to the degree of beam hardening. The utilisation of an aluminium standard for beam hardening evaluation is practical, easily applicable and effective. This method can also be used to evaluate the effectiveness of different beam hardening correction methods to correct grey value variation in different high density ores and test the ability of these methods to recover the lost information by using the %Error as a guideline.

## 6. Acknowledgements

The authors would like to thank Necsa (Nuclear Energy Corporation of South Africa) and the management team for funding and access to the Microfocus system in the MIXRAD Lab, which is a DST-NRF (Department of Science and Technology – National Research Funding) funded facility through the NEP-RISP (National Equipment Programme – Research Infrastructure Support Programmes) program [Grant No: UID72310]. The authors would also like to thank Andrew Watson for his contribution on compiling the diagrams. The work was supported by the SAMMRI (South African Minerals to Metals Research Institute) [Grant No.: S1511]. Any opinions, findings and conclusions or recommendations expressed in any publication generated by the NRF and SAMMRI supported research is that of the author(s), and that the NRF and SAMMRI accepts no liability whatsoever in this regard.

## 7. References

- Ay, M.R., Mehranian, A., Maleki, A., Ghadiri, H., Ghafarian, P., Zaidi, H., 2013. Experimental assessment of the influence of beam hardening filters on image quality and patient dose in volumetric 64-slice X-ray CT scanners. *Phys. Medica* 29, 249–260. <https://doi.org/10.1016/j.ejmp.2012.03.005>
- Bam, L.C., Miller, J.A., Becker, M., Beer, F.C. De, Basson, I., 2016. X-ray Computed Tomography – Determination of Rapid Scanning Parameters for Geometallurgical Analysis of Iron Ore, in: *Proceedings of the 3rd International Geometallurgy Conference*. Perth, pp. 209–219.
- Boas, F.E., Fleischmann, D., 2012. CT artifacts : Causes and reduction techniques. *Imaging Med* 4, 229–240.
- Charikinya, E., Bradshaw, S., Becker, M., 2015. Characterising and quantifying microwave induced damage in coarse sphalerite ore particles. *Miner. Eng.* 82, 14–24. <https://doi.org/10.1016/J.MINENG.2015.07.020>
- Clout, J.M.F., Manuel, J.R., 2015. Mineralogical, chemical, and physical characteristics of iron ore, in: *Iron Ore: Mineralogy, Processing and Environmental Sustainability*. Elsevier, pp. 45–84. <https://doi.org/10.1016/B978-1-78242-156-6.00002-2>
- Cnudde, V., Boone, M.N., 2013. High-resolution X-ray computed tomography in geosciences: a review of the current technology and applications. *Earth Sci. Rev.* 123, 1–17. <https://doi.org/10.1016/j.earscirev.2013.04.003>
- Davis, G.R., Elliott, J.C., 2006. Artefacts in X-ray microtomography of materials. *Mater. Sci. Technol.* 22. <https://doi.org/10.1179/174328406X114117>
- Dhawan, N., Safarzadeh, M.S., Miller, J.D., Moats, M.S., Rajamani, R.K., Lin, C.-L., 2012. Recent advances in the application of X-ray computed tomography in the analysis of heap leaching systems. *Miner. Eng.* 35, 75–86. <https://doi.org/10.1016/J.MINENG.2012.03.033>
- Donskoi, E., Poliakov, A., Holmes, R., Suthers, S., Ware, N., Manuel, J., Clout, J., 2016. Iron ore textural information is the key for prediction of downstream process performance. *Miner. Eng.* 86, 10–23. <https://doi.org/10.1016/J.MINENG.2015.11.009>
- Evans, C.L., Morrison, R.D., 2016. Mineral liberation, in: Megan Becker, Elaine Wightman, Cathy Evans (Eds.), *Process Mineralogy*. Julius Kruttschnitt Mineral Research Centre, Brisbane, Australia, pp. 219–233.
- Evans, C.L., Wightman, E.M., Yuan, X., 2015. Quantifying mineral grain size distributions for process modelling using X-ray micro-tomography. *Miner. Eng.* 82, 78–83. <https://doi.org/10.1016/J.MINENG.2015.03.026>
- Fagan-Endres, M.A., Cilliers, J.J., Sederman, A.J., Harrison, S.T.L., 2017. Spatial variations in leaching of a low-grade, low-porosity chalcopyrite ore identified using X-ray  $\mu$ CT. *Miner. Eng.* 105, 63–68. <https://doi.org/10.1016/J.MINENG.2017.01.010>
- Garcia, D., Lin, C.L., Miller, J.D., 2009. Quantitative analysis of grain boundary fracture in the breakage of single multiphase particles using X-ray microtomography procedures. *Miner. Eng.* 22, 236–243. <https://doi.org/10.1016/J.MINENG.2008.07.005>
- Ghorbani, Y., Becker, M., Petersen, J., Morar, S.H., Mainza, A., Franzidis, J.-P., 2011. Use of X-ray computed tomography to investigate crack distribution and mineral dissemination in sphalerite ore particles. *Miner. Eng.* 24, 1249–1257. <https://doi.org/10.1016/J.MINENG.2011.04.008>
- Hoffman, J.W., de Beer, F.C., 2012. Characteristics of the Micro-Focus X-ray Tomography Facility ( MIXRAD ) at Necsa in South Africa, in: *18th World Conference on Nondestructive Testing*. pp. 1–12.
- Jaju, P.P., Jain, M., Singh, A., Gupta, A., 2013. Artefacts in cone beam CT. *Open J. Stomatol.* 03, 292–297. <https://doi.org/10.4236/ojst.2013.35049>
- Jardine, M.A., Miller, J.A., Becker, M., 2018. Coupled X-ray computed tomography and grey level co-occurrence matrices as a method for quantification of mineralogy and texture in 3D. *Comput. Geosci.* 111, 105–117. <https://doi.org/10.1016/J.CAGEO.2017.11.005>
- Ketcham, R.A., Carlson, W.D., 2001. Acquisition , optimization and interpretation of X-ray computed tomographic imagery : applications to the geosciences. *Comput. Geosci.* 27, 381–400.



## CHAPTER 4: Practical Evaluation of Beam Hardening

- Ketcham, R.A., Hanna, R.D., 2014. Beam hardening correction for X-ray computed tomography of heterogeneous natural materials. *Comput. Geosci.* 67, 49–61. <https://doi.org/10.1016/j.cageo.2014.03.003>
- Koeberl, C., 2002. High-resolution X-ray computed tomography of impactites. *J. Geophys. Res.* 107, 1–9. <https://doi.org/10.1029/2001JE001833>
- Kraemer, A., Kovacheva, E., Lanza, G., 2015. Projection based evaluation of CT image quality in dimensional metrology, in: *Digital Industrial Radiology and Computed Tomography*. pp. 1–10.
- Lin, C.L., Miller, J.D., Nguyen, T., Nguyen, A., 2017a. Characterization of Breakage and Washability of ROM Coal using X-ray Computed Tomography. *Int. J. Coal Prep. Util.* 1–14. <https://doi.org/10.1080/19392699.2017.1305364>
- Lin, C.L., Miller, J.D., Nguyen, T., Nguyen, A., 2017b. Characterization of Breakage and Washability of ROM Coal using X-ray Computed Tomography. *Int. J. Coal Prep. Util.* 1–14. <https://doi.org/10.1080/19392699.2017.1305364>
- Louis, L., Wong, T. fong, Baud, P., Tembe, S., 2006. Imaging strain localization by X-ray computed tomography: discrete compaction bands in Diemelstadt sandstone. *J. Struct. Geol.* 28, 762–775. <https://doi.org/10.1016/j.jsg.2006.02.006>
- Lund, C., 2013. Mineralogical, Chemical and Textural Characterisation of the Malmberget Iron Ore Deposit for a Geometallurgical Model. Luleå University of Technology.
- Mees, F., Swennen, R., Van Geet, M., Jacobs, P., 2003. Applications of X-ray Computed Tomography in the Geosciences, 215th ed. The Geological Society London, London,.
- Meganck, J.A., Kozloff, K.M., Thornton, M.M., Broski, S.M., Goldstein, S.A., 2009. Beam hardening artifacts in micro-computed tomography scanning can be reduced by X-ray beam filtration and the resulting images can be used to accurately measure BMD. *Bone* 45, 1104–1116. <https://doi.org/10.1016/j.bone.2009.07.078>
- Miller, J.D., Lin, C.-L., Hupka, L., Al-Wakeel, M.I., 2009. Liberation-limited grade/recovery curves from X-ray micro CT analysis of feed material for the evaluation of separation efficiency. *Int. J. Miner. Process.* 93, 48–53. <https://doi.org/10.1016/J.MINPRO.2009.05.009>
- Mouton, A., Megherbi, N., 2013. An experimental survey of metal artefact reduction in computed tomography. *J. Xray. Sci. Technol.* 21, 193–226. <https://doi.org/10.3233/XST-130372>
- Park, H.S., Chung, Y.E., Seo, J.K., 2015. Computed tomographic beam-hardening artefacts: mathematical characterization and analysis. *PhilosTrans A Math Phys Eng Sci* 373, 1–11. <https://doi.org/10.1098/rsta.2014.0388>
- Park, H.S., Gao, H., Lee, S.M., Seo, J.K., 2016. Towards Beam Hardening Correction for Polychromatic X-ray CT. *J. Comput. Math.* 34, 671–682. <https://doi.org/10.4208/jcm.1607-m2016-0531>
- Schulze, R., Heil, U., Groß, D., Bruellmann, D.D., Dranschnikow, E., Schwanecke, U., Schoemer, E., 2011. Artefacts in CBCT: A review. *Dentomaxillofacial Radiol.* 40, 265–273. <https://doi.org/10.1259/dmfr/30642039>
- Siewerdsen, J.H., Daly, M.J., Bakhtiar, B., Moseley, D.J., Richard, S., Keller, H., Jaffray, D. a, 2006. A simple, direct method for x-ray scatter estimation and correction in digital radiography and cone-beam CT. *Med. Phys.* 33, 187–197. <https://doi.org/10.1118/1.2148916>
- Spencer, S., Sutherland, D., 2000. STEREOLOGICAL CORRECTION OF MINERAL LIBERATION GRADE DISTRIBUTIONS ESTIMATED BY SINGLE SECTIONING OF PARTICLES. *Image Anal Stereol Orig. Res. Pap.* 19, 175–182.
- Stowe, J.G., Curran, K.M., 2016. Suppression of the CT Beam Hardening Streak Artifact Using Predictive Correction on Detector Data. *Univers. J. Med. Sci.* 4, 69–80. <https://doi.org/10.13189/ujmsj.2016.040203>
- Van de Casteele, E., 2004. Model-based approach for Beam Hardening Correction and Resolution Measurements in Microtomography. Universiteit Antwerpen.
- Wang, Y., Lin, C.L., Miller, J.D., 2015. Improved 3D image segmentation for X-ray tomographic analysis of packed particle beds. *Miner. Eng.* 83, 185–191. <https://doi.org/10.1016/J.MINENG.2015.09.007>
- Wildenschild, D., Hopmans, J.W., Vaz, C.M.P., Rivers, M.L., Rikard, D., Christensen, B.S.B., 2002. Using X-ray computed tomography in hydrology : systems , resolutions , and limitations. *J. Hydrol.* 267, 285–297.
- Wildenschild, D., Sheppard, A.P., 2013. X-ray imaging and analysis techniques for quantifying pore-scale structure and processes in subsurface porous medium systems. *Adv. Water Resour.* 51, 217–246. <https://doi.org/10.1016/j.advwatres.2012.07.018>
- Yang, B.H., Wu, A.X., Miao, X.X., Liu, J.Z., 2014. 3D characterization and analysis of pore structure of packed ore particle beds based on computed tomography images. *Trans. Nonferrous Met. Soc. China (English Ed.)* 24, 833–838. [https://doi.org/10.1016/S1003-6326\(14\)63131-9](https://doi.org/10.1016/S1003-6326(14)63131-9)

## CHAPTER 4: Practical Evaluation of Beam Hardening

**Supplementary Notes on Beam Hardening**

These supplementary notes have been added to provide better context about the impact of beam hardening on highly attenuating samples. The filter materials were applied to minimise the impact of beam hardening. Thereafter, the signal-to-noise ratio, line profiles, porosity information and %Error were evaluated to further understand the impact of beam hardening

*Application of Filter Materials*

To minimise the impact of beam hardening in this case a combination of 1mm aluminium + 1mm copper filters were used.

*Signal-To-Noise Ratio*

The signal-to-noise ratio (SNR) describes the detectability or quality of the grey values to represent a mineral using the ratio between the mean grey value (signal) and standard deviation (noise). The SNR was measured on each thickness of the hematite stepped-wedge sample (4 mm, 14 mm, 24 mm, 34 mm and 47 mm). The stepped-wedge sample was scanned at different X-ray energy spectrums (Figure 4.1). This was done to determine the quality of the scans for each X-ray energy spectrum by using the SNR. The SNR was determined by selecting a region of interest (ROI) on the hematite region away from the pores in order to evaluate regions of the sample with the highest concentration of hematite to better understand the impact of beam hardening. As expected the SNR was the highest for the 4mm thickness of the sample across all the X-ray energies after beam hardening correction factor was applied, Figure 4.4c.

*Line Profile*

Even though the SNR was high for the 4mm thickness of the stepped-wedge as compared to other thicknesses the impact of beam hardening is still unknown. To further understand this artefact the line profiles were constructed across each thickness of the hematite stepped-wedge. The line profiles were compared before and after the beam hardening correction was applied, Figure 4.5. The line profiles for the 4mm thickness of the stepped-wedge show pronounced beam hardening as demonstrated by the curved line profiles or rather a larger variation of grey values (Figure 4.5a). However, after the impact of beam hardening was corrected, horizontal line profiles were obtained. This indicates that the grey values for the 4mm hematite stepped-wedge were corrected as expected (Figure 4.5f). But for thicknesses above 4mm the line profiles demonstrated the complex nature of beam hardening which was shown by grey value overlap of the line profiles for all the thicknesses and X-ray energy spectrums. It is important to note that the grey values for each line profiles were not calibrated to represent the linear attenuation coefficient of hematite for each X-ray energy spectrum but rather observe how the impact of beam hardening affects each thickness of the hematite stepped-wedge.

*Specularite Vein*

Although specularite has the same sample properties as hematite on an XCT image, the specularite vein appears differently on the images. This is due to the porous nature of the specularite. Analysis of Figure 4.4a shows that specularite grains have the same grey values as hematite. To further demonstrate the complexity of beam hardening, Figure 4.4a show a vertical cut-through slice that demonstrate clearly how each thickness is affected by the impact of beam hardening. The impact of beam hardening is well illustrated by the disappearing specularite vein and the

## CHAPTER 4: Practical Evaluation of Beam Hardening

decreasing SNR as the thickness of the hematite stepped-wedge increases even after beam hardening is corrected (Figure 4.4a and c). However, this is not a true reflection of the sample information because the specularite vein bisects the whole sample. Additional images are provided below to demonstrate that the specularite vein does in fact cut continuously through the entire sample (Figure 4.A).

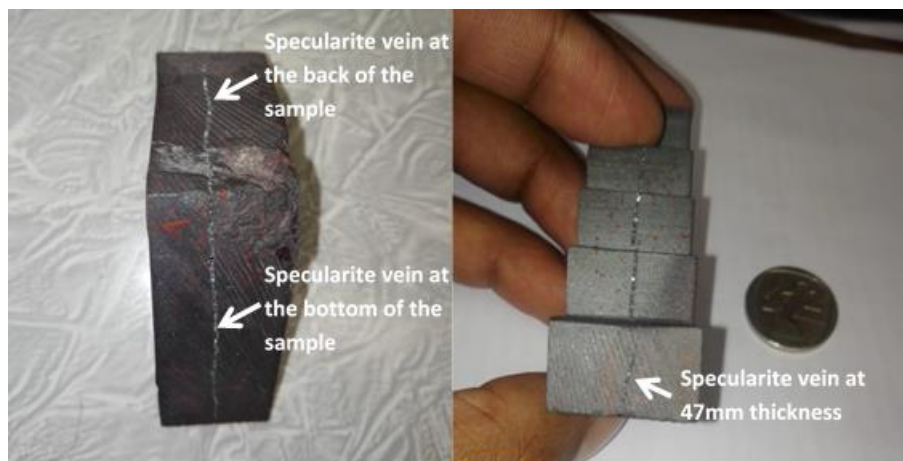


**Fig 4.A.** Stepped-wedge sample cut from a natural piece of hematite ore with a specularite vein bisecting the entire sample

#### *Quantification of Pore Volume and %Porosity Information*

Beam hardening can affect the quantification of sample information. This is demonstrated by quantifying the maximum pore volume and %porosity information within the stepped-wedge sample. The only reliable and consistent quantified maximum pore volume was of the 4mm thickness of the stepped-wedge across all the X-ray energy spectrums (Figure 4.6b and c). The quantified %porosity information found to be in good agreement and consistent was also for the 4mm thickness of the stepped-wedge sample (Figure 4.7a,b). The thicker parts of the stepped-wedge showed inconsistent porosity information which made it impossible to determine the true porosity information of the sample.

#### *Utilisation of Aluminium Standard Sample*

The aluminium standard sample was used to determine the %Error that corresponded with a loss of sample information. To do this, the standard sample was placed behind the longest path of the stepped-wedge sample because the X-ray beam experiences more beam hardening as it passes through the sample. The aluminium standard sample had a 2 mm diameter pore with a cross-sectional area (referred to as the pore surface area) of  $3.142\text{mm}^2$ . The pore surface area was then quantified on the scanned aluminium cylindrical sample for each 2D image slice covering the length of the hematite stepped-wedge to be compared against the physically measured pore area of  $3.142\text{mm}^2$  in order to quantify %Error as described in section 4.3 of this manuscript.

#### *Quantification of the %Error*

The %Error is defined as a comparison between the measured or quantified pore surface area of an aluminium cylindrical sample within the images against the expected pore surface area of  $3.142\text{mm}^2$ . The quantified pore surface area showed good agreement with the expected pore surface area of  $3.142\text{mm}^2$  within the 4mm thickness of the stepped-wedge (Figure 4.9a and b). Beyond this thickness of the stepped-wedge, the quantified pore surface areas deviated largely from the expected pore surface area of  $3.142\text{mm}^2$ . This demonstrates the impact and the degree of beam hardening on each thickness of the stepped-wedge that translated to a loss of sample information. This was

## CHAPTER 4: Practical Evaluation of Beam Hardening

indicated by %Error values larger than 10%. The large variation of the %Error suggest that each thickness of the stepped-wedge requires a different mean grey value in order to quantify the porosity information. However, when quantifying porosity information in real samples only a single grey value is selected without knowing how much it overlaps with the grey values of other phases. This is demonstrated by Figure 4.6b and c where unreliable maximum pore volumes were found to be associated with the thicker parts of the stepped-wedge (above 4mm) due to mean grey value of the pores overlapping with hematite grey values. Recognition of this problem could only be achieved or observed by using the %Error approach as shown in Figure 4.9c and d.

## CHAPTER 5: Dual Energy

---

**PAPER PUBLICATION HISTORY**

---

<b>Title</b>	Application of a Simplified Dual Energy X-Ray Computed Tomography Method for Analysis of High-Density Ore Samples
<b>Journal</b>	
<b>Status</b>	To be Submitted February 2020
<b>Authors and roles</b>	L C Bam – PhD Candidate J A Miller – Primary Supervisor M Becker – Secondary Supervisor
<b>Applicant Contribution</b>	Lunga Bam - Conceptualization, Formal analysis, Methodology, Writing—original draft & editing (90%).

---

# Application of a Simplified Dual Energy X-Ray Computed Tomography Method for Analysis of High Density Ore Samples

L Bam<sup>a,c</sup>, M Becker<sup>b</sup>, J Miller<sup>a</sup>

- a. Department of Earth Sciences, Stellenbosch University, Private Bag X1, Matieland 7601, South Africa. Email: [lunga.bam@necsa.co.za](mailto:lunga.bam@necsa.co.za); [jmiller@sun.ac.za](mailto:jmiller@sun.ac.za)  
 b. Centre for Minerals Research, Department of Chemical Engineering, University of Cape Town, Private Bag, Rondebosch 7701, South Africa. Email: [megan.becker@uct.ac.za](mailto:megan.becker@uct.ac.za)  
 c. Department Radiation Science, Necsa, PO Box 582, Pretoria, South Africa. Email: [lunga.bam@necsa.co.za](mailto:lunga.bam@necsa.co.za)

## ARTICLE INFO

### Keywords:

Dual energy,  
Attenuation coefficient,  
Chalcopyrite,  
Pyrite,  
Effective energy

## ABSTRACT

The discrimination between minerals with similar linear attenuation coefficients is challenging when using X-ray computed tomography. This challenge is even more pronounced when dealing with samples that are associated with beam hardening. Beam hardening changes the grey value ratio and distribution between minerals that is supposed to represent the theoretical linear attenuation coefficient of minerals in an image. With the utilization of the dual energy subtraction method the discrimination between minerals with similar linear attenuation coefficient becomes possible. This method also requires that the sample should not be highly affected by beam hardening in order to maintain the grey value difference that represents the theoretical linear attenuation coefficient difference to optimize the discrimination between e.g. chalcopyrite and pyrite. In high density ores the method is limited because the grey value difference between chalcopyrite and pyrite is affected. This study presents a simplified dual energy method that uses a combination of the scanned data at lower X-ray energy together with a simulated image to improve the discrimination between chalcopyrite and pyrite in cases where the sample is affected by beam hardening. The method also minimizes the errors associated with the X-ray source that result in edge artefacts when using the traditional dual energy subtraction method.

## 1. Introduction

The ability of conventional single-energy X-Ray computed tomography (XCT) to differentiate individual minerals is based on these minerals having a sufficient difference in X-ray attenuation that they manifest as different grey values (Aran et al., 2014). In a normal XCT (XCT systems with X-ray energy spectrum ~ 200keV), the total attenuation is a combination of the photo-electric effect and Compton scattering interactions. The relative contribution of these interactions to the total attenuation is energy dependent and a function of the atomic number and density of the materials involved (Aran et al., 2014; Rebuffel and Dinten, 2006). For minerals with similar densities and linear attenuation coefficients, single energy XCT will struggle to differentiate these minerals (Fessler et al., 2002). This is due to the fact that single-energy XCT scanning provides quantitative information based on linear attenuation coefficient of the closely related minerals even if there is a difference in effective atomic numbers between the minerals (Ilovea et al., 2006). However, dual energy is able to discriminate minerals or structures with similar densities but different elemental compositions based

on their atomic number and density (Aran et al., 2014; Rebuffel and Dinten, 2006).

The dual energy method uses two X-ray energy spectrums at both low and high X-ray energy spectrum (Forghani et al., 2017; Foust et al., 2018; Noguchi et al., 2017; Obaid et al., 2014; Stenner et al., 2007; Taguchi et al., 2018). The technique requires that the two X-ray energy spectrum measurements be acquired in identical geometry in order to allow their numerical combination (Rebuffel and Dinten, 2006). The method can be implemented in either dual or single exposure depending on the system design. The dual exposure technique is the most common in a normal XCT laboratory. The single exposure technique uses two detectors separated by an intermediate filter and the front detector records the low energy photons whereas the one at the back records high energy ones (Rebuffel and Dinten, 2006). In contrast, the dual exposure technique acquires two images successively using voltage tuning associated with the use of filters placed behind the generator. This method is efficient in terms of energy separation but assumes that the object is static and it is implemented using 2D detectors. The disadvantage of using 2D detectors is



## CHAPTER 5: Dual Energy

that they are affected by scattered X-ray beams that affects the accuracy of the detected X-ray beam.

The dual energy technique has shown promise for various applications including rock characterization for petro-chemical industrial applications (Wellington and Vinegar, 1987), soil sample analysis in agriculture (Cruvinel and Balogun, 2000), explosives detection (Roder, 1979), and radioactive waste characterization (Robert-Coutant et al., 1999). However, when considering a specific problem the dual energy technique may or may not be applicable depending on the complexity of the problem (Rebuffel and Dinten, 2006). Considering its successful applications in the various fields mentioned above, the dual energy technique has the potential to characterize and discriminate minerals with similar densities for minerals processing purposes. Some of the minerals of interest occur within the more dense ores which induces beam hardening due to the polychromatic nature of the X-ray energy spectrum of most lab based systems. This artefact therefore leads to reconstructed volumes with distorted attenuation coefficients of the minerals of interest that limits the application of the XCT lab-based systems using single X-ray energy spectrum. The most common approach to minimize beam hardening is through a mathematical correction or a more simpler approach, with the use of a physical correction (Ilovea et al., 2006). There are various other ways to correct for beam hardening artefact as summarized in Bam et al. (2019). However, it has been shown that the high impact of beam hardening can lead to a loss of sample information when scanning high density ores which affects the true representation of the sample properties (Bam et al., 2019) and this can affect dual energy results.

This study proposes a new and simplified dual energy method that discriminates high density phases with similar attenuation coefficients. The method takes advantage of a smaller difference in attenuation coefficients at the lower X-ray energy spectrum to obtain the scanned information, and a similarity in attenuation coefficient at a higher X-ray energy spectrum to obtain a simulated image. This optimizes the applicability of the dual energy method to dense

samples affected by beam hardening. The proposed method (1) incorporates calibration samples for data validation and to improve the accuracy of the quantified information, and (2) eliminates unwanted errors associated with the X-ray source that uses a filament to generate X-ray energy spectrums. The proposed method is based on the dual energy subtraction technique that involves subtraction of two volumes scanned at different X-ray energies. The method simulates one scanning condition and the other condition is obtained by conducting a real scan so that mineralogical information can be obtained in 3D. The use of a simulated image provides faster scan turnaround times thereby addressing the timing issue that has been a problem for conventional dual energy methods (Fessler et al., 2002). The application of the method is demonstrated for the discrimination of chalcopyrite from pyrite, two minerals that have traditionally been difficult to differentiate using single-energy XCT scanning.

## 2. Methodology

The simplified dual energy method relies on two scanning conditions: a) where there is a small discrimination in linear attenuation coefficient between two minerals at a lower X-ray energy spectrum; and b) where there is an overlap in linear attenuation coefficient at a higher X-ray energy spectrum. An overlap in the linear attenuation coefficient allows the minerals to be simulated in an image with the same grey value because they share the same linear attenuation coefficient.

### 2.1. Simplified Dual Energy Method

The simplified dual energy method relies on prior mineralogical information (density and chemical composition) in order to calculate the different linear attenuation coefficients of the minerals present within a sample (see chapter 2). This optimizes the sample information by selecting X-ray energies where there is a slight discrimination in the linear attenuation coefficient between minerals that share similar densities.

## CHAPTER 5: Dual Energy

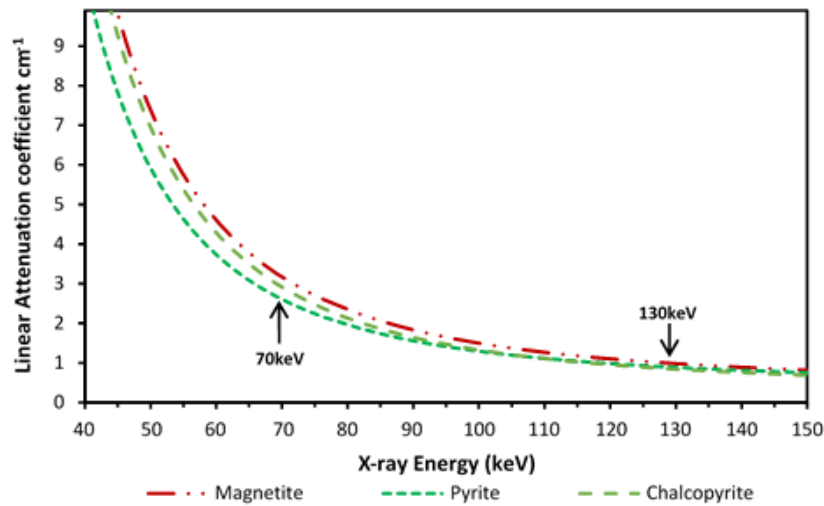


**Fig 5.1.** The linear attenuation coefficient distribution with increasing X-ray energy of chalcopyrite, pyrite and magnetite.

#### 2.1.1. Linear Attenuation Coefficient of Minerals

Most mineralogical information can be easily discriminated in terms of linear attenuation coefficients at a lower X-ray energy range due to the photoelectric effect interaction dominating at X-ray energies between 50 – 100keV (Ketcham and Carlson, 2001). However, these X-ray energies are usually associated with many image artefacts including noise and beam hardening which makes it difficult to conduct scans especially for high density samples. The linear attenuation coefficient of pyrite and chalcopyrite converges with increasing X-ray energy until around 130keV and diverges with decreasing X-ray energy (Fig. 5.1). The proposed simplified dual energy method takes advantage of the similar attenuation coefficients of pyrite and chalcopyrite at 130keV. The minimum optimal X-ray energy is selected at 70keV because there is a small discrimination between pyrite and chalcopyrite. To optimize the discrimination between chalcopyrite and pyrite using the dual energy method, the second X-ray energy is selected at 130keV due to an overlap in the linear attenuation coefficient between the two minerals. This means the subtraction of the 130keV scan from 70keV scan will result in an optimized discrimination of chalcopyrite from pyrite because the contribution of pyrite linear attenuation coefficient will be removed from the resultant scan or image slice. However, the set voltages on the XCT system would be 70kV and 130kV which produces X-ray energy spectrums with effective X-ray energies of 45.5keV and 61.3keV respectively (see chapter 2). The effective X-ray energy represents a monochromatic X-ray energy similar to that of the total energy spectrum. This effective X-ray energy is used to calculate the linear attenuation coefficient of a mineral as per chapter 2. The calculated linear attenuation coefficient does not take into consideration the impact of beam hardening due to high density nature of the minerals and the utilisation of a filter material.

#### 2.1.2. The Generation of the Simulated Image

The generation of a simulated image relies on the overlap in linear attenuation coefficient between chalcopyrite and pyrite

## CHAPTER 5: Dual Energy

at 130keV. This means the grey values of the two minerals will be similar on an image due to similar attenuation coefficients. However, XCT produces a polychromatic X-ray energy spectrum at 130kV with effective energy of 61.3keV. Due to high density nature of pyrite and chalcopyrite the effective energy can be hardened or attenuated such that the linear attenuation coefficient of both minerals is that of 130keV. Due to this, the true and expected grey values of chalcopyrite and pyrite at 130kV are not known. The same applies for 70kV voltage with effective energy of 45.5keV that it can also be attenuated such that the effective energy is increased to 70keV. Therefore, to effectively obtain the grey value representation of pyrite and chalcopyrite at both 70kV and 130kV, a grey value calibration is needed. A calibration was conducted by scanning a chalcopyrite standard sample together with a known sample that contained both pyrite and chalcopyrite to obtain grey values that represents the resulting effective energy and linear attenuation coefficients of these minerals. The scans were conducted several times such that the subtraction of 130kV from 70kV

scans resulted in an optimal discrimination of chalcopyrite from pyrite. Therefore, the relationship between chalcopyrite (minimum, mean and maximum) grey values at 130kV were compared to the chalcopyrite grey values at 70kV. This was done to obtain the grey value ratio that can be used to multiply the chalcopyrite grey values at 70kV in order to obtain the chalcopyrite grey value representation at 130kV without having to scan the sample. This information was then used to create a simulated image using ImageJ, a freely available software. To obtain the true dimensions of the simulated image, one of the images from the 70kV scan was used.

Due to the polychromatic nature of the X-ray beam that resulted in a variation of grey values, only a maximum grey value was considered and added to the simulated image (Fig. 5.2). This was done to optimize the discrimination of chalcopyrite from pyrite by removing all the pyrite grey values including those that overlap with chalcopyrite when a simulated image is applied during the subtraction. This was also done to improve the overall image contrast of other

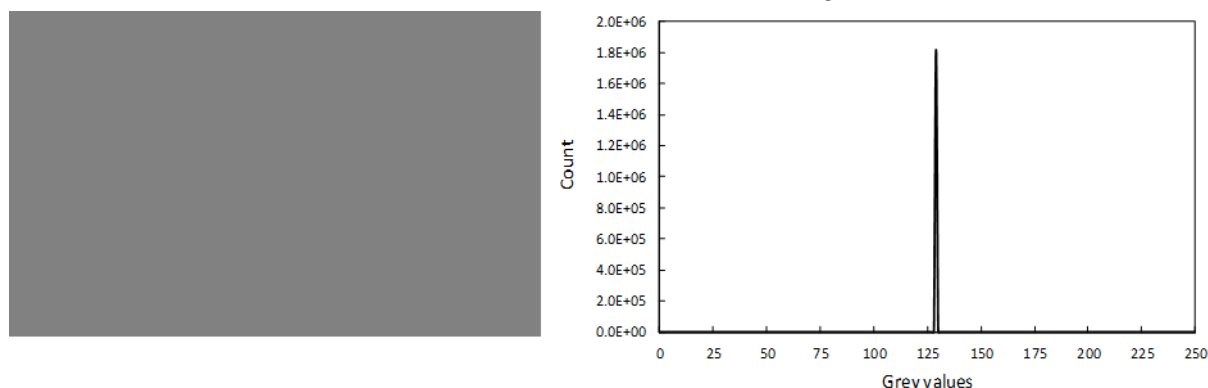


**Fig 5.2.** (a) Simulated images representing pyrite and chalcopyrite grey values at 130kV and (b) Pyrite and chalcopyrite grey value distribution assuming a monochromatic X-ray beam.

minerals with grey values higher than that of chalcopyrite at 70kV. The simulated grey value also assumes a monochromatic X-ray beam that results in the same attenuation coefficient of chalcopyrite and pyrite with a standard deviation of zero between all grey values. The simulated image discriminated minerals based on their linear attenuation coefficient only, it does not calculate or discriminate minerals based on effective atomic mass.

## 2.2. Samples

Four sample sets were used to test the applicability and effectiveness of the proposed and simplified dual energy method. The first sample was a Witwatersrand basin quartz conglomerate containing quartz (2.65 g/cm<sup>3</sup>), muscovite (2.82 g/cm<sup>3</sup>), chlorite (3.2 g/cm<sup>3</sup>), feldspar (2.56 g/cm<sup>3</sup>), biotite (3.05 g/cm<sup>3</sup>), sphene (3.53 g/cm<sup>3</sup>), pyrite (5.01 g/cm<sup>3</sup>) and chalcopyrite (4.20 g/cm<sup>3</sup>) (Nwaila et al., 2013). The second sample consisted of discrete chalcopyrite and pyrite mineral grains derived from the Witwatersrand basin ores,

separated using heavy liquid separation techniques. The third sample was an apatite-magnetite iron ore sample consisting of magnetite (5.18 g/cm<sup>3</sup>), ferromagnesian silicates, mica and amphibole (3.1 g/cm<sup>3</sup>), apatite (3.2 g/cm<sup>3</sup>), Na-feldspar (2.65 g/cm<sup>3</sup>), pyrite (5.01 g/cm<sup>3</sup>) and chalcopyrite (4.20 g/cm<sup>3</sup>) similar to samples used by Lund (2013). The fourth sample was a 4 mm piece of hematite sample (5.26 g/cm<sup>3</sup>). An additional standard chalcopyrite sample was used as a calibration sample in order to optimise the discrimination between chalcopyrite and pyrite during the dual energy subtraction analysis. All the samples were further analysed and confirmed by SEM-EDS and QEMSCAN analysis. However, the QEMSCAN blocks were not used for scanning due to the smaller grain sizes of pyrite and chalcopyrite which require high resolution.

## 2.3. X-ray Source Calibration

The X-ray source is one of the most important parts of the XCT system because it determines the

## CHAPTER 5: Dual Energy

resolution capabilities. It is contained within the NIKON XTH 225 ST system based at

the South African Nuclear Energy Corporation (Necsa) in the Microfocus X-ray Radiography/Tomography (MIXRAD) facility and the capabilities of this system are described by (Hoffman and de Beer, 2012). The source is capable of generating a voltage range from 30 up to 225 kV whilst the current ranges from 0 to 1 mA. The spot size where the X-rays are generated is around  $\sim 3.7 \mu\text{m}$  to provide relatively high resolution capability for various sample applications. The X-ray source uses a filament to produce electrons that interact with the tungsten target in order to generate X-rays. The filament has a lifetime which is determined by the frequently used X-ray voltage and is quickly depleted when high X-ray voltages  $> 150\text{kV}$  are used which makes it last for about 90 to 100 hours of scanning time.

For every filament change, an alignment of the X-ray beam is conducted which determines the quality of an image in terms of sharpness and consistent distribution of the X-ray flux across all the image pixels. To ensure optimal quality of the beam, the beam is aligned at three different X-ray voltages with a minimum of 60kV and a maximum of 225kV. The alignment at minimum X-ray voltage is done using both physical and electronic alignment. The other two X-ray voltages are only aligned electronically and then interpolated in order to incorporate all other X-ray voltages. The X-ray beam x and y-axis centre position can change for each X-ray energy during this interpolation process and this can limit the application of the dual energy technique even though the sample is stationary. For optimal application of the dual energy technique it is important that the X-ray beam maintains its centre position for all the X-ray voltages. Figure 5.3 shows two images of a tungsten cross scanned at 70kV, 130kV and the resulting image after subtraction that determines the reliability of the resulting image to discriminate sample information that requires dual energy application. The tungsten cross was used to align and focus the beam and evaluate the geometrical subtraction to determine possible errors associated with the X-ray beam. Figure 5.3C shows that the X-ray beam moved in both the x and y-axis direction during the voltage switching from 70kV

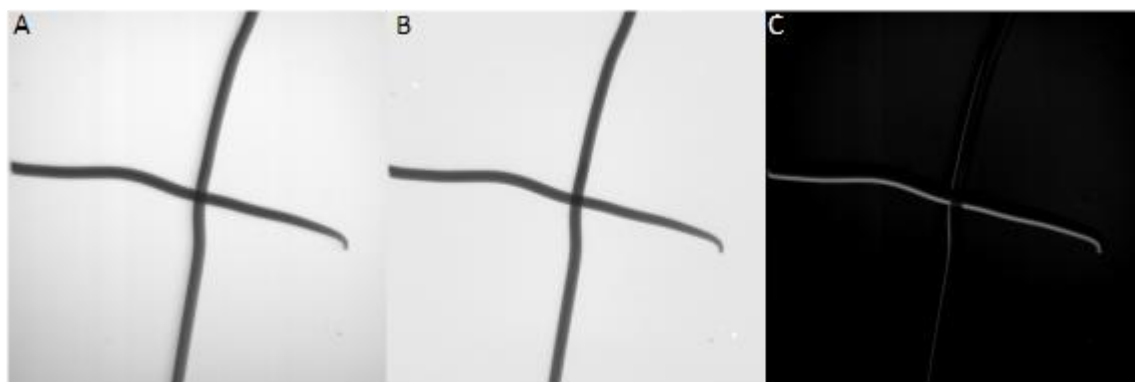


**Fig 5.3.** Tungsten cross used for X-ray beam alignment at (a) 70kV, (b) 130kV and (c) the resulting image to evaluate the X-ray beam position at both energies.

## CHAPTER 5: Dual Energy

**Table 5.1.**

Scanning conditions for all the sample

Sample	Condition	Voltage (kV)		Resolution ( $\mu\text{m}$ )
Witwatersrand basin quartz conglomerate	a	70	130	4.54
	b	70	130	4.54
	c	70	130	13.09
Discrete pyrite and chalcopyrite mineral separates	a	70	130	4.54
Apatite magnetite iron ore	a	70	130	4.54

to 130kV resulting in bright edge artefacts. This means that the scanned data has to be further processed in order to merge the reconstructed volumes to minimize the edge artefacts. This also means that an understanding of the capabilities together with the limitations of an XCT system are important in order to optimise its full operation. The lack of this understanding will limit the capability of the XCT system for dual energy application because the limitations or errors associated with the X-ray source are not well understood

sample when scanning the Witwatersrand quartz conglomerate. The 4 mm hematite

#### 2.4. Scanning Conditions

All the samples were scanned at 70kV (147 $\mu\text{A}$ , 4 seconds, 2000 projections, 0.25mm copper filter) and 130kV (67 $\mu\text{A}$ , 2 seconds, 2000 projections, 0.25mm copper filter). All the scans were reconstructed using CT Pro 3D reconstruction software. The software was also used to minimise the impact of beam hardening by applying a beam hardening correction factor of three. The VG Studio software version 3.2 was used to merge the reconstructed volumes obtained at both 70kV and 130kV. The conducted analyses are based on sample information only and excludes the background information. The samples were scanned together with the chalcopyrite standard sample for chalcopyrite grey value calibration after dual energy subtraction. The Witwatersrand basin rock sample was used to test the capability of the system to discriminate chalcopyrite from pyrite and also test the limitations of the dual energy method. The sample was subjected to three different conditions: a) when the X-ray beam is properly aligned; b) induced unsharpness of the X-ray beam; and c) experimentally inducing additional beam hardening. For the properly aligned X-ray beam condition, several scans were conducted and repeated until the discrimination of chalcopyrite was possible without the need to calibrate grey values. This was done in order to understand the relationship of chalcopyrite and pyrite grey values that represent the linear attenuation coefficient at both 70kV and 130kV without calibrating the grey values. The scans with induced unsharpness were conducted to evaluate the impact of unsharpness on the discrimination of chalcopyrite from pyrite. The scans with induced beam hardening were conducted by including a 4 hematite

## CHAPTER 5: Dual Energy

sample was not used as a filter but formed part of the Witwatersrand basin rock sample and rotated with it during scanning. The grey value relationship of pyrite and chalcopyrite that represent the linear attenuation coefficient on the first condition was applied to the second and third conditions in order to optimize the discrimination of chalcopyrite from pyrite. Table 5.1 shows the scanning conditions for all the samples and in particular the difference in resolution of the beam hardening induced scans due to the incorporated 4 mm hematite sample. All the dual energy results obtained from 70kV and 130kV scans were compared with the dual energy results obtained from 70kV scans and 130kV simulated image.

### 3. Results

#### 3.1. Dual Energy

This section assesses the factors affecting the application of dual energy method. The ability to minimize each factor is compared between the normal dual energy subtraction and the simplified dual energy subtraction method presented.

##### 3.1.1. Beam Alignment

The variation in grey values between chalcopyrite and pyrite when scanned at 70kV and 130kV voltage is shown in Fig. 5.4A and B. At 70kV, the pyrite and chalcopyrite grains are not easily differentiated because of their overlapping grey values and this is observable in their broader grey value peak (Fig. 5.5). This is due to the fact that the effective X-ray energy of 45.5keV (70kV) is attenuated such that the linear attenuation coefficient of pyrite and chalcopyrite is equivalent to that of 70keV. The expected linear attenuation coefficient difference between pyrite ( $7.47\text{cm}^{-1}$ ) and chalcopyrite ( $9.19\text{cm}^{-1}$ ) at 45.5keV is 18.71% which is enough to render discrimination. However, at 70keV the linear attenuation coefficient difference between pyrite ( $2.61\text{cm}^{-1}$ ) and chalcopyrite ( $2.73\text{cm}^{-1}$ ) is 4.4% which results in significant grey value overlap making it difficult to discriminate the minerals. The considered grey value information for pyrite and chalcopyrite in Figure 5.5 excludes the chalcopyrite standard sample. The discrimination between the grey values is even more difficult at 130kV because they share a similar attenuation coefficient as shown by the narrow peak of pyrite

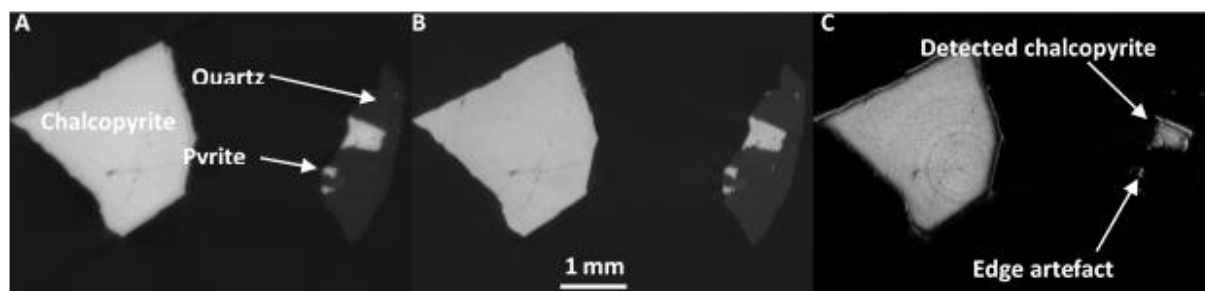


**Fig 5.4.** Witwatersrand basin quartz conglomerate sample scanned at (A) 70kV, (B) 130kV and (C) the discrimination of chalcopyrite from pyrite grains through dual energy subtraction method.

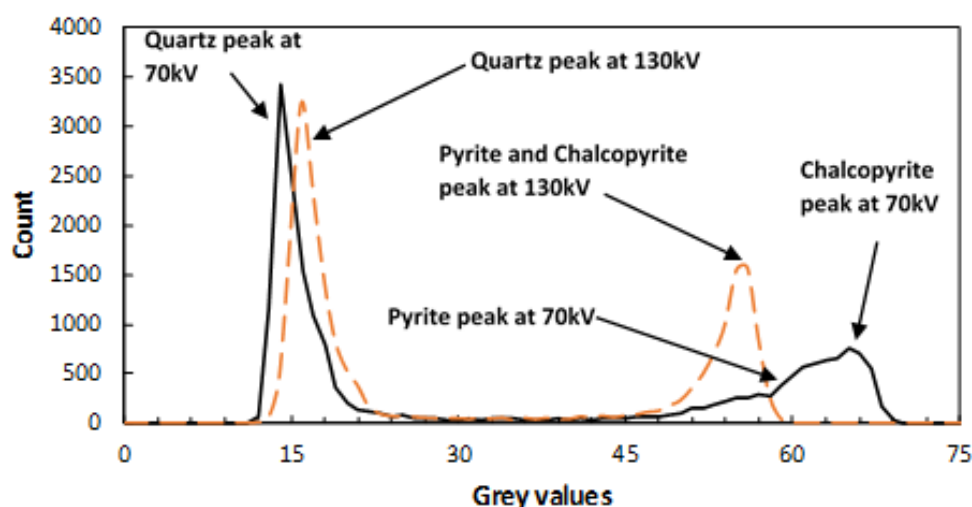


**Fig 5.5.** Distribution of peak positions for quartz, pyrite and chalcopyrite at 70kV and 130kV with optimized X-ray beam alignment.



## CHAPTER 5: Dual Energy



**Fig 5.6.** (a) Witwatersrand basin quartz conglomerate scanned at 70kV, (b) Simulated grey values of pyrite and chalcopyrite at 130kV and (c) Dual energy subtraction result.

and chalcopyrite at 130kV (Fig. 5.5). The narrow peak represents a highly attenuated X-ray beam with linear attenuation coefficient difference  $< 1\%$  between pyrite ( $0.947\text{cm}^{-1}$ ) and chalcopyrite ( $0.949\text{cm}^{-1}$ ) at 130kV. This means that the linear attenuation coefficient of pyrite and chalcopyrite is that of 130keV energy. This is different from the expected linear attenuation coefficient difference of 10.65% between pyrite ( $3.69\text{cm}^{-1}$ ) and chalcopyrite ( $4.13\text{cm}^{-1}$ ) at 61.3keV effective energy. The narrow peak contains grey values responsible for removing the pyrite grey values on the 70kV image during the dual energy subtraction method using the scans. The grey value peak positions for both pyrite and chalcopyrite at 70kV and 130kV represents the attenuation coefficient behaviour and the subtraction of the two images results in the discrimination of chalcopyrite from pyrite as shown in Fig. 5.4C. However, the subtraction of the two images resulted in a small edge artefact even after the volume data was aligned and merged. The edge artefact can lead to the misinterpretation or over estimation of the resulting chalcopyrite grain sizes.

The 70kV scan was also processed using the 130kV simulated image Fig. 5.6(A and B). The subtraction between an image slice acquired at 70kV and a simulated image also resulted in the discrimination of chalcopyrite from pyrite (Fig. 5.6C). However, the resulting chalcopyrite particle surface area in Fig. 5.6C is 38% smaller as compared to the chalcopyrite grain or particle surface area in Fig. 5.6A. This is due to the utilised single grey value of the simulated image after dual energy subtraction which removes all intermediate grey values between pyrite and chalcopyrite, Fig. 5.6C.

### 3.1.2. Unsharpness

The scanned data with induced unsharpness was calibrated based on the chalcopyrite standard sample grey values (Fig. 5.5) in order to optimise the discrimination between chalcopyrite and pyrite. Figure

5.7 (A and B) shows the Witwatersrand quartz conglomerate scanned at 70kV and 130kV and shows the dual energy result after subtracting the 130kV scan from the 70kV scan and, the 130kV simulated image from the 70kV scan. The discrimination between chalcopyrite and pyrite in both cases is difficult. This is evident in their grey value distribution at both X-ray voltages (Fig. 5.8). The dual energy subtraction using the 70kV and 130kV scans (Fig. 5.7C) could not discriminate chalcopyrite from pyrite. However, the dual energy subtraction using the 70kV scan and a simulated image could discriminate between chalcopyrite from pyrite (Fig. 5.7D). This shows the importance of the simulated image especially in cases where the acquired scans cannot yield any meaningful results due to unsharpness present in both 70kV and 130kV scans (Fig. 5.7C). The percentage difference between the detected chalcopyrite grain surface area in Fig. 5.7D is 40% smaller as compared to the original particle surface area in Fig. 5.7B.

### 3.1.3. Beam Hardening Artefacts

The Witwatersrand quartz conglomerate with experimentally induced beam hardening demonstrates the impact of beam hardening on structural information (Fig. 5.9A to D). There is a clear difference in structural definition (cracks) before and after beam hardening was induced. The induced beam hardening also causes pixilation or rough textures within the sample structures. This is shown by the narrow peak distribution between quartz, pyrite and chalcopyrite peak at 70kV (Fig. 5.10). The quartz peak also shows two peaks as if there are two different minerals as compared to the narrow quartz peak at 130kV (Fig. 5.10). The peak positions of pyrite and chalcopyrite at 70kV also show a decrease in grey values as compared to the same peaks at 130kV. This was even after the samples were calibrated the same as the samples shown in Fig. 5.4 A,B that resulted in the discrimination of chalcopyrite

## CHAPTER 5: Dual Energy

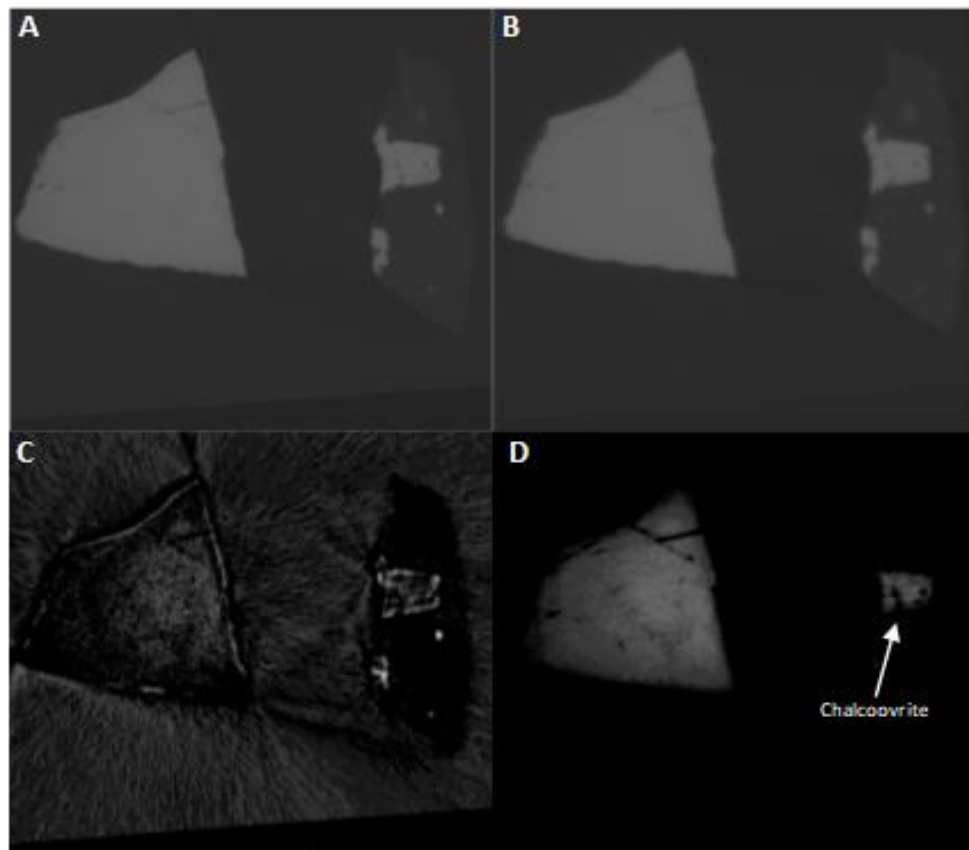


**Fig 5.7.** Witwatersrand basin quartz conglomerate scanned at (a) 70kV, (b) 130kV, (c) dual energy subtraction between 70kV and 130kV and (d) dual energy subtraction between 70kV and 130kV simulated image.

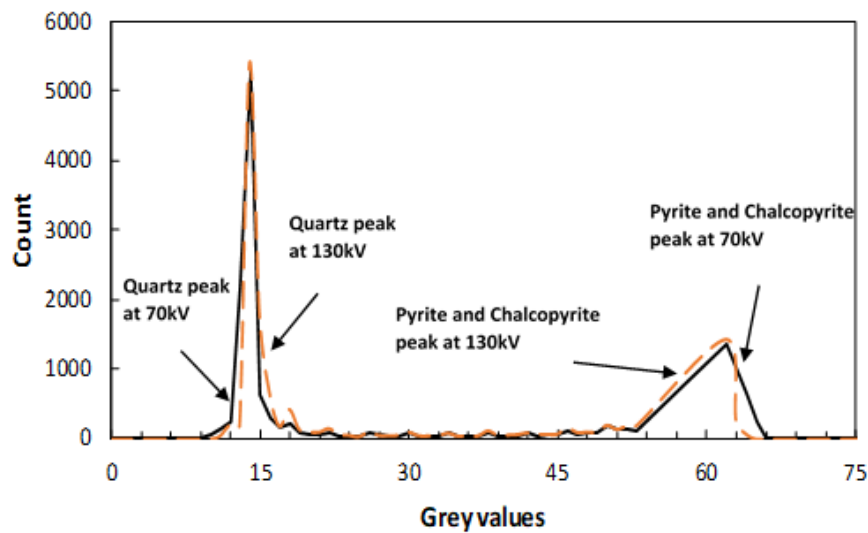


**Fig 5.8.** Distribution of peak positions for quartz, pyrite and chalcopyrite at 70kV and 130kV influenced by misaligned X-ray beam.

from pyrite after dual energy subtraction. This grey value peak distribution affects the dual energy subtraction due to the overall altered grey values of these minerals (Fig. 5.11A) where the dual energy subtraction using the 70kV and 130kV could not discriminate chalcopyrite from pyrite. The dual energy subtraction using the simulated image also could not

discriminate between the internal chalcopyrite from pyrite, only a part of chalcopyrite standard sample could be detected Fig. 5.11B. The remaining chalcopyrite standard sample surface area is 68% smaller than its original surface area.

## CHAPTER 5: Dual Energy

## 3.2. Application of Dual Energy to Different Samples

The application of the dual energy subtraction method together with the utilization of the 130kV simulated image were further applied to two different samples. The first sample was the Witwatersrand discrete pyrite and chalcopyrite grains. The application of the dual energy subtraction method to the discrete pyrite and chalcopyrite grains resulted in discrimination of the chalcopyrite standard sample from pyrite but the image still suffered from the edge artefact (Fig. 5.12B). No chalcopyrite grains within the sample could be detected at that position. The dual energy subtraction using the simulated image also produced the same image result but with no edge artefact (Fig. 5.12C). Figure 5.12(A to C) and (D to F) show two different slice positions of the same sample. The dual energy subtraction method using the 70kV and 130kV scans was able to discriminate chalcopyrite from pyrite (Fig. 5.12E) but still resulted in edge artefacts. However, the dual energy method using the simulated method eliminated the edge artefacts (Fig. 5.12F). It can be clearly observed on Figure 5.12D that there are three big grains that look similar (bottom left, bottom right and top centre) but after the application of dual energy method the grain on the bottom left was removed (Fig. 5.12E and F). The remaining grains have the same grey values with the standard chalcopyrite sample.

The second sample to be evaluated was the apatite-magnetite iron ore using the dual energy subtraction method. The chalcopyrite discrimination was also evaluated in different sample regions (Fig

5.13A and D). The dual energy subtraction method was able to discriminate chalcopyrite (Fig. 5.13B) but the dual energy method using the simulated image detected more particles (Fig. 5.13C). For the second

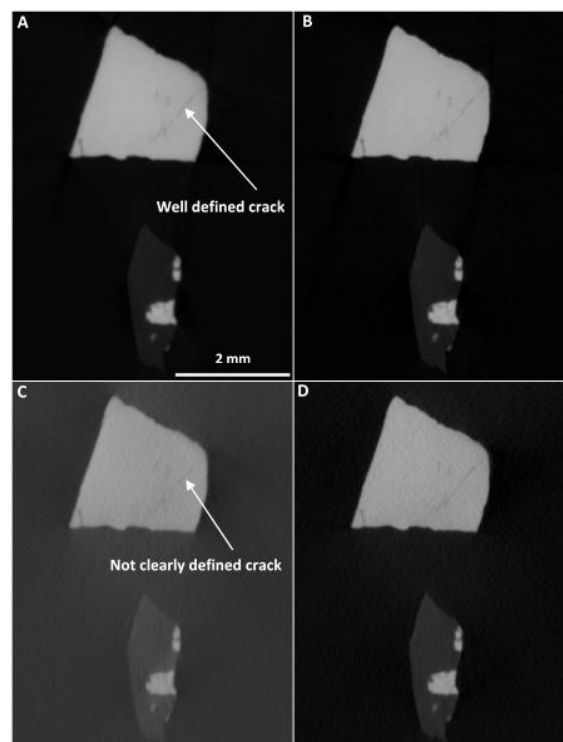


**Fig 5.9.** Witwatersrand basin quartz conglomerate scanned at (A) 70kV, (B) 130kV before induced beam hardening artefact and (C) 70kV and (D) 130kV after beam hardening has been induced experimentally.

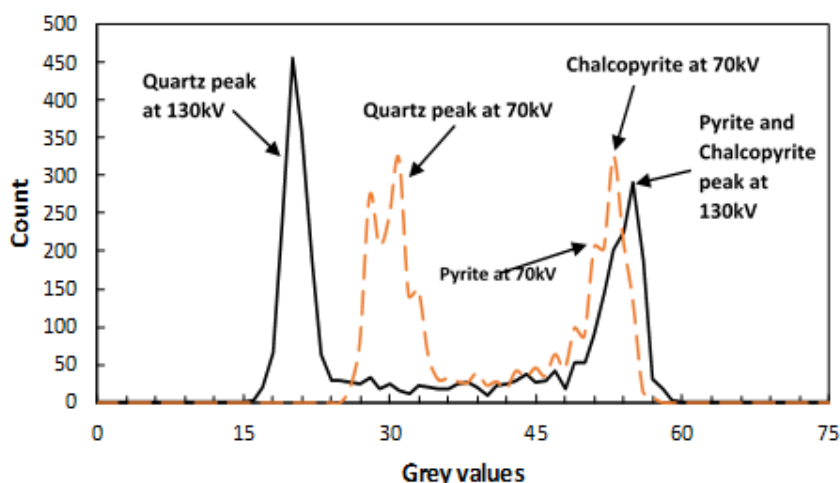


**Fig 5.10.** Distribution of peak positions for quartz, pyrite and chalcopyrite at 70kV and 130kV influenced by beam hardening artefact

## CHAPTER 5: Dual Energy

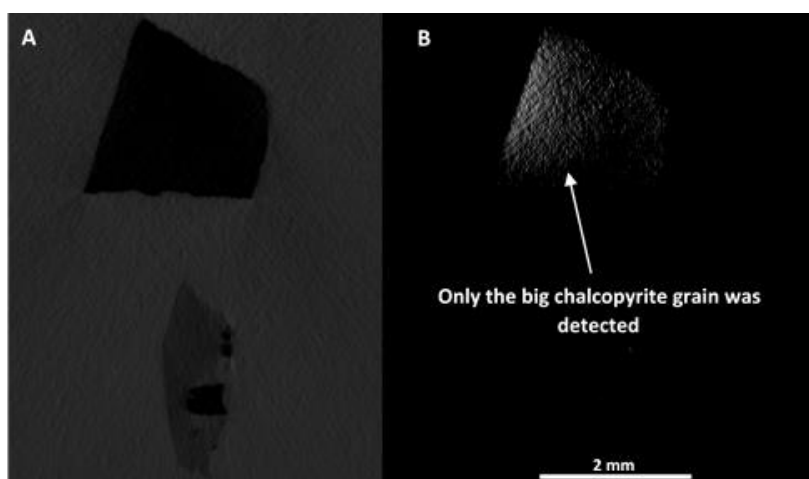


**Fig 5.11.** (a) Dual energy subtraction of 70kV and 130kV scans and (b) dual energy subtraction of 70kV scan and 130kV simulated image.

region of the sample, the dual energy subtraction method could not discriminate chalcopyrite (Fig. 5.13E) due to the larger edge artefact that affects the discrimination of the smaller chalcopyrite particles. The utilization of the simulated image was able to discriminate chalcopyrite grains (Fig. 5.13F). In the case of the dual energy method using 70kV and 130kV scans the edge artefacts were still observable. However, the discrimination of magnetite from chalcopyrite was optimized by both the normal dual energy subtraction method and the simplified dual energy method.

#### 4. Discussion

The dual energy results show the importance of understanding the system capabilities and the contribution of each component of the system towards quantifiable and reliable information. Dual energy is one of the methods that can be used to evaluate the systematic errors associated with the X-CT system (X-ray source). In addition to this, is an understanding of the artefacts associated with the sample itself, which

can limit its application to differentiation of minerals that share similar linear attenuation coefficients using the normal dual energy subtraction method.

##### 4.1. Impact of X-ray Source

The application of the dual energy method using the scanning information where the X-ray source was optimally aligned was able to discriminate chalcopyrite from pyrite within the Witwatersrand basin quartz conglomerate sample (Table 5.2). But the method suffered from edge artefacts that result in the overestimation of the discriminated chalcopyrite particles. The edge artefacts show how difficult it is to properly align the X-ray beam, which affects the application of the dual energy subtraction method using the 70kV and 130kV scans. However, the utilization of the simulated image resolved the edge artefacts but resulted in a reduced particle surface area that is 38% smaller than its original particle surface area (Table 5.2). Table 5.2 summarises the advantages and disadvantages of the dual energy method using the scanned

## CHAPTER 5: Dual Energy

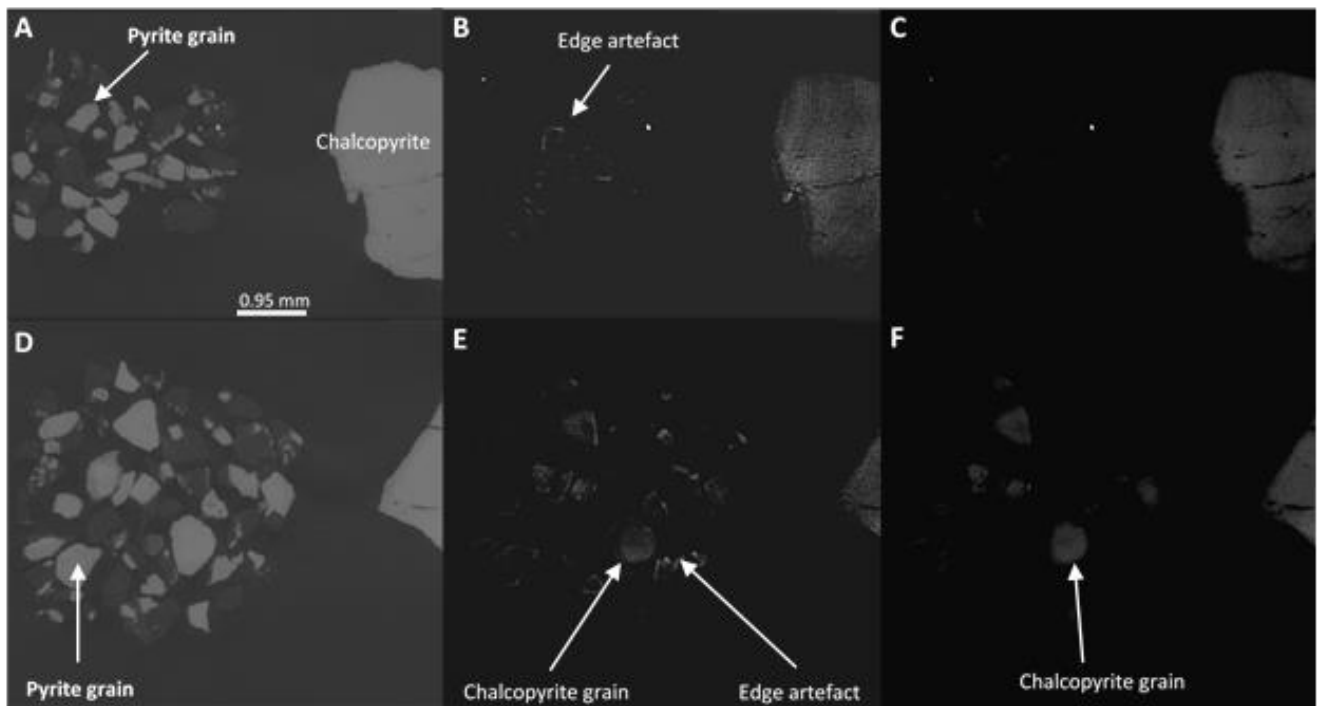


**Fig. 5.12.** The Discrete pyrite and chalcopyrite mineral separates scanned at 70kV (a) and (d), processed with dual energy subtraction using 70kV and 130kV scans (b) and (e), and also processed with dual energy subtraction using a 70kV scan and 130kV simulated image (c) and (f).

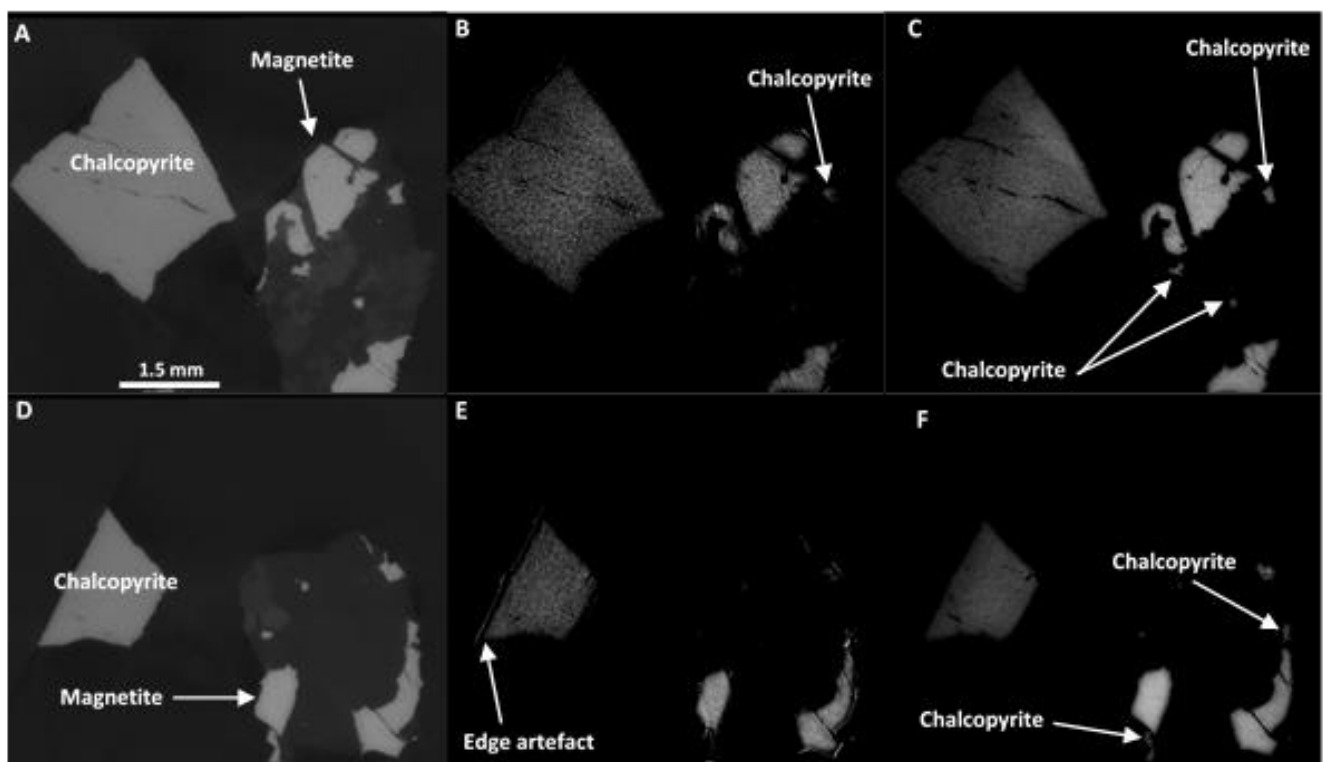


**Fig 5.13.** Two different slice positions of the apatite magnetite iron ore scanned at (A) and (D) 70kV, (B) and (E) dual energy subtraction result using 70kV and 130kV scans and, (C) and (F) dual energy subtraction method using the 70kV and 130kV simulated image.

## CHAPTER 5: Dual Energy

**Table 5.2.**

Comparison between the experimental and experimental + simulated image result of the dual energy method

Sample	Condition	Experimental Result			Experimental + Simulated Result		
		Chalcopyrite discrimination	Artefact	Duration	Chalcopyrite discrimination	Artefact	Duration
Witwatersrand basin quartz conglomerate	Beam alignment	Yes	Edge	2 Scans	Yes	Reduced surface area	1 Scan
	Unsharpness	No	Edge	2 Scans	Yes	Reduced surface area	1 Scan
	Beam hardening	No	No detection	2 Scans	No	No detection	1 Scan
Pyrite chalcopyrite discrete grains	Beam alignment	Yes	Edge	2 Scans	Yes	Reduced surface area	1 Scan
Apatite-magnetite sample	Beam alignment	Yes	Edge	2 Scans	Yes	Reduced surface area	1 Scan

data, and the scanned and simulated image. From Table 5.2 it is clear that the utilisation of a single scan together with a simulated image, is a major advantage of the simplified dual energy method as compared to the traditional dual energy method.

The utilisation of the traditional dual energy method on the induced unsharpness scans did not result in discrimination of chalcopyrite from pyrite due to an overlap in grey values between chalcopyrite and pyrite. This also demonstrates how sensitive the traditional dual energy method is to changes in grey values. The utilization of the simulated image took advantage of the slight difference between chalcopyrite and pyrite grey values because it uses only a single grey value to discriminate the minerals but it resulted in a reduced chalcopyrite grain surface area (Table 5.2).

#### 4.2. Impact of Beam Hardening

The utilization of the traditional dual energy method using 70kV and 130kV scans could not discriminate between chalcopyrite from pyrite due to heavily altered grey values at 70kV. The changed grey values gave an impression that the linear attenuation coefficients of chalcopyrite and pyrite are lower at 70kV as compared to 130kV and this is not true. This further shows that the impact of beam hardening also affects the true representation of grey values between chalcopyrite and pyrite which makes it difficult for the traditional dual energy subtraction method to discriminate the minerals. The application of the simulated image also could not discriminate smaller chalcopyrite grains (Table 5.2). However, the bigger chalcopyrite standard sample could still be observed after the subtraction was applied with a surface area difference of 68% when compared to the original surface area. This

shows that beam hardening does change the grey values of the minerals within the sample but that the impact is not uniform which makes it difficult to discriminate minerals with similar attenuation coefficients.

#### 4.3. Application of Dual Energy

Application of the traditional dual energy subtraction method resulted in effective discrimination in all three case studies. However, the method still suffered from the presence of edge artefacts due to errors associated with the X-ray source. The application of the simulated image was able to minimize this artefact (Table 5.2). In the case of the apatite-magnetite iron ore sample, use of the simulated image resulted in the detection of more chalcopyrite grains than the traditional dual energy subtraction method. This is thought to be due to larger edge artefacts that are within the grain size range resulting in the elimination of smaller grains during the dual energy subtraction.

### 5. Conclusion

XCT is a powerful technique capable of providing 3D mineralogical and textural information. The capability of XCT to provide reliable and quantifiable information though requires a full understanding of the XCT system limitations. Understanding the limitations leads to appropriate method developments that minimize the system limitations in order to optimize and broaden the application of XCT. This is evident in the development and application of the simplified dual energy method that addresses limitations associated with the X-ray source. The method has the advantage



## CHAPTER 5: Dual Energy

that it yields rapid dual energy results instead of the more time consuming method of scanning two sample volumes. The method is demonstrated by showing how chalcopyrite and pyrite can be discriminated in samples associated with beam hardening, where the traditional dual energy method struggles. This means that the method can be extended to various high density samples that are known to be associated with different levels of beam hardening. In particular, further study is needed to optimize the method in cases where the sample is highly affected by beam hardening.

## 6. Acknowledgements

The authors would like to thank Necsa and the management team for funding and access to the Microfocus system in the MIXRAD Lab, which is a DST-NRF (Department of Science and Technology – National Research Funding) funded facility through the NEP-RISP (National Equipment Programme – Research Infrastructure Support Programmes) program. The project is generously supported through the South African Minerals to Metals Research Initiative (SAMMRI). The authors would also like to thank Glen Nwaila for providing with the Witwatersrand samples. This work is based on the research supported in part by the National Research Foundation of South Africa (Grant Numbers 86054, 99005). Any opinions, findings and conclusions or recommendations expressed in any publication generated by the NRF supported research is that of the author(s), and that the NRF accepts no liability whatsoever in this regard

## 7. References

- Aran, S., Besheli, L.D., Karcaaltincaba, M., Gupta, R., Flores, E.J., Abujudeh, H.H., 2014. Applications of dual-energy CT in emergency radiology. *Am. J. Roentgenol.* 202, 314–324. <https://doi.org/10.2214/AJR.13.11682>
- Bam, L.C., Miller, A.J., Becker, M., Basson, I.J., 2019. X-ray Computed Tomography: Practical Evaluation of Beam Hardening in Iron Ore Samples. *Miner. Eng.* 131, 206–215. <https://doi.org/10.1016/j.mineng.2018.11.010>
- Bam, L.C., Miller, J., Becker, M. A simple Tool to Calculate X-ray Linear Attenuation Coefficients to Assess Mineralogical Differentiation for X-ray Computed Tomography Scanning, In preparation.
- Cruvinel, P.E., Balogun, F.A., 2000. Minitomography scanner for agriculture based on dual-energy Compton scattering, in: 13th Brazilian Symposium on Computer Graphics and Image Processing. Gramado, pp. 193–199. <https://doi.org/10.1109/SIBGRA.2000.883913>
- Fessler, J.A., Elbakri, I., Sukovic, P., Clinthorne, N.H., 2002. Maximum-likelihood dual-energy tomographic image reconstruction, in: Sonka, M., Fitzpatrick, J.M. (Eds.), *SPIE Medical Imaging*. pp. 4684–4685. <https://doi.org/10.1117/12.467189>
- Forghani, R., De Man, B., Gupta, R., 2017. Dual-Energy Computed Tomography: Physical Principles, Approaches to Scanning, Usage, and Implementation: Part 2. *Neuroimaging Clin. N. Am.* 27, 385–400. <https://doi.org/10.1016/j.nic.2017.03.003>
- Foust, A.M., Nguyen, X. V., Prevedello, L., Bourekas, E.C., Boulter, D.J., 2018. Dual-energy CT cisternography in the evaluation of CSF leaks: A novel approach. *Radiol. Case Reports* 13, 237–240. <https://doi.org/10.1016/j.radcr.2017.09.005>
- Hoffman, J.W., de Beer, F.C., 2012. Characteristics of the Micro-Focus X-ray Tomography Facility ( MIXRAD ) at Necsa in South Africa, in: 18th World Conference on Nondestructive Testing. pp. 1–12.
- Ilovea, M., Dului, O., Oaie, G., Ricman, C., Mateiasi, G., 2006. Dual-energy computer tomography and digital radiography investigation of organic and inorganic materials, in: *Proceedings of European Conference on Non Destructive Testing*. pp. 1–13.
- Ketcham, R.A., Carlson, W.D., 2001. Acquisition , optimization and interpretation of X-ray computed tomographic imagery : applications to the geosciences. *Comput. Geosci.* 27, 381–400.
- Lund, C., 2013. Mineralogical, Chemical and Textural Characterisation of the Malmberget Iron Ore Deposit for a Geometallurgical Model. Luleå University of Technology.
- Noguchi, K., Itoh, T., Naruto, N., Takashima, S., Tanaka, K., Kuroda, S., 2017. A Novel Imaging Technique (X-Map) to Identify Acute Ischemic Lesions Using Noncontrast Dual-Energy Computed Tomography. *J. Stroke Cerebrovasc. Dis.* 26, 34–41. <https://doi.org/10.1016/j.jstrokecerebrovasdis.2016.08.025>
- Nwaila, G., Becker, M., Ghorbani, Y., Petersen, J., Reid, D., Bam, L., de Beer, F., Franzidis, J.-P., 2013. A geometallurgical study of the Witwatersrand gold ore at Carletonville, South Africa. 2nd AusIMM Int. Geometallurgy Conf. 75–84.
- Obaid, D.R., Calvert, P.A., Gopalan, D., Parker, R.A., West, N.E.J., Goddard, M., Rudd, J.H.F., Bennett, M.R., 2014. Dual-energy computed tomography imaging to determine atherosclerotic plaque composition: A prospective study with tissue validation. *J. Cardiovasc. Comput. Tomogr.* 8, 230–237. <https://doi.org/10.1016/j.jcct.2014.04.007>
- Rebuffel, V., Dinten, J., 2006. Dual-Energy X-Ray Imaging : Benefits and Limits, in: 9th European Conference on NDT. pp. 1–12.
- Robert-Coutant, C., Moulin, V., Sauze, R., Rizo, P., Casagrande, J.M., 1999. Estimation of the matrix attenuation in heterogeneous radioactive waste drums using dual-energy computed tomography. *Nucl. Instruments Methods Phys. Res. Sect. A Accel. Spectrometers, Detect. Equip.* 422, 949–956. [https://doi.org/10.1016/S0168-9002\(98\)01053-5](https://doi.org/10.1016/S0168-9002(98)01053-5)
- Roder, F.L., 1979. Explosives detection by dual-energy computed tomography (CT), in: *SPIE Vol. 182 Imaging Applications for Automated Industrial Inspection and Assembly*. SPIE, pp. 171–178.
- Stenner, P., Berkus, T., Kachelriess, M., 2007. Empirical dual energy calibration (EDEC) for cone-beam

## CHAPTER 5: Dual Energy

computed tomography. *Med. Phys.* 34, 3630–3641.  
<https://doi.org/10.1118/1.2769104>

Taguchi, N., Oda, S., Kobayashi, T., Naoe, H., Sasaki, Y., Imuta, M., Nakaura, T., Yamashita, Y., 2018. Advanced parametric imaging for evaluation of Crohn's disease using dual-energy computed tomography enterography. *Radiol. Case Reports* 13, 709–712. <https://doi.org/10.1016/j.radcr.2018.04.002>

Wellington, S.L., Vinegar, H.J., 1987. X-ray Computirized Tomography. *Soc. Pet. Eng. J.* 39.  
<https://doi.org/doi.org/10.2118/16983-PA>

---

**PAPER PUBLICATION HISTORY**

---

<b>Title</b>	Customisation of XCT scanning protocols for the quantification of textural attributes in high density ores
<b>Journal</b>	Minerals Engineering
<b>Status</b>	To Be Submitted February 2020
<b>Authors and roles</b>	L C Bam – PhD Candidate J A Miller – Primary Supervisor M Becker – Secondary Supervisor
<b>Applicant Contribution</b>	Conceptualization, Formal analysis, Methodology, Writing—original draft & editing (80%).

---

# Customisation of XCT scanning protocols for the quantification of textural attributes in high density ores

L Bam<sup>a,c</sup>, M Becker<sup>b</sup>, J Miller<sup>a</sup>

- a. Department of Earth Sciences, Stellenbosch University, Private Bag X1, Matieland 7601, South Africa. Email: lunga.bam@necsa.co.za; jmiller@sun.ac.za*  
*b. Centre for Minerals Research, Department of Chemical Engineering, University of Cape Town, Private Bag, Rondebosch 7701, South Africa. Email: megan.becker@uct.ac.za*  
*c. Department Radiation Science, Necsa, PO Box 582, Pretoria, South Africa. Email: lunga.bam@necsa.co.za*

## ARTICLE INFO

### Keywords:

Dual energy,  
Loss of information,  
%Error  
Porosity,  
Chalcopyrite,

## ABSTRACT

X-ray computed tomography is increasingly used to visualize and quantify ore characteristics in 3D for a variety of minerals processing applications. The success of the technique to produce reliable data is a function of optimal scanning parameters, sample density and size especially when dealing with high density samples that are more subject to image artefacts. To assist with this there is a need to use a standard when scanning high density samples (with a specific gravity > 3.5) in order to improve the accuracy of the scan information by quantifying error's due to beam hardening. In this study, the advantages of using an aluminium metal standard are demonstrated for the quantification of two different textural attributes in high density ores: (i) porosity information for iron ore and (ii) chalcopyrite grain size distribution in a polymetallic sulphide ore. The latter is also coupled with a newly developed 'simplified' dual energy method (Chapter 5). Data reliability is defined as %Error. Values below 10% indicate that the data is reliable whereas values above 10% means that there is a loss of information and the quantified information is unreliable as presented in Chapter 4. The quantified 3D porosity information of two different iron ore samples sets (Brazilian and South African) were extracted from sample regions where %Error was less than 10%. In the three Brazilian samples investigated, porosity was found to be 7.20, 1.70 and 2.10%, while for the South African iron ore, a porosity of 3.20% was determined. The quantified porosity information is comparable with the QEMSCAN 2D data except for the South African ore where QEMSCAN gave a porosity of 0.85%. This difference is interpreted to be due to non-uniform distribution of porosity within that ore sample. Applying the same approach of only using data with a %Error of less than 10%, the chalcopyrite 3D grain size distribution determined using X-ray computed tomography showed similar grain size distribution patterns to conventional 2D QEMSCAN data with a larger difference in absolute grain sizes. Based on the above results, it is evident that X-ray computed tomography can provide accurate mineralogical information on high density ores for minerals processing purposes.

## 1. Introduction

X-ray computed tomography (XCT) is increasingly used to visualize and quantify ore characteristics in 3D for a variety of minerals processing and metallurgical applications (Evans et al., 2015; Fagan-Endres et al., 2017; Ghorbani et al., 2011; Lin et al., 2017; Miller and Lin, 2003; Miller et al., 1990). Of specific interest is its ability to characterise and quantify texture in 3D, where texture can be defined as the inter-relationship between the different mineral grains in the rock or particle. The success of the technique to provide textural information relies on the effective X-ray penetration. This is most easily obtained for small and

low-density samples or samples that consist of a distinct variation in mineral densities. However, this is not the case when dealing with high-density ore samples because they are associated with beam hardening that results in image artefacts and therefore unreliable textural information, limiting the application of XCT. High density samples are defined here as those ores with a specific gravity greater than 3.5 that are typically comprised of high proportions of dense minerals such as the sulphides (e.g. pyrite, chalcopyrite, galena) and / or oxides (e.g. magnetite, chromite, hematite). Beam hardening occurs when the low energetic X-rays are absorbed more and high energetic ones are 'hardened' as they penetrate

## CHAPTER 6: Case Studies

through the sample. This results in an uneven grey value distribution of the same material or mineral depending on both its location within the sample as well as the distribution of other minerals around it. In most cases, it is difficult to overcome the issue of beam hardening by simply increasing the X-ray energy because the discrimination of most minerals with respect to the attenuation coefficient is more pronounced in the low X-ray energy range. This means prior sample mineralogical information is important to determine the attenuation coefficient of the minerals under investigation (see Chapter 2 and 3). Thereafter, the attenuation coefficient information can be used to determine the optimal scanning parameters in order to better discriminate the minerals of interest and minimize scanning artefacts (Bam et al., 2016).

However, when dealing with high density ores, simply applying optimal scanning parameters is often insufficient because the extent of beam hardening is unknown and thus difficult to minimize. One of the simplest ways to minimize beam hardening for a given X-ray energy is to increase the X-ray flux. However, there is a spot size limitation that defines the resolution, and this puts a limit to the X-ray flux in order to maintain a true resolution (Lin et al., 2018). Other ways to minimize the impact of beam hardening are increasing either the exposure time or the number of projections or both (Lin et al., 2018) or utilizing a filter material (Bucher et al., 2016; Kheruka et al., 2011). Although all of these methods are relatively useful in minimising beam hardening artefacts in XCT scan information, their effectiveness when applied to high density samples is still compromised because they do not completely remove the impact of beam hardening. This motivated the development of a standardisation procedure using an aluminium metal standard sample, specifically for application to high density samples (Bam et al., 2019). The utilization of the aluminium standard sample has been shown to be effective in identifying areas of the scanned volume where sample information has literally been 'lost' and cannot be recovered by any form of post-processing. The corollary to this is that it can also be used to determine the sample size associated with no loss or minimal loss of sample information due to beam hardening (Bam et al., 2019). This concept has been demonstrated by using the %Error (which is a comparison between the quantified pore areas of aluminium cylindrical sample within the images with the expected or known pore surface area) to evaluate whether a given sample volume is sufficient to provide an accurate representation of the ore characteristics (Bam et al., 2019).

The dual energy method is also one of the methods that can be used to minimize the impact of beam hardening because it combines scanning information acquired at both low and high X-ray energy (Stenner et al., 2007). Chapter 5) propose a simplified dual energy method that uses scanned data acquired at a lower X-

ray energy and a simulated image for high X-ray energy to improve mineralogical discrimination. The method was used to discriminate chalcopyrite from pyrite because they have similar attenuation coefficients. In the case of beam hardening, the scanned image and simulated image cannot be directly combined to discriminate the minerals. This is because different sample areas or information are affected differently by beam hardening at lower X-ray energy. However, quantification of the %Error using the aluminium standard sample can be used to identify usable sample information or regions for dual energy application to improve the accuracy of XCT to discriminate chalcopyrite from pyrite.

The objective of this paper is to further demonstrate the application of the aluminium standard sample in combination with the new simplified dual energy approach, by using two case studies. Each of the case studies considers a high density ore and then evaluates the quantification of specific attributes of relevance to the handling and processing of the ore. In the first case study, the aluminium standard sample is applied to determine porosity in drill core of two different iron ore sample sets. The characterisation and quantification of 3D porosity (a component of iron ore texture) in the scanned XCT volumes is of relevance to the physical processing (including the lump to fines ratio, liberation, gravity concentration, desliming and transportation) (Fonteneau et al., 2013) as well as downstream metallurgical properties (including sintering and pelletisation) of these ores (Bhuiyan et al., 2013; Muwanguzi et al., 2012; Shatokha et al., 2010). The XCT technique has previously been used to study and quantify porosity in both iron ore drill core (rock) samples (Bam et al., 2016; Fonteneau et al., 2013) as well as sinters and pellets (Bhuiyan et al., 2013; Muwanguzi et al., 2012; Shatokha et al., 2010). However, the quantification of porosity information has not been previously done on the ore samples themselves and hence it is not clear if the porosity information determined from the sinters and pellets is a true reflection of porosity in the unprocessed ores.

In the second case study, the simplified dual energy method is applied to discriminate chalcopyrite from pyrite, and thereafter to quantify chalcopyrite 3D grain size distribution in a high density polymetallic sulphide ore. The quantification of grain size distribution (a component of ore texture) is important in terms of the inherent rock strength, its breakage and liberation properties including the nature of composite ore and gangue particles, as well as grade, recovery and selectivity during flotation (Cropp et al., 2013; Parbhakar-Fox et al., 2011). As such, the quantification of grain size distribution is a particular parameter of interest when investigating ore heterogeneity and establishing geometallurgical units (Fragomeni et al., 2005; Gordon et al., 2018). A number of studies have previously used XCT

## CHAPTER 6: Case Studies

technology to quantify grain size distributions in 3D particularly those intending to further understand the magnitude and effects of stereological error (Evans et al., 2015; Reyes et al., 2017; Wang et al., 2018). However, the determination of reliable information using XCT to provide 3D chalcopyrite grain size distribution information (GSD) has not been done on high density and complex ores in order to evaluate if the quantified GSD is a true reflection of an ore sample.

## 2. Materials and Methods

The approach used for the two case studies presented here, consists of first determining sample regions that are not associated with a loss of sample information according to Chapter 4 by quantifying the %Error. Bam et al., (2019) found that %Error values less than 10% are not associated with high impact of beam hardening that leads to a loss of sample information. Therefore to obtain the %Error information in this case, the standard aluminium sample was drilled using a drill bit of 1mm diameter that generated a known or expected pore surface area of  $0.785\text{mm}^2$  where pore surface area is defined as the cross-sectional area of the pore perpendicular to the length of the pore. This pore surface area is then compared to the quantified pore surface area of the standard aluminium sample to obtain the %Error information. The %Error is basically a comparison or deviation between the quantified pore areas of an aluminium standard sample within the images against the expected or known pore area of  $0.785\text{mm}^2$  (Bam et al., 2019). Thereafter, the regions of low %Error are used to quantify porosity information in iron ore samples and measure the quantified chalcopyrite GSD in polymetallic sulphide ore samples. For both case studies, two dimensional automated SEM-EDS (QEMSCAN) techniques are used to complement and validate the results of the XCT scanning.

### 2.1. Samples

In both case studies, a combination of rock fragments and drill core samples were used. Case study 1 samples comprise a South African massive hematite sample (Sishen-type banded iron formation), as well as three Brazilian iron ore types (a compact coarse-grained hematite ore, a compact itabirite ore and a goethite ore). For case study 2, a sample was obtained from the magnetite dominated Upper Ore Body of the Swartberg polymetallic Cu-Pb-Zn sulphide ore in South Africa

(Gordon et al., 2018). 6mm and 4mm diameter drill cores were prepared from these samples as summarised in Table 6.1. The required core diameters were determined using the approach outlined in Chapter 4 that determines the sample size associated with no loss of sample information due to beam hardening.

### 2.2. QEMSCAN

The various rock pieces and drill core samples were prepared into 30mm, epoxy-resin mounted polished sections which were coated with an EMITECH Quorum carbon coater. Special care was taken during the sample preparation procedure to ensure that no plucking took place and this was verified using a binocular microscope. Samples were thereafter analysed using an FEI QEMSCAN 650F instrument in the Centre for Minerals Processing at the University of Cape Town fitted with two Bruker SDD detectors operating at (25kV, 10nA) using the QEMSCAN field image analysis routine. Samples were run at  $1500\text{ }\mu\text{m}$  field size with  $15\text{ }\mu\text{m}$  pixel spacing. All data processing and results quantification was carried out using the QEMSCAN iDiscover software..

### 2.3. X-Ray Computed Tomography

All XCT scanning were conducted using a NIKON XTH 225 ST system based at the South Africa Nuclear Energy Corporation (Necsa) in the Microfocus X-ray Radiography/Tomography (MIXRAD) facility (Hoffman and de Beer, 2012). A total number of four samples were scanned with 2000 projections, 4 seconds exposure time, 130kV (iron ore samples) and 70kV for the polymetallic sulphide ore sample. All the samples were scanned together with the aluminium standard sample in order to quantify the %Error. For the polymetallic sulphide ore sample, a chalcopyrite standard sample was included to optimize chalcopyrite discrimination. A 0.25 mm copper filter was also used to remove the low X-ray energies associated with beam hardening artefacts. The scans were reconstructed and corrected for beam hardening using the CT Pro 3D .



## CHAPTER 6: Case Studies

**Table 6.1**

Summary of the drill core samples analysed in Case studies 1 and 2.

Details		Description	Core diameter (mm)
Case study 1	South African iron ore	Massive banded iron formation	6
	Brazilian iron ore	Compact Hematite -	6
		Compact Itabirite -	6
		Goethite	4
Case study 2	Swartberg Polymetallic Cu-Pb-Zn ore	Upper ore body – magnetite dominated ore	6

**Table 6.2**

Scanning parameters for porosity quantification, optimization parameters and chalcopyrite discrimination.

Parameter Settings	Porosity Quantification	Optimization Parameters	Chalcopyrite Discrimination
X-ray voltage (kV)	130	70	70
Current (um)	77	143	143
Exposure time (sec)	2	1 – 4	4
Resolution (mm)	0.012	0.007	0.012
No of projections	2000	2000	2000

reconstruction software. The beam hardening correction factor of 3 was selected because it removed all the bright grey values on the edge of the samples. This result to reliable grey values that reflect the true mineralogical information of the sample. The data was then processed using VG Studio rendering software 3.2 and the open source ImageJ software.

*2.3.1. Iron Ore Case Study*

The iron ore samples were scanned to evaluate the reliability and the applicability of the aluminium standard sample to quantify porosity information in these high density ores. The aluminium standard sample has a pore diameter of 1 mm in order to evaluate the quality of the data produced. This was done by quantifying the %Error for each and every image slice representing the entire volume. In order to do this the aluminium standard sample was placed behind each sample being scanned. The method is still applied even after the optimal sample size was determined because the quantification of sample information in high density samples is not straight forward and the extent of beam hardening is still unknown. All iron ore samples were scanned at 130kV (equivalent to an effective energy of 61.3keV) in order to minimize beam hardening artefacts as shown in Table 6.2 under the porosity quantification parameter settings column. However, the X-ray beam with effective energy of 61.3keV can be attenuated or hardened such that it is equivalent to 130keV due to the high density nature of the samples. The %Error of the scanned data was first quantified to determine if there is a loss of sample information before porosity information is quantified.

*2.3.2. Polymetallic Sulphide Ore Case Study*

Several preliminary scans of the polymetallic sulphide ore samples were conducted to determine optimal scanning parameters for chalcopyrite discrimination. The procedure to determine the optimal scanning parameters to obtain mineralogical information was adopted from Bam et al. (2016). The selected X-ray voltage to evaluate the applicability of the procedure was 70kV (equivalent to an effective energy of 45.5keV) based on the simplified dual energy method to discriminate chalcopyrite from pyrite grains (Bam et al., In preparation a). This effective energy can also be attenuated such that it is equivalent to 70keV. The sample was scanned

## CHAPTER 6: Case Studies

with varying exposure times to determine the optimal SNR (Table 6.2). The data set acquired at 4 seconds exposure time had the least amount of noise within an image as compared to data set acquired at 1 and 2 seconds exposure time (Fig. 6.7A to C). Like the iron ore samples, 2000 projections were used to scan. These optimal scanning parameters were then used to scan the polymetallic sulphide ore sample. The sample was also scanned with the chalcopyrite standard sample to optimize the chalcopyrite grain discrimination. The dual energy method used to discriminate chalcopyrite from pyrite is adopted and described by Bam et al. (In preparation a). The method uses a simplified dual energy subtraction approach that relies on a single scanning condition at 70kV and a simulated image at 130kV. The resulting image grey values are then compared with the chalcopyrite standard sample to optimize chalcopyrite grain discrimination.

### 3. Iron Ore Case Study

#### 3.1. Results

Before the porosity information was measured, the average pore grey value was first determined using the

partial volume effect of the two component system (pore and hematite/goethite) to determine the boundary between the minerals and pores. The %Error was then quantified to identify regions of the ore samples that are associated with a loss of porosity information due to beam hardening (Fig. 6.1A). The increasing slice numbers represents the sample from top to bottom and Fig. 6.1B shows one of the image slices of the sample. To improve image contrast in Figure 6.1B ImageJ free software was used to minimise the background information in order to optimise the discrimination between quartz, hematite and pores. The quantified %Error for all the image slices is less than 10% which falls within the range of %Error that is not associated with a loss of sample information. The highest %Error for the massive hematite is 6% which represents a region of the sample with less porosity. The sample regions with %Error values less than 2%, represent sample regions with the highest porosity information and this can be observed between slice number 1 to 50 and 220 to 340 (Fig. 6.1A). This could also be observed from the frequency distribution of pore sizes where pores with a diameter ranging from 13 to 40  $\mu\text{m}$  were between 10 to 56% (Fig. 6.2). The total quantified porosity of the sample was 3.2 volume% across all the image

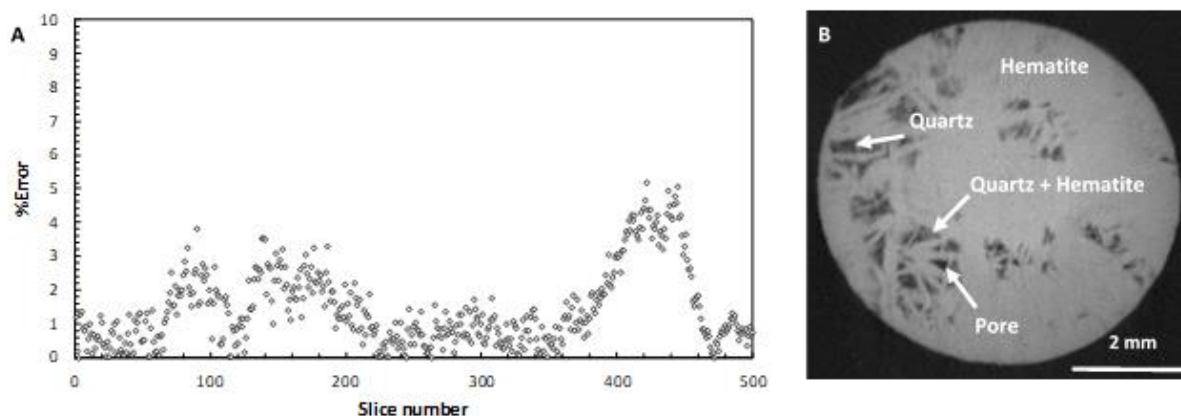


**Fig 6.1.** (a) The distribution of the quantified %Error in each slice of the massive hematite ore sample and (b) Iron formation showing the presence of quartz and pores in the interstitial spaces of massive hematite ore (slice number 157).

## CHAPTER 6: Case Studies

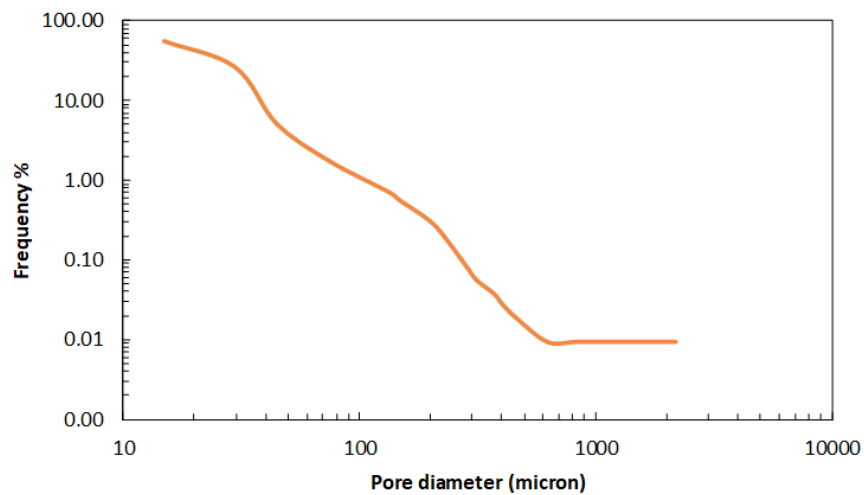


**Fig 6.2.** Histogram of frequency of 3D pore diameter distribution within the interstitial spaces of the massive hematite ore sample.

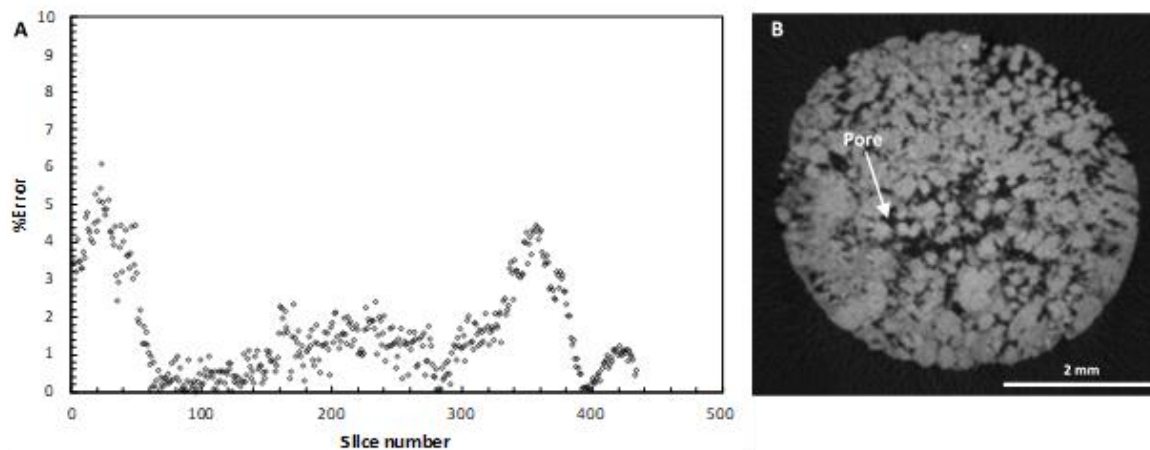


**Fig 6.3.** (a) The distribution of %Error for compact hematite and (b) 2D image slice of compact hematite (slice number 212)

## CHAPTER 6: Case Studies

**Table 6.3**

Comparison of 2D and 3D porosity information of different iron ore samples.

Sample	XCT Porosity	QEMSCAN Porosity
	(%)	(%)
Massive hematite	3.20	0.85
Compact hematite	7.20	5.30
Compact itabirite	1.70	1.10
Goethite	2.14	2.00

slices. The quantified 3D porosity is higher than the QEMSCAN porosity result which is 0.85% (Table 6.3). Similarly, the %Error was quantified for the compact hematite, compact itabirite and goethite ore samples from Brazil to evaluate the reliability of the quantified porosity information. For the compact hematite ore, the %Error was less than 6% for the entire sample (Fig. 6.3A) with the majority of the regions less than 2% highlighting the porous

character of the sample (Fig. 6.3B). The quantified total porosity in the compact hematite ore was 7.2%. The compact itabirite ore showed increasing %Error values from the top to the bottom of the sample (increasing slice numbers; Fig. 6.4A). The majority of the sample image slices, from 1 to 1359, have a %Error less than or equal to 10%, while from slice 1360 to 1400 the values were higher than 10% due to more compact itabirite in those regions (Fig. 6.4B). Taking into account the above %Error information, the quantified 3D porosity for the compact itabirite was 1.7%. The difference in porosity is also demonstrated by the relatively bigger pores in terms of diameter in the compact hematite compared to the compact itabirite pores (Fig. 6.5). The goethite ore sample also had quantified %Error values less than 10% for the entire sample with the majority of the images slices with %Error values less than 2% (Fig. 6.6A). The quantified total porosity of the sample was found to be 2.14% (Fig. 6.6B). All the quantified porosity results for compact hematite, compact itabirite and goethite were compared with the QEMSCAN porosity results as demonstrated in Table 6.3.

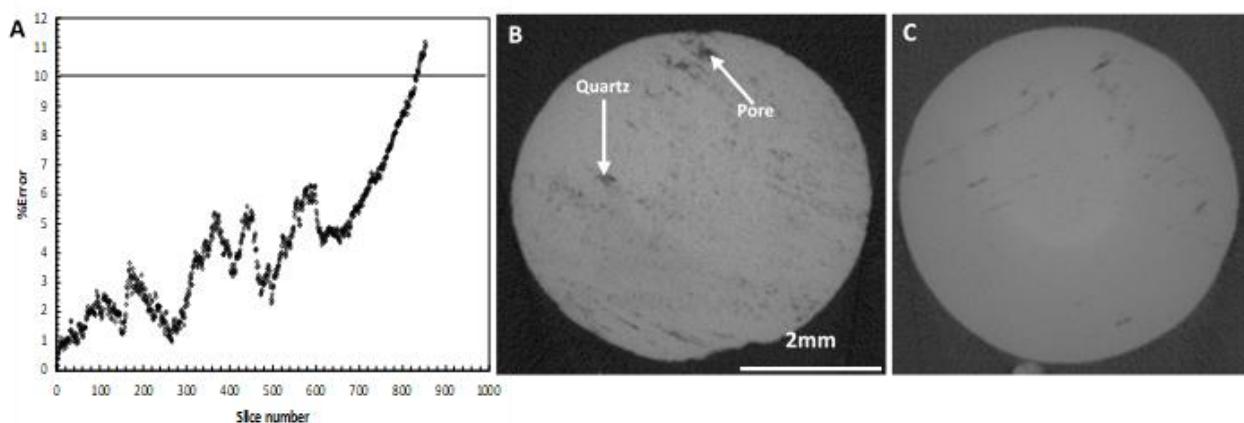
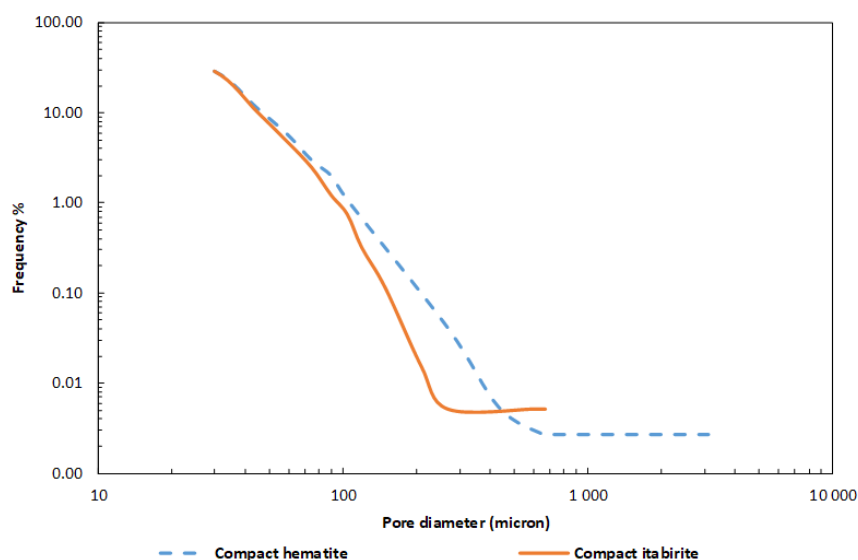


**Fig 6.4.** (a) The distribution of %Error for compact itabirite, (B) 2D image slice (slice number 311) and (C) 2D image slice (slice number 433) of compact itabirite.



## CHAPTER 6: Case Studies

**Fig 6.5.** Histogram of frequency of 3D pore diameter distribution of compact itabirite and hematite with minimum pore size of 15  $\mu\text{m}$ .

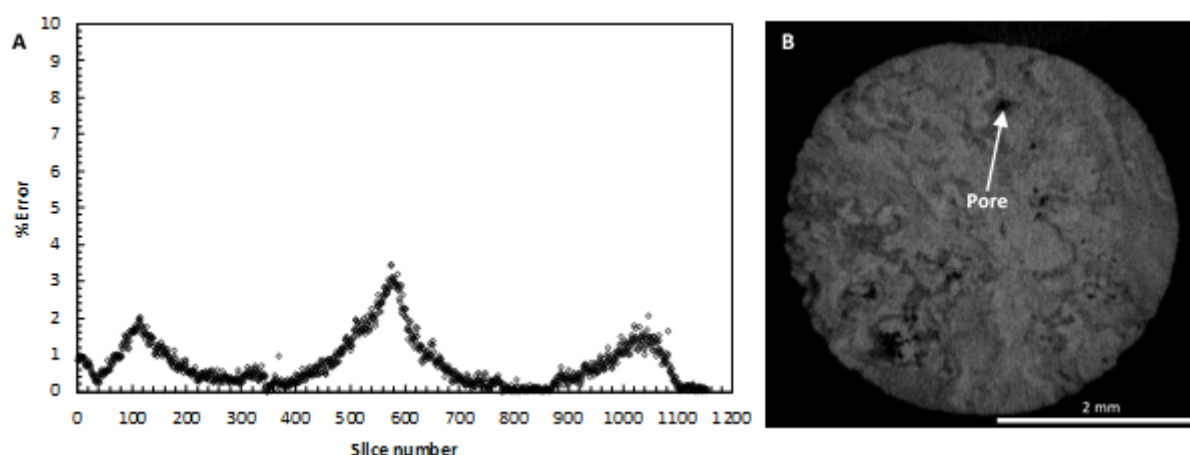


**Fig 6.6.** (a) The distribution of %Error for goethite and (b) 2D image slice of goethite.

### 3.2. Discussion

The low %Error for the massive hematite sample showed that the sample is minimally affected by beam hardening and hence the quantified porosity information for the sample is a true reflection of the sample and is reliable. The big difference between 2D and 3D quantified porosity information is that in 3D the total volume porosity is captured including its distribution whereas in 2D only surface porosity and distribution is quantified. This poses a challenge for 2D quantification when the distribution of pores including pore sizes have a random and non-uniform distribution within an ore sample. The more variable the ore, the larger the sample volume that would need to be analysed in order to improve the comparison between 2D and 3D. The compact hematite had sample regions with %Error similar to massive hematite but compact hematite had higher quantified porosity information. This is due to the massive hematite sample consisting of more quartz within the sample. Quartz has a lower SG which means it is less attenuating which results in higher X-ray penetration. The goethite ore sample also had a majority of the sample regions with %Error less than 2% but its porosity was lower compared to the massive hematite and compact hematite samples. This is due to the lower SG of the goethite ore sample as compared to the higher SG (5.26) of hematite. All the samples had a similar external diameter which means that the lower %Error for the goethite sample is due to more X-ray penetration as compared to hematite samples. In the case of hematite samples the lower %Error represents X-ray penetration in regions where the effective thickness of hematite is less than 6mm due to the presence of quartz and/or pores. The compact itabirite had the lowest quantified porosity information and this was indicative in its increasing %Error distribution. The sample also had %Error greater than 10% which indicates inconsistent sample

information that would result in inconsistent porosity information. The quantified porosity information for compact itabirite excluded the sample region with %Error values more than 10% to minimize errors associated with a loss of sample information due to beam hardening. Despite the differences in %Error distributions of compact hematite, compact itabirite and goethite, the 3D quantified porosity information is in agreement with the 2D QEMSCAN data. This agreement between the 2D and 3D is attributed to the uniform distribution of the porosity information within the samples. This means that the %Error distributions are a true reflection of the density distribution of a sample, different proportions of the mineralogy and effective thickness of the sample matrix (goethitic, hematitic, itabiritic, etc).

## 4. Polymetallic Sulphide ore Case study

### 4.1. Results

The %Error was found to be less than 10% for the entire sample meaning the entire sample can be used for further quantification (Fig. 6.7). The simplified dual energy method was then implemented on the sample to discriminate chalcopyrite from pyrite. The discrimination between chalcopyrite and pyrite grains is not possible without dual energy analysis (Fig. 6.8A and B). This is due to the highly attenuated X-ray beam (45.5keV effective energy) such that its effective energy is equivalent to 70keV where pyrite ( $2.61\text{cm}^{-1}$ ) and chalcopyrite ( $2.73\text{cm}^{-1}$ ) linear attenuation coefficient difference is 4.4%. The discrimination between magnetite and chalcopyrite was also optimized after dual energy subtraction (Fig. 6.8C and D). This is shown by the bright grey values of magnetite which are distinct from chalcopyrite (Fig. 6.8D). The dual energy subtraction results in a reduction in chalcopyrite surface area before and after

## CHAPTER 6: Case Studies

subtraction of 60%. However, the resultant discriminated chalcopyrite grey values (mean 75.96) were comparable with those of the chalcopyrite standard sample (mean 79.68). Thereafter, the volume and equivalent diameter of each chalcopyrite grain was quantified in 3D and converted to mass of chalcopyrite for each grain. Therefore, the quantified total mass of the 3D chalcopyrite grains (22g) was more than the 2D chalcopyrite grains (18g) by 18.9%. The 3D chalcopyrite grain size distribution (GSD) was

then compared with the same sample using QEMSCAN (Fig. 6.9). As expected the 3D chalcopyrite GSD show a coarser distribution with an overall similar trend when compared to the QEMSCAN data. This is attributed to the fact that more regions of the same sample were quantified using the QEMSCAN which optimised the comparison between 2D and 3D GSD (Fig. 6.10). This also indicates that the utilisation of the simulated image does optimise the discrimination between chalcopyrite and pyrite.

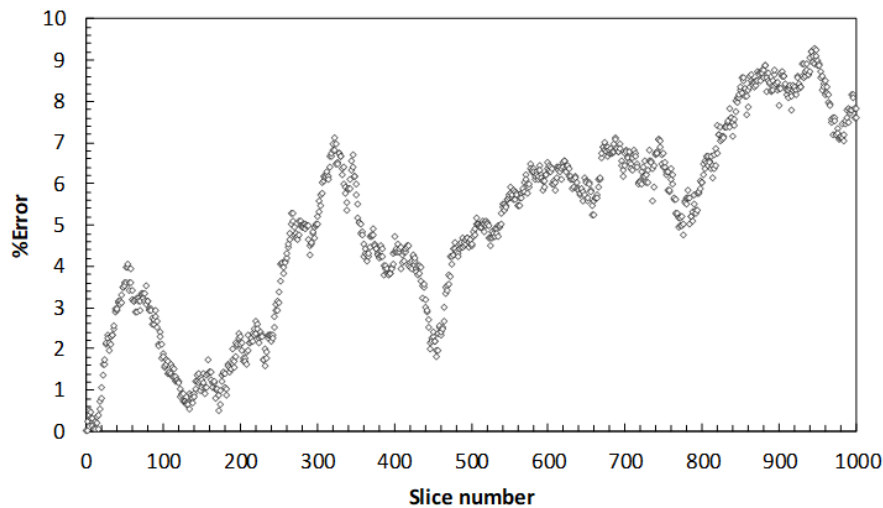
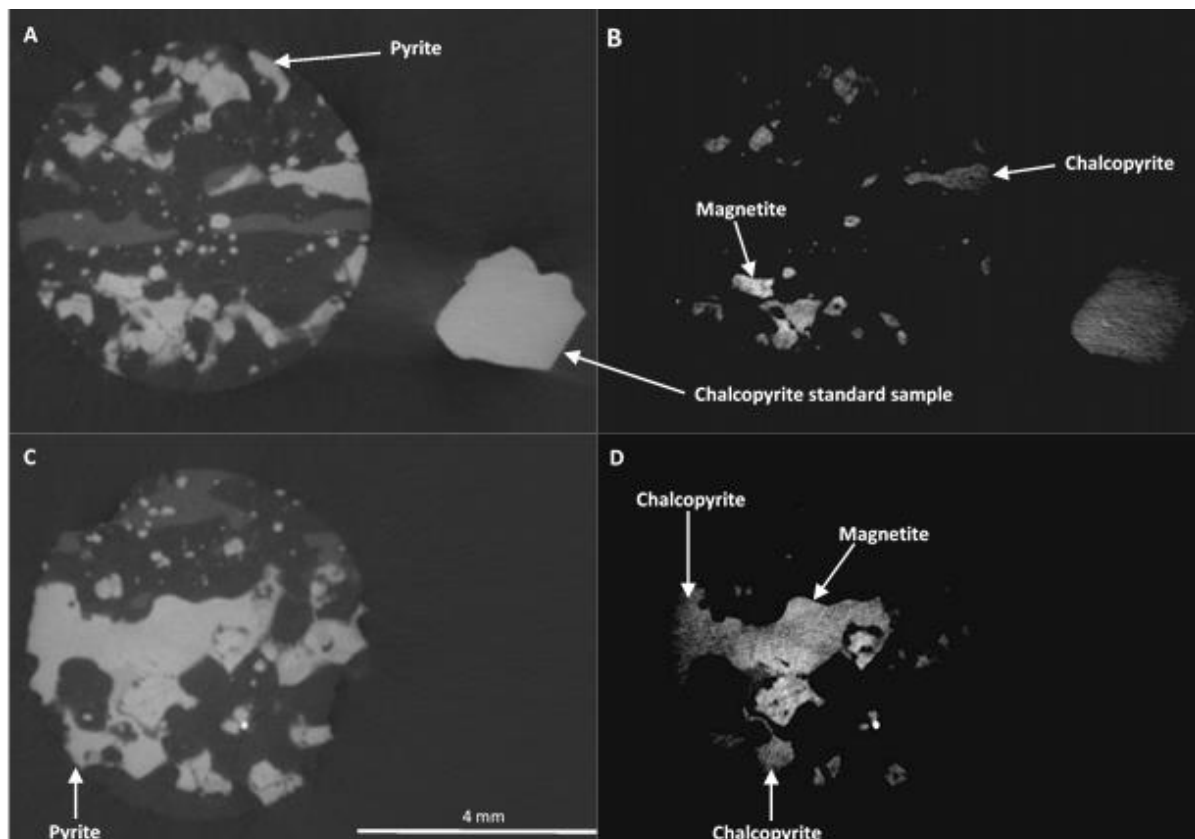


**Fig 6.7.** %Error for each image slice of the polymetallic sulphide ore sample (UOB) at 70kV X-ray energy.





## CHAPTER 6: Case Studies

**Fig 6.8.** Shows different image slices of the polymetallic sulphide ore sample with magnetite dominated before and after dual energy subtraction (a) and (c), and (b) and (d). The discriminated chalcopyrite grains grey values were compared to the chalcopyrite standard sample.

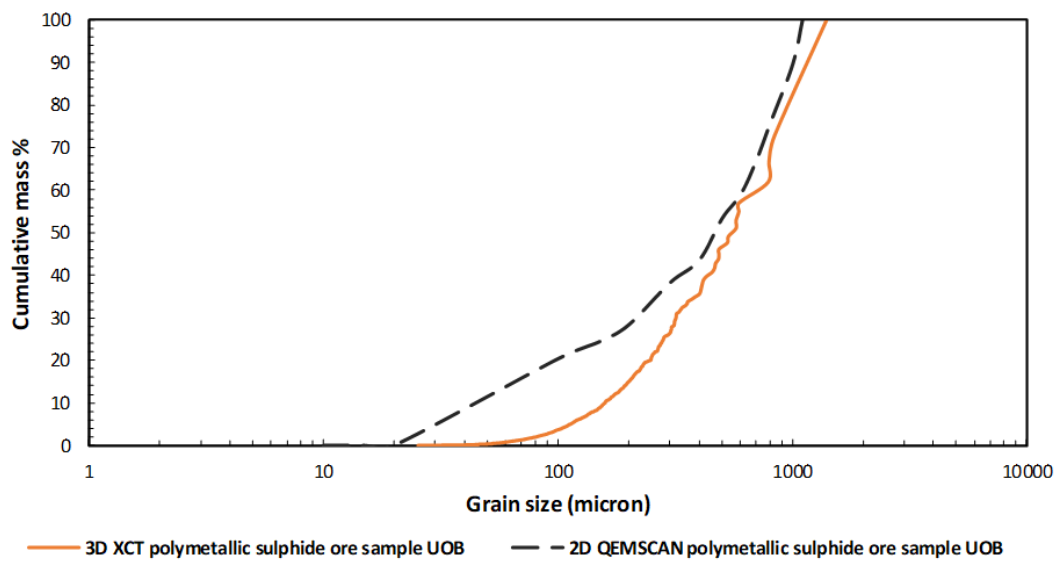


**Fig 6.9.** The comparison of 3D XCT (UOB) and QEMSCAN (UOB) grain size distribution of the polymetallic sulphide ore sample.

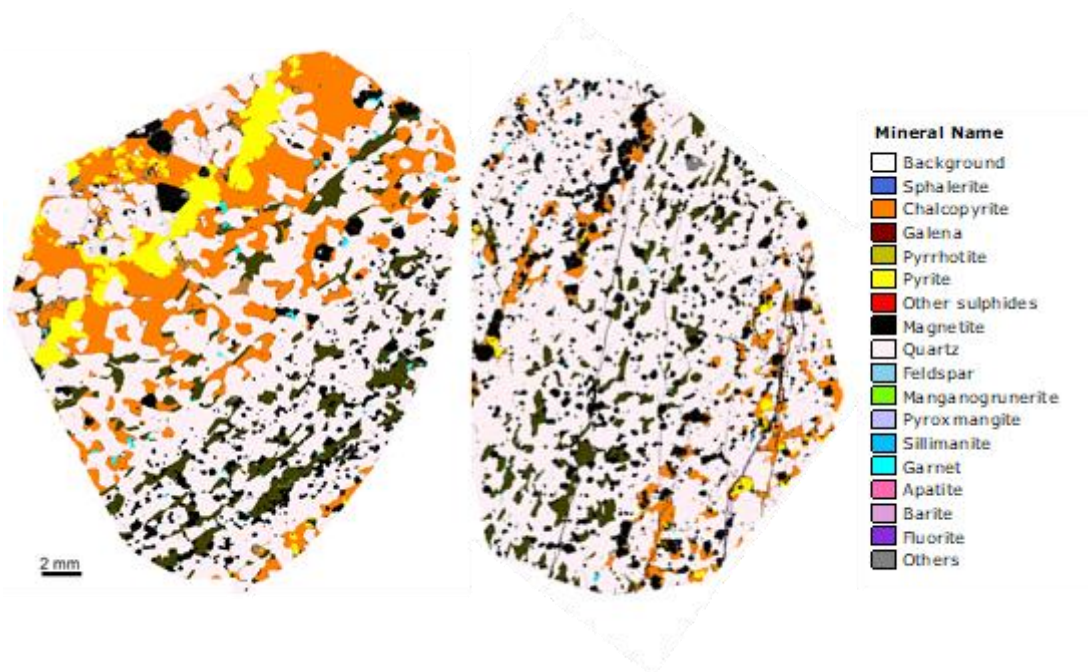


**Fig 6.10.** QEMSCAN images showing different distributions of the chalcopyrite grains in different sections of the same polymetallic sulphide ore sample

#### 4.2. Discussion

The utilization of the %Error together with the simplified dual energy method improved the ability to discriminate chalcopyrite from pyrite and magnetite. The advantage of the dual energy subtraction method using the 130kV simulated image is that it uses a

single grey value to optimize the discrimination of chalcopyrite from pyrite. This means that the majority of chalcopyrite grey values that overlap with pyrite are removed, leaving only the chalcopyrite grey values that are genuinely distinct from pyrite based on attenuation coefficient. In the case of using two scanning conditions (70kV and 130kV) the discrimination is

## CHAPTER 6: Case Studies

difficult because the two sample volumes are affected differently by beam hardening. This means that the pixel grey values do not meet the grey value difference required to discriminate chalcopyrite from pyrite and this results in noisy images. Even though the utilization of a simulated image improved the discrimination between pyrite and chalcopyrite, it resulted in artificially smaller surface area/volume of the chalcopyrite grains, impacting on the true diameter of the grains but this did not affect the 3D chalcopyrite GSD. Thus, the XCT shows overall coarser chalcopyrite grain sizes compared to the QEMSCAN data as expected. The quantified XCT chalcopyrite grains are larger because they are 3D in nature and more grains are quantified which increases the probability of XCT to quantify even larger grains than QEMSCAN data. This is also evident in the quantified total mass of the 3D chalcopyrite grains which is more than the QEMSCAN. The 3D chalcopyrite GSD show an overall similar trend when compared with the QEMSCAN data. The similar trends show that the quantified 3D chalcopyrite GSD is a true reflection of the sample characteristics and the application of a simplified dual energy method is reliable. The simplified dual energy method is not limited to the discrimination of chalcopyrite from pyrite in dense ore samples. It can also be applied to different ore types ranging from low to high density ores that consist of different minerals with similar attenuation coefficients that require the utilization of the dual energy method to discriminate between

## 5. Conclusions

Beam hardening is a challenge in XCT due to the lack of X-ray penetration when dealing with high density ore samples that limit its application. With a better understanding of this challenge, there is the potential for development of refined scanning protocols and analysis methods that can overcome this challenge. The utilization of an aluminium standard sample shows that the accuracy required to quantify porosity information within the iron ore samples is attainable when evaluated using the %Error analysis approach. Comparison of the quantified 3D porosity information between XCT and QEMSCAN indicates that XCT is an effective and reliable technique for quantification of this parameter in high density ore samples and can therefore be used within the minerals processing environment for predicting and optimising downstream processing. The utilization of an aluminium standard sample and the simplified dual energy method were also effective in enabling discrimination of chalcopyrite from pyrite. However, more investigation about the %Error analysis is needed in order to understand the impact of beam hardening on the actual grey values themselves. This will optimize the application of the simplified dual energy method and result in the actual quantification of the chalcopyrite grain sizes with respect to volume and

diameter. However, the application of the simplified dual energy method resulted in coarser grain sizes of the chalcopyrite when compared to QEMSCAN data.

## 6. Acknowledgements

The authors would like to thank Necsa and the management team for funding and access to the Microfocus system in the MIXRAD Lab, which is a DST-NRF (Department of Science and Technology – National Research Funding) funded facility through the NEP-RISP (National Equipment Programme – Research Infrastructure Support Programmes) program. The authors would also like to acknowledge Gaynor Yorath and the QEMSCAN team for assistance with QEMSCAN analysis. The project is generously supported through the South African Minerals to Metals Research Initiative (SAMMRI). The authors would also like to thank Henry Gordon and Thiago de Souza for providing with the samples. This work is based on the research supported in part by the National Research Foundation of South Africa (Grant Numbers 86054, 99005). Any opinions, findings and conclusions or recommendations expressed in any publication generated by the NRF supported research is that of the author(s), and that the NRF accepts no liability whatsoever in this regard.

## 7. References

- Bam, L.C., Miller, A.J., Becker, M., Basson, I.J., 2019. X-ray Computed Tomography: Practical Evaluation of Beam Hardening in Iron Ore Samples. *Miner. Eng.* 131, 206–215. <https://doi.org/10.1016/j.mineng.2018.11.010>
- Bam, L.C., Miller, J., Becker, M., 2018. Application of a Simplified Dual Energy X-Ray Computed Tomography Method for Analysis of High Density Ore Samples.
- Bam, L.C., Miller, J., Becker, M., 2018. A simple Tool to Calculate X-ray Linear Attenuation Coefficients to Assess Mineralogical Differentiation for X-ray Computed Tomography Scanning.
- Bam, L.C., Miller, J.A., Becker, M., Beer, F.C. De, Basson, I., 2016. X-ray Computed Tomography – Determination of Rapid Scanning Parameters for Geometallurgical Analysis of Iron Ore, in: *Proceedings of the Third AusIMM International Geometallurgy Conference*. Perth, pp. 209–219.
- Bhuiyan, I.U., Mouzon, J., Forsberg, F., Forsmo, S.P.E., Sjödaahl, M., Hedlund, J., 2013. Consideration of X-ray microtomography to quantitatively determine the size distribution of bubble cavities in iron ore pellets. *Powder Technol.* 233, 312–318. <https://doi.org/10.1016/J.POWTEC.2012.09.012>
- Bucher, A.M., Wichmann, J.L., Schoepf, U.J., Wolla, C.D., Canstein, C., McQuiston, A.D., Krazinski, A.W., De Cecco, C.N., Meinel, F.G., Vogl, T.J., Geyer, L.L., 2016. Quantitative evaluation of beam-hardening artefact correction in dual-energy CT myocardial perfusion imaging. *Eur. Radiol.* 26, 3215–3222. <https://doi.org/10.1007/s00330-015-4137-x>

## CHAPTER 6: Case Studies

- Cropp, A.F., Goodall, W.R., Bradshaw, D.J., 2013. The Influence of Textural Variation and Gangue Mineralogy on Recovery of Copper by Flotation from Porphyry Ore – A Review, in: Proceedings of the Second AusIMM International Geometallurgy Conference. pp. 279–291.
- Evans, C.L., Wightman, E.M., Yuan, X., 2015. Quantifying mineral grain size distributions for process modelling using X-ray micro-tomography. *Miner. Eng.* 82, 78–83. <https://doi.org/10.1016/J.MINENG.2015.03.026>
- Fagan-Endres, M.A., Cilliers, J.J., Sederman, A.J., Harrison, S.T.L., 2017. Spatial variations in leaching of a low-grade, low-porosity chalcopyrite ore identified using X-ray  $\mu$ CT. *Miner. Eng.* 105, 63–68. <https://doi.org/10.1016/J.MINENG.2017.01.010>
- Fonteneau, L.C.P.J., Gobel, B., Ramanaidou, E.R., 2013. Application of High-Resolution X-ray Computed Tomography to Iron Ore Characterisation, in: Iron Ore Conference.
- Fragomeni, D., Boyd, L.J., Charland, A., Kormos, L.J., Lotter, N.O., Potts, G., 2005. The use of End-Members for grind-recovery modelling, tonnage prediction and flowsheet development at Raglan, in: Canadian Mineral Processor. pp. 75–98.
- Ghorbani, Y., Becker, M., Petersen, J., Morar, S.H., Mainza, A., Franzidis, J.-P., 2011. Use of X-ray computed tomography to investigate crack distribution and mineral dissemination in sphalerite ore particles. *Miner. Eng.* 24, 1249–1257. <https://doi.org/10.1016/J.MINENG.2011.04.008>
- Gordon, H.J.J., Miller, J.A., Becker, M., 2018. Using Mineralogy for Early Stage Geometallurgical Domain Definition : a Case Study of the Swartberg Polymetallic Sulphide Deposit. *Proc. Geometallurgy 2018* 121–132.
- Hoffman, J.W., de Beer, F.C., 2012. Characteristics of the Micro-Focus X-ray Tomography Facility ( MIXRAD ) at Necsa in South Africa, in: 18th World Conference on Nondestructive Testing. pp. 1–12.
- Kheruka, S., Naithani, U., Maurya, A., Painuly, N., Aggarwal, L., Gambhir, S., 2011. A study to improve the image quality in low-dose computed tomography (SPECT) using filtration. *Indian J. Nucl. Med.* 26, 14–21. <https://doi.org/10.4103/0972-3919.84595>
- Lin, C.L., Miller, J.D., Nguyen, T., Nguyen, A., 2017. Characterization of Breakage and Washability of ROM Coal using X-ray Computed Tomography. *Int. J. Coal Prep. Util.* 1–14. <https://doi.org/10.1080/19392699.2017.1305364>
- Lin, Q., Andrew, M., Thompson, W., Blunt, M.J., Bijeljic, B., 2018. Optimization of image quality and acquisition time for lab-based X-ray microtomography using an iterative reconstruction algorithm. *Adv. Water Resour.* 115, 112–124. <https://doi.org/10.1016/j.advwatres.2018.03.007>
- Miller, J., Lin, C., 2003. 3D ANALYSIS OF PARTICULATES IN MINERAL PROCESSING SYSTEMS BY CONE BEAM X-RAY MICROTOMOGRAPHY, in: Lorenzen, L., Bradshaw, D.J. (Eds.), XXII International Mineral Processing Congress. Cape Town. South Africa, p. 15.
- Miller, J.D., Lin, C.L., Cortes, A.B., 1990. A Review of X-Ray Computed Tomography and Its Applications in Mineral Processing. *Miner. Process. Extr. Metall. Rev.* 7, 1–18. <https://doi.org/10.1080/08827509008952663>
- Muwanguzi, A.J.B., Karasev, A. V., Byaruhanga, J.K., Jonsson, P.G., 2012. Characterization of Chemical Composition and Microstructure of Natural Iron Ore from Muko Deposits. *ISRN Mater. Sci.* 2012, 1–9. <https://doi.org/10.5402/2012/174803>
- Parbhakar-Fox, A.K., Edraki, M., Walters, S., Bradshaw, D., 2011. Development of a textural index for the prediction of acid rock drainage. *Miner. Eng.* 24, 1277–1287. <https://doi.org/10.1016/J.MINENG.2011.04.019>
- Reyes, F., Lin, Q., Udoudo, O., Dodds, C., Lee, P.D., Neethling, S.J., 2017. Calibrated X-ray micro-tomography for mineral ore quantification. *Miner. Eng.* 110, 122–130. <https://doi.org/10.1016/J.MINENG.2017.04.015>
- Shatokha, V., Korobeynikov, I., Maire, E., Gremillard, L., Adrien, J., 2010. Iron ore sinter porosity characterisation with application of 3D X-ray tomography. *Ironmak. Steelmak.* 37, 313–319. <https://doi.org/10.1179/030192310x12683045805865>
- Stenner, P., Berkus, T., Kachelriess, M., 2007. Empirical dual energy calibration (EDEC) for cone-beam computed tomography. *Med. Phys.* 34, 3630–3641. <https://doi.org/10.1118/1.2769104>
- Wang, Y., McClung, C., Lin, C.L., Miller, J.D., 2018. Stereological correction of perimeter based estimates of exposed grain surface area. *Miner. Eng.* 126, 64–73. <https://doi.org/10.1016/J.MINENG.2018.06.026>

## Conclusions and Recommendations

In this chapter the outcomes of this thesis are discussed in terms of the original project objectives with consideration of the key questions that were posed in Chapter 1. Thereafter, consideration of the general findings are presented and an assessment made on the future of XCT for routine mineralogical and textural characterisation of high-density ores.

In Chapter 2 the key objective was to build an attenuation coefficient data bank in order to predict mineralogical discrimination in high-density ores using XCT prior to scanning and quantification. The spreadsheet calculated linear attenuation coefficients of different minerals to determine the linear attenuation coefficient difference. The spreadsheet was based on NIST data but is more flexible than the NIST online calculator because it can be used offline and linear attenuation coefficients can be calculated for X-ray energies spectrums between (40 to 225keV). This is an important requirement for exploiting subtle differences in linear attenuation coefficients of mineral pairs at different X-ray energies. Based on the linear attenuation coefficient information correlated with the grey values of the scanned minerals, the minimum attenuation coefficient difference required to differentiate two minerals using XCT is greater than 6% at 45.5keV effective X-ray energy. Minerals with a percentage difference in linear attenuation coefficient less than this generally have similar densities. In contrast to the density, the chemical composition of the minerals had a greater contribution to the linear attenuation coefficient of a mineral. It was pointed out that this is sometimes contrary to impressions using the example of barite which has a low density but a high linear attenuation coefficient because of its composition. In light of this finding, minerals were found to be difficult to discriminate when their attenuation coefficient difference was below the above indicated minimum. The development of the spreadsheet to calculate the linear attenuation coefficients together with the scanned minerals were instrumental in analysing the ability of XCT to differentiate different minerals in the samples that were used in subsequent chapters. In particular, the calculation spreadsheet was instrumental in understanding the potential for discrimination of chalcopyrite from pyrite using dual energy. The method for doing this was explored in Chapter 5.

In Chapter 3 the key objective was to determine the optimal scanning parameters to quantify mineralogical and textural information in high density ores. The focus was on a method to evaluate the impact of different scanning parameters for high density ore samples. The parameters considered for optimisation included: number of projections, exposure time, signal-to-noise ratio and sample contrast. The number of projections had the greatest impact on the quality of the scan images after a beam hardening correction was applied. The number of projections defined the resolution and this is important for the quantification of mineralogical and textural information. The exposure time had little impact on the textural information (but only when the number of projections were optimal and corrected for beam hardening). The corrected images for beam hardening were associated with a highest signal-to-noise ratio, and hence less



## CHAPTER 7: Conclusions and Recommendations

noise within the images. The scanning protocol demonstrated the ability of XCT to scan drill cores rapidly to obtain mineralogical information. This is an important finding because obtaining information rapidly is a core requirement for the potential implementation of XCT on a mine site. Previously, it was assumed that getting high quality information from XCT scans required long scan durations. This part of the study successfully demonstrated that long scan times were not a pre-requisite to generate image volumes from which textural information required for downstream ore characterisation, could be generated.

In Chapter 4 the third objective for this thesis was to develop a method that quantified the amount of sample information lost due to beam hardening in high density ores. This is a significant contribution given that the effect of its impact on sample information was effectively unknown. Previously, it had always been assumed that the impact of beam hardening could be minimised through the use of various filter materials, calibration methods and mathematical functions to correct for the grey value variations of single materials. The developed method made use of an aluminium standard sample from which the sample size associated with a loss of sample information could be identified using the %Error. %Error values above 10% were associated with a loss of sample information as determined by comparison of the quantified pore surface area with the known pore surface area of the aluminium standard sample. The method was applied to a hematite stepped-wedge sample where a specularite crystal vein “disappeared” with increasing sample thickness due to beam hardening. The recognition of this disappearance represented an important guide towards the recognition of loss of sample information. The method also showed that low density sample information (e.g. porosity) was the most affected by beam hardening. . This method was used in Chapter 6 for quantification of both porosity in iron ores and chalcopyrite grain size distribution in polymetallic sulphide ores.

In Chapter 5 the fourth objective for this thesis was to develop a new approach for dual energy scanning applied to high density ore samples where beam hardening affects the discrimination between minerals. This key objective was addressed by developing a simplified dual energy approach to optimize the discrimination of the chalcopyrite – pyrite mineral pair. The method used information derived from single energy scanning at a lower X-ray energy where a small variation of the linear attenuation coefficient exists. The other X-ray energy scan information was simulated based on the same linear attenuation coefficient of pyrite and chalcopyrite at higher X-ray energy which meant the two minerals have the same grey value. In the case of beam hardening the normal dual energy subtraction method could not discriminate the two minerals due to the change in grey value distribution and grey value ratio between chalcopyrite and pyrite. While both methods are limited in their ability to discriminate minerals that share the same linear attenuation coefficient across all the X-ray energies the simplified method was successful in discriminating two minerals in cases where the X-ray source or beam was not optimized or resulted in edge artefacts. The proposed method was applied to the polymetallic case study presented in Chapter 6.

In Chapter 6 the fifth objective for this thesis was to demonstrate the practical application of the scanning methods and protocols developed in Chapter 4 and 5 (but also incorporating information from chapters 2 and 3) using high density ores and their relevance to the minerals processing industry using two case studies. The case studies examined the analysis of porosity information for a set of iron ore samples and the discrimination and quantification of chalcopyrite grain size distribution in a polymetallic sulphide ore. For both ore samples, the aluminium standard sample was applied to quantify the loss of sample information due to beam hardening. Comparison of the 3D calculated porosity for various iron ore samples was in agreement with that derived from 2D QEMSCAN analysis. One notable exception was the massive hematite sample where the variability between measurement techniques was attributed to the non-uniform

## CHAPTER 7: Conclusions and Recommendations

distribution of the porosity information in this sample. This illustrates one of the added benefits of the 3D XCT technique that allowed the analysis of a greater sample volume compared to the limited area analysed using 2D sections. The quantified chalcopyrite grain size distribution showed a similar distribution with coarse grains as compared to the QEMSCAN data as expected. The quantified porosity and chalcopyrite GSD emphasised the importance of an optimal sample size in order to obtain accurate results when using XCT. Due to the established relationship mentioned above, XCT can be used as one of the techniques to provide textural attributes relevant for predicting and optimising downstream minerals processing.

The ability of XCT to quantify mineralogical and textural information in high density ores using specialised scanning protocols and analysis methods is an important finding. This means that XCT can be used to obtain 3D mineralogical and textural information that is important for the design of mineral processing circuits, their optimization, benchmarking and trouble shooting. There are routine analytical techniques that are used to obtain this information due to easy access (QXRD, Optical microscope, chemical assays, etc). XCT is regarded as a specialised technique because it lacks routine scanning and analysis protocols that can be used to obtain textural information. However, with the scanning methods developed here that optimise the quantification of textural attributes, XCT has the potential to become one of the routine techniques for process mineralogy in the near future. It is important to note that the scanning protocols and analysis were developed using small sample sizes (~6 mm drill cores). This size is smaller than commonly used drill cores on mine sites and this might affect statistical representation of the mineralogical and textural information of the ore. However, recent physical developments of the XCT systems (outside the scope of this study) allow routine scanning of samples to facilitate automated scanning of a larger number of samples and this will address the issue of representability. To facilitate this application only the optimal sample sizes determined in this study will be used.

To optimize the required mineralogical and textural information of high-density ores, the sample size needs to be further optimized. This should be based on the sensitivity and nature of the required mineralogical and textural information. From this study it was found that beam hardening changes the grey value ratio between minerals in cases where there is no loss of sample information. This means that the variation of %Error values between (0 and 10%) needs to be better understood. This is well illustrated by the quantified porosity information in iron ore samples. For %Error less than 10% the quantified porosity information is valid due to a large attenuation coefficient difference between hematite and pores. However, for the discrimination between minerals with similar attenuation coefficients the %Error needs to provide a better indication on what is happening to the actual grey values as it varies from 0 to 10%. The exact value(s) that indicates the preserved theoretical ratio of the attenuation coefficient difference would be determined and understood. This would optimise the developed spreadsheet to calculate the linear attenuation coefficient that is correlated with the required sample size. Lastly, the turnaround time for scanning high density ore samples would be optimized because all the possible contributions that result to an image artefact will be minimized.